Pacific Northwest
NATIONAL LABORATORY

PNNL-39318

PIE-Enabled Study of Aqueous Corrosion & Zr Hydriding in Cr-Coated Cladding

M3GV-23PN0101132

May 2026

Susan E. Asmussen,[1] Mukesh Bachhav,[2] Konstantina Lambrinou,[3] Edgar Buck,[1] Peng Xu,[2] Bjorn Westman,[1] Aj Goulet,[1] Bradley Jeffries,[1] Joshua Silverstein[1]

[1] Pacific Northwest National Laboratory
[2] Idaho National Laboratory
[3] University of Huddersfield

U.S. DEPARTMENT of ENERGY

Prepared for the U.S. Department of Energy
under Contract DE-AC05-76RL01830

DISCLAIMER

PACIFIC NORTHWEST NATIONAL LABORATORY
operated by
BATTELLE
for the
UNITED STATES DEPARTMENT OF ENERGY
under Contract DE-AC05-76RL01830

Printed in the United States of America

Available to DOE and DOE contractors from
the Office of Scientific and Technical Information,
P.O. Box 62, Oak Ridge, TN 37831-0062
www.osti.gov
ph: (865) 576-8401
fax: (865) 576-5728
email: reports@osti.gov

Available to the public from the National Technical Information Service
5301 Shawnee Rd., Alexandria, VA 22312
ph: (800) 553-NTIS (6847)
or (703) 605-6000
email: info@ntis.gov
Online ordering: http://www.ntis.gov

PNNL-39318

PIE-Enabled Study of Aqueous Corrosion & Zr Hydriding in Cr-Coated Cladding

M3GV-23PN0101132

May 2026

Susan E. Asmussen, Mukesh Bachhav, Konstantina Lambrinou, Edgar Buck, Peng Xu, Bjorn Westman, Aj Goulet, Bradley Jeffries, Joshua Silverstein

Pacific Northwest National Laboratory
Richland, Washington 99354

Idaho National Laboratory
Idaho Falls, Idaho 83415

University of Huddersfield
Queensgate, Huddersfield HD1 3DH

Abstract

Chromium-coated zirconium alloy cladding is under development as an accident-tolerant fuel (ATF) technology to extend performance to higher burnups via improved oxidation resistance and reduced hydrogen pickup. However, hydrothermal corrosion behavior and hydrogen transport mechanisms governing in-service hydriding of these coatings remain poorly understood. In a collaborative study between Pacific Northwest National Laboratory (PNNL), Idaho National Laboratory (INL), and the University of Huddersfield, cold spray (CS) and physical vapor deposition (PVD) Cr-coated Optimized ZIRLO™ cladding samples were characterized after exposure to PWR-simulated water chemistry under both in-core (neutron irradiation) and out-of-core (aqueous-only) conditions at the Massachusetts Institute of Technology (MIT) Research Reactor. Multi-scale characterization was performed independently at PNNL and INL to evaluate coating integrity, microstructural evolution, Cr/Zr interface chemistry, and hydride formation.

Both laboratories observed a consistent divergence in hydriding behavior: out-of-core CS Cr-coated cladding exhibited elevated hydride concentrations exceeding those of uncoated cladding, whereas in-core CS samples showed substantially suppressed hydriding. In-core specimens also displayed irradiation-specific features, including nanoscale voids within the Cr-coating and radiation-induced segregation clusters in the Zr substrate. CS coatings retained an interdiffusion-free Cr/Zr bond with no intermetallic layer, whereas PVD coatings exhibited inferior quality with visible cracks and pores. An automated image-based hydride quantification method systematically overestimated bulk hydrogen content relative to inert gas fusion measurements, underscoring the need for standardized sample preparation and reference standards to support further development.

Interpretation of hydride nucleation and growth is complicated by the open inner diameter of the specimens, which provides additional hydrogen pathways, although the studies showed that even samples that exhibited hydride formation had less hydrogen near the inner diameter than elsewhere across the substrate wall thickness. The results motivate further foundational studies to support predictive models of hydrothermal corrosion and hydrogen transport in unirradiated and irradiated Cr-coated cladding.

Summary

Chromium-coated zirconium alloy cladding is being explored as an accident-tolerant fuel (ATF) concept by Westinghouse Electric Company in collaboration with the U.S. Department of Energy with the goal to extend cladding performance to higher burnups through improved oxidation resistance and reduced hydrogen pickup. While high-temperature testing has demonstrated benefits of Cr-coated Zr cladding, the hydrothermal corrosion effects and hydrogen transport mechanisms driving in-service hydriding and embrittlement remain uncertain. In this collaborative study between Pacific Northwest National Laboratory (PNNL), Idaho National Laboratory (INL), and the University of Huddersfield, cold spray (CS) and physical vapor deposition (PVD) Cr-coated Optimized ZIRLO™ cladding samples were characterized following exposure to pressurized water reactor (PWR)-simulated water chemistry in both in-core (neutron irradiation) and out-of-core (aqueous-only) conditions at the Massachusetts Institute of Technology Research Reactor. Multi-scale characterization combining optical microscopy (OM), scanning electron microscopy coupled with energy-dispersive spectroscopy (SEM/EDS), transmission electron microscopy (TEM), atom probe tomography (APT), and inert gas fusion hydrogen analysis was performed independently at PNNL and INL to assess coating integrity, microstructural evolution, Cr/Zr interface chemistry, and hydride formation behavior.

Results from both laboratories revealed a consistent and striking divergence in hydride formation between exposure conditions.

- CS Cr-coated cladding exposed to out-of-core conditions developed significant hydride concentrations, indicating enhanced hydrogen pickup relative to uncoated cladding under the same aqueous conditions. In contrast, in-core CS Cr-coated samples exhibited substantially suppressed hydride formation. In-core samples additionally displayed damage features unique to irradiation, including nano-scale voids within the Cr-coating and nanoscale radiation-induced segregation clusters in the Zr substrate. The CS Cr-coated materials maintained an interdiffusion-free Cr/Zr bond with no intermetallic layer formation.
- The PVD Cr-coatings exhibited inferior structural quality with readily observable cracks and pores.
- An automated image-based hydride quantification approach was explored, but systematically overestimated bulk hydrogen content relative to inert gas fusion measurements, highlighting the critical importance of sample preparation and the need for reference standards to validate such techniques.

Investigation of hydride nucleation and growth mechanisms in the Zr substrate was complicated by the open inner diameter geometry of the cladding specimens tested, which introduces additional pathways for hydrogen ingress into the matrix. However, even samples that exhibited hydride formation had less hydrogen near the inner diameter than elsewhere across the substrate wall thickness. Findings presented here suggest that further studies should be pursued to generate foundational data to support the development of predictive models for hydrothermal corrosion and hydrogen transport in unirradiated and irradiated Cr-coated cladding.

Acknowledgments

The authors acknowledge and thank the many people from various laboratories and groups who contributed to this report, both those names here and any others who were a part of this effort.

We thank the GAIN NE Voucher program for the award and the opportunity to carry out this work. We particularly thank our industrial partner Westinghouse Electric Company, specifically Ed Lahoda and Luke Czerniak.

We thank Brady Hanson and Bob Oelrich for their leadership, guidance, support, and technical knowledge.

Many thanks to the teamsters, crafts, radiological engineers, and support staff who aided in receipt of the materials and facilitated the research performed.

Technical Contributors to, and reviewers of this report, include all those listed below:

PNNL
- Rick Shimskey
- Christian Perez
- Alivia Mourot
- Dallin Barton
- R. Matthew Asmussen
- Brady Hanson

Idaho National Laboratory
- Anshul Kamboj
- Sohail Shah
- Kaustubh Bawane
- Jana Howard
- Alex Pomo
- Alexandria Alcantara
- Scott Anderson

Acronyms and Abbreviations

ADOPT™	Cr_2O_3 and Al_2O_3-doped UO_2
ATF	accident tolerant fuel
BCC	body-centered cubic
BR2	Belgium Reactor 2
BSE	backscattered electron
CMESIC	Critical Materials Energy System and Innovation Center
CRADA	Cooperative Research and Development Agreement
CS	cold spray
d_i	inner diameter
d_o	outer diameter
DOE	Department of Energy
dpa	displacements per atom
EBSD	electron backscatter diffraction
EELS	electron energy loss spectroscopy
EFPD	equivalent full power days
EFTEM	energy filtered transmission electron microscopy
FCT	face-centered tetragonal
FEG	field emission gun
FIB	focused ion beam
GAIN	Gateway for Accelerated Innovation in Nuclear
HCP	hexagonal close-packed
IMCL	Irradiated Materials Characterization Laboratory
INL	Idaho National Laboratory
IR	infrared
KIT	Karlsruhe Institute of Technology
LWR	light water reactor
MIT	Massachusetts Institute of Technology
MITR	Massachusetts Institute of Technology Reactor
MW	megawatt
NDIR	non-dispersive infrared
NIST	National Institute of Standards and Technology
NPP	nuclear power plant
OM	optical microscope
PIE	post irradiation examination
PNNL	Pacific Northwest National Laboratory
PVD	physical vapor deposition

PWR	pressurized water reactor
SAED	selected area electron diffraction
SEM/EDS	scanning electron microscopy – energy dispersive x-ray spectroscopy
SiC	silicon carbide
STEM	scanning transmission electron microscopy
TEM	transmission electron microscopy
TIG	tungsten inert gas
UH	University of Huddersfield
WBDF	weak-beam dark-field
wppm	weight parts per million

Contents

Figures

Tables

1.0 Introduction

The Westinghouse Electric Company LLC (Westinghouse) is exploring chromium coated zirconium alloy cladding (Cr-coated Zr cladding) in the accident tolerant fuel (ATF) program that is jointly supported by the U.S. Department of Energy (DOE). The corrosion of zircaloy cladding and resulting hydrogen generation is of critical importance for extending zircaloy cladding performance to higher burnups. Utilizing coatings, specifically Cr-coatings, has shown promise for oxidation resistance, and in turn reduced hydrogen pickup and hydride formation. The Westinghouse Cr-coated Zr cladding has been tested under various conditions utilizing Westinghouse Churchill autoclaves and the Massachusetts Institute of Technology (MIT) Reactor, and high temperature testing facilities at Karlsruhe Institute of Technology (KIT). In the high temperature testing, results indicate that Cr-coated Zr cladding can experience temperatures of up to 1500°C for short periods without total oxidation occurring (E.J. Lahoda 2022). Testing showed that the Cr-coated Zr cladding delayed the bursting of the tube, reduced burst area, and reduced hydriding and embrittlement of the Zr (E.J. Lahoda 2022).

Westinghouse combined the Cr-coated cladding with ADOPT™ (Cr_2O_3 and Al_2O_3-doped UO_2) within their EnCore® Fuel program to achieve higher fuel enrichment (>5% ^{235}U) and burnup, which would allow for 24-month cycles in pressurized water reactors (PWRs) and nuclear power plant (NPP) uprates by the mid-2020's. The selection of metallic chromium was due to its ability to generate a protective chromium oxide scale on the surface of the cladding both in operating conditions and at high temperature oxidations (A. Fazi et al. 2023; K.A. Terrani 2018).

In collaboration, Pacific Northwest National Laboratory (PNNL), Idaho National Laboratory (INL), and the University of Huddersfield (UH) had the opportunity to characterize the Cr-coated Zr cladding material further to understand and gain unique insights into the hydrothermal corrosion effects and hydrogen transport mechanisms driving the observed hydriding and embrittlement. This study planned to focus on Cr-coating deposition methods (namely cold spray [CS] versus physical vapor deposition [PVD]) and a welded sample. Initial plans contained samples from the Massachusetts Institute of Technology Reactor (MITR or MIT Reactor) and the Belgium Reactor 2 (BR2). Unfortunately, it was discovered that the shipment of samples from BR2 was infeasible, reducing the samples available for study to effectively half those initially expected.

The in-core hydrothermal degradation and Zr hydriding behavior was compared between uncoated and Cr-coated Zr cladding samples. As well, similar uncoated and Cr-coated Zr cladding were tested in out-of-core corrosion loop conditions to understand material degradation effects in the absence of neutron irradiation and significantly lower gamma irradiation.

Characterization techniques and post irradiation examination (PIE) activities were performed independently at PNNL and INL to assess hydrothermal degradation of the Cr-coated cladding, such as coating thickness and microstructural features such as the grain size and grain boundary orientation. Data collected from these studies are expected to support efforts regarding the development of reliable, predictive models for hydrothermal corrosion and hydrogen transport in unirradiated and irradiated Cr-coated cladding. The development of a predictive model was beyond the scope of this current Cooperative Research and Development Agreement (CRADA); rather the focus is on the data collection that can parameterize a future model.

This report is presented in sections for the respective efforts from each laboratory. Section 2.0 presents sample selection, origin, and details, Section 3.0 presents the efforts from PNNL,

Section 4.0 presents the efforts from INL, and Section 5.0 presents the overall summary of the work.

1.1 Background

Reactor core environments are harsh, extreme environments for materials to exist in. Irradiation and fast neutrons within the core of a reactor can alter and damage cladding matrices, in turn generating irradiation-induced defects in the material, such as vacancies and interstitial atoms. Should the vacancies cluster, material void swelling and embrittlement can occur, typically at grain boundaries. Irradiation defects, such as microstructural defects, are able to trap hydrogen as hydrogen can adsorb to these readily (R.A. Oriani 1970). Hydrogen trapping is a known concept in hydrogen-metal interactions (M.P. Puls 2012).

Zircaloy itself is highly resistant to irradiation induced void swelling and voids are generally suppressed under light water reactor (LWR) conditions. Vacancy clusters normally collapse within the material into dislocation loops (S. Di et al. 2015). However, at high fluence or high temperatures (noted typically greater than 360°C to 400°C), vacancies have the ability to grow into voids as opposed to collapsing into dislocation loops (S. Di et al. 2015; D.I.R. Norris 1972; S.D. Harkness et al. 1971). Within the zircaloy substrate itself, hydrogen solubility is temperature dependent and relatively low, typically resulting in hydride precipitate formation as cladding cools. Depending on the sample temperature and the cool down when no longer in testing, there is potential for hydride precipitation and trapping of dissolved hydrogen within the cladding matrix. This trapped hydrogen, when adsorbed on a void surface, can recombine to form H_2. Not only does the trapped gas pose an issue for pressure build up within a void, but to escape the void the H_2 must first disassociate.

Chromium coatings on zircaloy cladding have emerged as leading coatings in ATF to aid in the mitigation of corrosion and to minimize the hydrogen uptake. With waterside corrosion being a primary source of hydrogen pickup in uncoated zircaloy, the coating acts to form a stable thin chromium oxide (Cr_2O_3) layer that protects from high temperature water, reduces corrosion kinetics, and significantly reduces hydrogen permeability through the Cr-coating in comparison to zirconia (Zr_2O) (J.-C. Brachet et al. 2019; J. Bischoff et al. 2018; J. Krejčí et al. 2020; H. Yeom et al. 2019; B. Maier et al. 2018; H.-G. Kim et al. 2018). Several methods have been explored for the deposition of coatings on the surface of cladding. These include CS and PVD coatings, both of which have shown promise as a method for applying protective coatings in the nuclear industry (M. Ševeček et al. 2018; I. Alakiozidis et al. 2025; H. Yeom et al. 2019).

In CS deposition methods, using helium or nitrogen gas, solid powder particles are propelled to a substrate, with the benefit that the process occurs at relatively low temperatures (I. Alakiozidis et al. 2025). For samples studied here, the CS process used N_2 as the carrier gas to the zircaloy substrate. Typically, CS coatings are observed to have a layered or lamellar structure due to the nature of the deposition – particles “splat” on the interface and become layered to generate the thickness – with grain boundaries parallel to the surface. Cold spray techniques are advantageous in the throughput of samples due to the deposition rate, the variability on thicknesses of coatings that can be achieved, and low substrate temperature, preventing substrate alteration (H. Singh et al. 2022; *High Pressure Cold Spray: Principles and Applications* 2016).

In PVD methods, or thin film processes, a chromium target is bombarded with ions (typically argon), vaporizing the solid target material in a vacuum chamber. The vaporized material is then condensed onto a specimen, in this case zircaloy cladding, atom by atom, which generates a

thin external layer (D.M. Mattox 2010). These coatings typically exhibit columnar grain boundaries perpendicular to the surface. Advantages to the PVD coating method are the maintenance of a low temperature in the substrate during deposition, preventing substrate alternation, dense coatings, good adhesion, and excellent thickness control (J. Bischoff et al. 2018).

2.0 Sample Selection, Origin, and Receipt

The objectives of the project were achieved through detailed PIE of select Cr-coated cladding and weld samples that were irradiated in the MITR and BR2 test reactors. Samples were selected carefully for analysis after being fabricated and supplied by Westinghouse. Comparable as-manufactured materials were also provided for comparison to the irradiated materials.

2.1.1 Sample Naming Conventions

A sample naming convention was adopted by the collaborators to facilitate and streamline sample identification. The sample naming convention was:

[Origin][Position][Sample#] – [Material] – [Coating][Specimen #]

- **Origin** – the source of the sample; M is MITR, B is BR2, and R is reference material (i.e., as-manufactured)
- **Position** – the sample's position within the originating facility; I is for in-core (MITR or BR2), O is for out-of-core (MITR only), and C for the Cortellini loop (BR2 only). This field is omitted for reference material
- **Sample #** – the sample number for samples originating from the BR2 MISTRAL-N rig; omitted for all other samples
- **Material** – the material type; Z is Optimized ZIRLO™, ZY is zircaloy 4
- **Coating** – the coating method or sample identifier; C is cold spray, P is physical vapor deposition, U is uncoated, and L is laser weld
- **Specimen #** – a sequential number assigned to each specimen cut from a parent sample

For example, MI-Z-C1 is a sample from MITR, in-core; Optimized ZIRLO™, cold-spray coated; and the 1st specimen cut from its parent sample.

To complement and compare materials, as-manufactured materials were transferred to the labs to provide materials for baseline testing. Samples were sent to PNNL and INL (uncoated, Cr-coated through CS, and Cr-coated through PVD), where coating thickness depended on the preparation method. The as-manufactured material matrix is shown in Table 2.1.

Table 2.1. As-manufactured sample matrix.

Original Sample Name	Project Naming Convention	Preparation Method	Sample Length, mm	Coating thickness, µm
Sample C	R-Z-C1	Cold Spray Cr-coated Optimized ZIRLO™	116	25
Sample D	R-Z-C2	Cold Spray Cr-coated Optimized ZIRLO™	116	25
Sample E	R-Z-C3	Cold Spray Cr-coated Optimized ZIRLO™	116	25
Sample F	R-Z-C4	Cold Spray Cr-coated Optimized ZIRLO™	116	25
Sample H	R-Z-C5	Cold Spray Cr-coated Optimized ZIRLO™	116	25
Sample I	R-Z-U1	Uncoated Optimized ZIRLO™	71	--
Sample P	R-Z-U2	Uncoated Optimized ZIRLO™	71	--
Sample N	R-Z-P1	PVD Cr/Nb-Coated Optimized ZIRLO™	116	14 (7/7 Cr/Nb)
Sample X	R-Z-P2	PVD Cr-coated Optimized ZIRLO™	178	7

2.2 Massachusetts Institute of Technology Reactor Samples

Westinghouse irradiated variants of CS and PVD Cr-coated cladding in the MITR and also tested equivalent samples in a water loop out-of-core. Cladding tubes were open and not sealed in this irradiation experiment, with water at a controlled chemistry flowing on the outside and inside of the tubes.

Normal practice for the water chemistry at the MITR is to run 50 cc/kg hydrogen, running mid-cycle boron and lithium (800 ppm boron target, lithium concentration to pH 7.2) to emulate mid-cycle PWR conditions. Water chemistry is constantly monitored using hydrogen and oxygen concentration measurements in conjunction with online pH monitoring. Colorimetric analysis is performed on grab samples for measurements of the boron and lithium content. The same water flows to both the in-core and out-of-core samples; thus, they see equivalent water chemistry in both conditions. Similarly, corresponding in-core and out-of-core samples experienced the same loop exposure history, including identical time in water, equivalent full power days (EFPD), and hot days (i.e., days in which the core is electrically heated). The key distinction between the two populations is therefore irradiation. That is, in-core samples received the full neutron flux, while out-of-core samples served as thermally and chemically exposed but unirradiated controls.

2.2.1 In-Core Sample Conditions

Irradiation of the samples was performed in a water loop installed on the MITR 6 megawatt (MW) research reactor. Samples were contained in an autoclave in the core region, where water flowed upwards around the samples in the in-core region (and then to samples located in an out-of-core region) before recirculating. For unsealed tube samples there is a small flow of chemistry controlled water through the center of the samples, but the primary flow path is over the outside surface of the samples.

The in-core samples were irradiated to ~0.5 displacements per atom (dpa) at 298±1°C. Temperature variation between the in-core and out-of-core samples is negligible, because the nuclear heating of the reactor is low. The loop temperature is instead set using electrical heating outside of the core. As such, the water temperature in the experiments is highly stable in both regions and independent of whether the reactor is operating or not. While the samples

themselves generate a small amount of heat when the reactor is operational, this contribution is minimal and not enough to induce significant temperature variations (there is only a ~2°C delta across the core).

The in-core samples from MITR received at PNNL for PIE were all Optimized ZIRLO™ and comprised four coating/treatment variants: uncoated, Cr-coated by N_2 cold spray, Cr-coated by PVD (magnetron sputtering), and laser welded samples with a cold-sprayed Cr coating. Table 2.2 summarizes each sample received, including the original sample name, the project naming convention identifier, treatment method, as-received length, and coating thickness.

Table 2.2. MITR in-core sample matrix.

Original Sample Name	Project Naming Convention	Preparation Method	Sample Length, mm	Coating thickness, µm
V52-3	MI-Z-U1	Uncoated Optimized ZIRLO™	12.5	N/A
NC5-1	MI-Z-C1	N_2 CS Cr-coated Optimized ZIRLO™	30	15-25
IB5-1	MI-Z-P1	PVD Cr-coated Optimized ZIRLO™	12.5	5
IB10-1	MI-Z-P2	PVD Cr-coated Optimized ZIRLO™	30	10
LW-1	MI-Z-L1	Laser weld, CS Cr-coated laser welded segments	12.5	15-25

2.2.2 Out-of-Core Sample Conditions

Equivalent out-of-core samples were exposed at nearly identical temperature conditions (296±1°C). These samples were placed directly above the core-tank at about 6-8 inches, receiving the same circulating water as in-core samples. The total dose observed at the top of the core is about 50% lower and reduced by an order of magnitude for every foot travelled. As such, these samples observe an order of magnitude difference in gamma radiation dose but have essentially no fast neutron flux (small thermal neutron dose).

The water chemistry does change slightly as it exits the core of the reactor and flows past the out-of-core samples, since the in-core neutron flux is no longer present. However, the temperatures and water chemistry remain nearly identical between the in-core and out-of-core regions due to the control methods used by MITR (as noted in Section 2.3.1).

Out-of-core equivalent samples were comprised of three coating/treatment variants: uncoated, Cr-coated by N_2 cold spray, and Cr-coated by PVD (magnetron sputtering). Table 2.3 summarizes each sample received, including the original sample name, the project naming convention identifier, treatment method, as-received length, and coating thickness.

Table 2.3. MITR out-of-core sample matrix.

Original Sample Name	Project Naming Convention	Preparation Method	Sample Length, mm	Coating thickness, µm
V52-5	MO-Z-U1	Uncoated Optimized ZIRLO™	12.5	N/A
NC5-5	MO-Z-C1	N_2 CS Cr-coated Optimized ZIRLO™	12.5	15-25
IB5-3	MO-Z-P1	PVD Cr-coated Optimized ZIRLO™	12.5	5
IB10-3	MO-Z-P2	PVD Cr-coated Optimized ZIRLO™	12.5	10

2.3 Belgian Reactor 2 Cladding

The MISTRAL-N irradiation rig fabricated at SCK CEN (Belgian Nuclear Research Reactor) for the H2020 IL TROVATORE program was utilized. The rig carries three needles, each of which can hold 17 cladding rodlets of standard length (30 mm) or fewer for larger lengths. Conditions for samples in the rig were 320°C with PWR like chemistry. The rig itself does not have heating capabilities, but rather relies on gamma heating to achieve the irradiation temperature. The rodlets in the rig were filled with alumina (Al_2O_3) dummy pellets, backfilled with helium, and sealed via tungsten inert gas (TIG) welding of end plugs.

Six samples were identified for testing under the GAIN voucher: sample 1, Cr/Nb coated by PVD (length [L] = 116 mm, coating thickness ≈7/7 µm); samples 2 and 6, Cr-coated via CS (L = 116 mm & 161 mm, respectively, coating thickness ≈25 µm); samples 3 and 4, uncoated Optimized ZIRLO™ (L = 71 mm); and sample 5, Cr-coated via PVD (L = 116 mm, coating thickness ≈ 7 µm).

Unfortunately, due to logistical constraints of shipping the BR2 materials to the United States and associated labs, the samples associated with the rig remain at BR2 for the time being. No testing or results were obtained on these samples.

2.4 Sample Imaging and Visual Appearance

The MITR samples were tested and shipped directly to Westinghouse. Westinghouse then cut the samples into two specimens and transferred the respective samples to PNNL and INL. Images of the samples were taken at Westinghouse prior to sectioning them, which are shown in Figure 2.1.

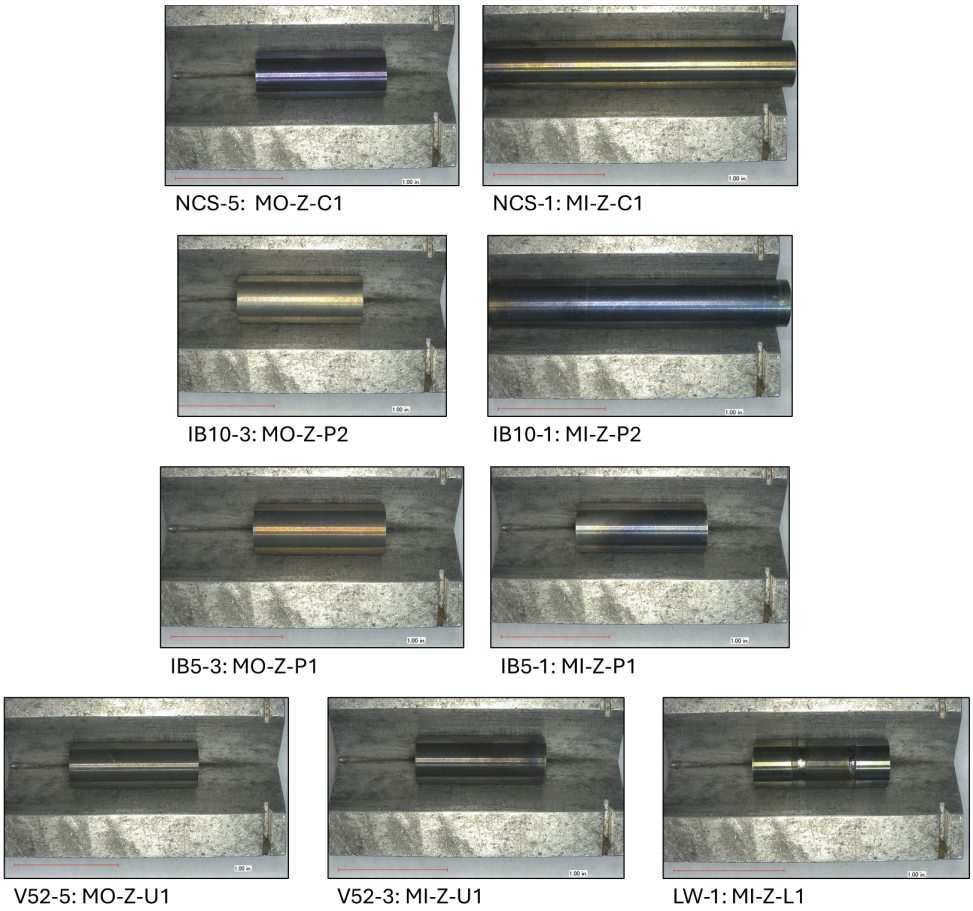

Figure 2.1. Sample images collected at Westinghouse prior to sectioning the material.

Visually, it was noted that the MITR samples differ in color, with some appearing gold/straw colored and others appearing to have a blue/purple hue. Despite identical exposure conditions to the oxidizing medium (i.e., the chemistry-controlled water loop), the samples show color differences characteristic of thin-film optical interference, where thickness variations of only tens of nanometers can produce visibly distinct hues (X. Shi et al. 2023; D. Guo et al. 2025).

Contributing factors that are known to affect the oxide thickness include the material (i.e., Zr versus Cr), the crystallographic orientation of the outer coating, orientation of grain boundaries, and the coating thickness itself.

3.0 PNNL – Methods, Results, and Discussion

3.1 Materials and Methods

3.1.1 Metallographic Sample Preparation

Initial efforts with the as-manufactured materials were focused on the potting and polishing of cut sub-samples to optimize the preparation techniques of the samples. To explore this, an aqueous polishing recipe and non-aqueous polishing recipe were tested on as-manufactured materials with follow on microscopy efforts to confirm ideal polishing conditions. Non-aqueous techniques were explored to determine if aqueous techniques artificially created hydrides in the substrate. No evidence of this was observed, and as such aqueous techniques were pursued due to superior quality.

From the parent samples, sub-samples, nominally 2 mm (0.12 inches) in length, and were cut using an IsoMet low speed saw to characterize the samples and prepare them for metallographic examination following ASTM International E3-11 (2017), *Standard Guide for Preparation of Metallographic Specimens* (ASTM 2017). Sub-sample rings were mounted in two-part Buehler EpoThin™ 2 epoxy resin and hardener. Mounted samples were placed in a vacuum for several minutes to remove any trapped gas. They were then allowed to cure overnight at room temperature. Cured epoxy samples were then moved to a Pace Technologies® multistage grinder-polisher. Prior to grinding, all samples underwent backing – the process of grinding the back side of the sample puck to provide a flat surface parallel to the sample surface. Backing was performed with 240 grit silicon carbide (SiC) paper for 60 seconds at 70 psi. Following backing, samples were ground with SiC paper in sequential steps at 240 and 400 grit. Between steps samples were cleaned via ultrasonic cleaning in a deionized water bath for 30 seconds. Samples were then polished using Pace® TEXPAN and ATLANTIS polishing cloths with Buehler MetaDi™ Supreme polycrystalline diamond suspension in 9, 6, 3, and 1 micron (µm) particle size. The final polishing step is performed with a Pace® vibratory polisher, Pace® MICROPAD polishing cloth, and Buehler MasterMet™ colloidal silica polishing suspension with the samples placed in a metal mount. Post polish, samples were cleaned in a soap and water ultrasonic bath, rinsed with deionized water, and rinsed with ethanol before air drying. Procedural steps are noted in Table 3.1.

Table 3.1. Grinding and polishing procedural steps.

Step	RPM Set, Head/platen	Force, psi	Time
Backing	200/200	~70	60 s
240 grit SiC	200/200	~70	60 s
240 grit SiC	200/200	~70	60 s
400 grit SiC	200/200	~70	60 s
400 grit SiC	200/200	~70	60 s
400 grit SiC	200/200	~70	60 s
9 µm diamond suspension	150/150	~75	5 min
9 µm diamond suspension	150/150	~75	5 min
6 µm diamond suspension	150/150	~75	7 min
3 µm diamond suspension	150/150	~65	5 min
1 µm diamond suspension	150/150	~65	5 min
0.06 µm colloidal silica	1 revolution per 10 seconds	~300 grams	~20 – 30 hr

3.1.2 Optical Microscopy

Metallographic examination included image collection and observations using an Olympus DSX510 optical microscope (OM). Weekly calibration verifications are completed on the OM using the National Institute of Standards and Technology (NIST) standards by following ASTM E1951-14, *Standard Guide for Calibrating Reticles and Light Microscopy Magnificati*ons (ASTM 2019). Optical images show broad characteristics of the samples, can be used to determine the inner diameter (d_i) and outer diameter (d_o) of the cladding, and can allow for thickness measurements on the Cr-coating. Equipped with a 5× and 20× lens, an overview of the cladding was captured through stitching together 144 images with the 5× lens. Individual quadrants of the cladding were captured using the 20× lens and stitching together 64 images. Finally, individual images were captured for specified areas of interest. While exterior oxide can be observed using the OM, the thickness was typically too small to quantify on the OM. Uncertainty measurements for the inner and outer diameter measurements were ±3 µm, while the uncertainty on the layer thickness was ±0.5 µm.

3.1.3 Microhardness Testing

Some polished samples were transferred to a microhardness tester (Sun-Tec CM-802AT) and tested per ASTM E92-17, *Standard Test Methods for Vickers Hardness and Knoop Hardness of Metallic Materials* (ASTM 2023). The tester was verified prior to use with three hardness standards, which have measured certified values of 182 HV0.3 ±2.6 HV0.3, 243 HV0.3 ±3.9 HV0.3, and 313 HV0.3 ±6.3 HV0.3; the verification passed if the measured value of the standard was within 2%. Following indentation, the indents were measured using a 50× lens with a resolution of 0.42 µm per ASTM E92-17 (ASTM 2023). The total estimated uncertainty for an individual microhardness measurement was ±6 HV at 300 gf, which is the result of the combination of the individual uncertainties. All indents and measurements were collected at room temperature.

3.1.4 Chemical Etching

Some polished samples were exposed to an etching solution of 70 mL H_2O_2:40 mL HNO_3:4 mL HF, at concentrations of 30-50% H_2O_2, 70% HNO_3, and 48-52% HF as prescribed by Westinghouse. Following etching, samples were re-examined using the OM to visualize the hydrides.

3.1.5 Scanning Electron Microscopy

The imaging of the non-irradiated specimens was performed using an FEI (Thermo-Fisher, Hillsboro, OR) Quanta250 Field Emission Gun (FEG) scanning electron microscope (SEM) equipped with a backscattered electron (BSE) detector and an EDAX (EDAX Inc., Draper, UT) Hikari™ electron backscattered diffraction (EBSD) system. Irradiated specimens were examined with a Thermo-Fisher Apero™ SEM equipped with an Oxford Instruments 100 mm^2 UltimMax™ energy-dispersive x-ray spectroscopy (EDS) running Aztec™ software.

The zircaloy materials were non-conducting and were examined under low vacuum conditions (20 to 40 Pa water vapor). By running at 10 keV, low beam current, it was possible to reveal the grain structure through electron channeling contrast using the backscattered detectors under high contrast conditions (A. Devaraj et al. 2021). At lower energy, electrons can be channeled along specific crystallographic directions with little backscattering which results in the grain structure becoming visible. The analysis of oxygen in the presence of chromium can present problems with EDS because of peak overlap. However, the Aztec software was able to deconvolute the O-K signal from the Cr signals by using the expected intensity ratio of the Cr-K and Cr-L lines.

3.1.6 Transmission Electron Microscopy

Lamella were prepared for transmission electron microscopy (TEM) using a Thermo Fisher Scientific Helios 5 UX DualBeam for focused ion beam (FIB) lift outs. A Pt-protective coating was deposited prior to milling. The TEM lamella were cryo-thinned using a Thermo Fisher rotatable cryo-stage module at −170°C using 30 kV to bulk thin and 5 kV for final thinning to minimize hydride damage.

Lift-out samples were examined on a JEOL Inc., (Akishima, Tokyo, Japan) GrandARM 300F STEM/TEM equipped with a Gatan Inc., (Pleasanton, CA, USA) OneView digital camera, dual Centris EDS detectors, and a Gatan image filter for electron energy loss spectroscopy (EELS) and energy filtered transmission electron microscopy (EFTEM). In this study, elemental mapping was conducted using the three-window EFTEM method for the Cr-$L_{2,3}$, and Zr- edges. This involved collecting energy-filtered images (pre-edge, 1, 2, and post-edge images) to subtract the background. A thickness map was also collected to confirm the conditions of the analyzed area. The 4D-scanning transmission electron microscopy (STEM) data were analyzed using Gatan DigitalMicrograph scripts. Selected area electron diffraction (SAED) was analyzed using CrysTBox software (M. Klinger 2017).

3.1.7 Hydrogen Analysis

The LECO ONH836 Oxygen/Nitrogen/Hydrogen analyzer measures total content of these elements in steel, refractory metal, and other inorganic materials. Samples are pre-weighed and placed in a graphite crucible, which is then heated in an impulse furnace to release analyte gases. Helium, an inert gas carrier, sweeps the released analyte gases out of the furnace,

through a mass flow controller, and through a series of detectors. The liberated oxygen in the sample reacts on combustion with the graphite crucible to form carbon monoxide (CO) and carbon dioxide (CO_2), which are detected using non-dispersive infrared (NDIR) cells.

Infrared (IR) energy is absorbed by analyte gas molecules at unique IR wavelengths, and as such, incident IR energy at these wavelengths is absorbed as the gases pass through NDIR absorption cells. The gas continues through a heated copper bed, oxidizing CO to CO_2, and hydrogen gas (H_2) to water (H_2O). The gas passes through NDIR cells detecting H_2O and CO_2; these gases are then scrubbed out of the carrier gas stream and carrier gas is added to compensate for gas loss. Finally, the remaining gas is carried through a thermal conductivity detector to detect nitrogen. For the purposes of this work, only the hydrogen was quantified in the samples, which is an indication of total content, and not limited to the substrate or coating. The instrument reports results in weight parts per million (wppm). For those pieces with duplicates the weighted average is presented (P.R. Bevington 1969).

Samples for hydrogen analysis on the LECO instrument were prepared by quartering cladding rings using an IsoMet low speed saw. Quarters were cleaned with acetone and placed in pre-tared sample vials. Vials were weighed with the quartered samples and a sample mass was determined.

Samples were run in a graphite crucible with a nickel basket and tin flux to accelerate sample combustion. Prior to analysis the system is prepared with a blank calibration to establish the instrument “zero”, followed by a series of certified standards to generate a calibration curve based on total analyte mass. Sample results are compared against the calibration curve to determine the total hydrogen concentration in the sample. Previous work at PNNL has shown the uncertainty in LECO measurements to be ±10% (R.W. Shimskey et al. 2022b; R.W. Shimskey et al. 2022a).

3.2 Results

3.2.1 Non-Radiological Materials Analysis

Uncoated Optimized ZIRLO™ has shown reduced in-reactor corrosion, excellent dimensional stability, and similar creep results to ZIRLO® (B. Comstock et al. 2015; G. Pan et al. 2016).

3.2.1.1 Cold Spray Cr-Coated Materials

The Cr-coated reference materials provided were analyzed to understand the materials properties in comparison to the out-of-core and in-core comparable samples. The Cr-coating on the CS prepared materials were all noted to have a thickness of 25 µm on average.
The polished samples exhibited smooth surfaces with the Cr-coating clearly visible around the outer diameter. Discrepancies in the Cr-coating thickness were observed around the sample, as seen in Figure 3.1, due to the nature of the cold spray coating process.

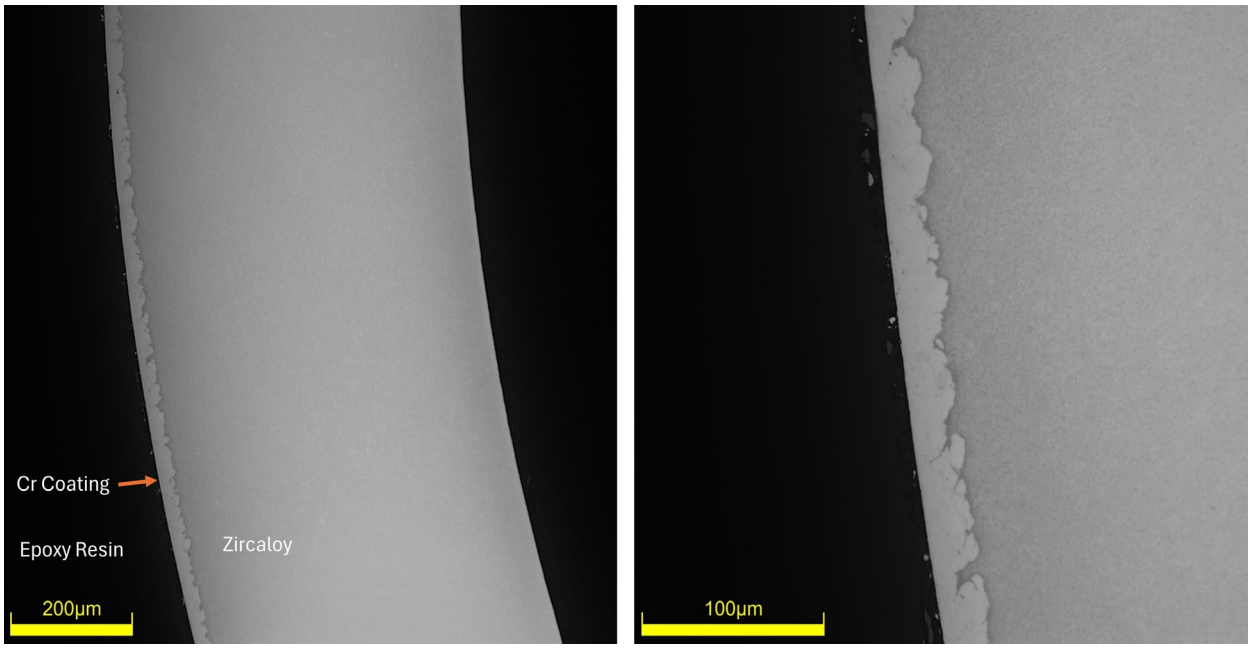

Figure 3.1. Optical microscopy of CS Cr-coated cladding showing a zoomed in portion of the coating and substrate interface.

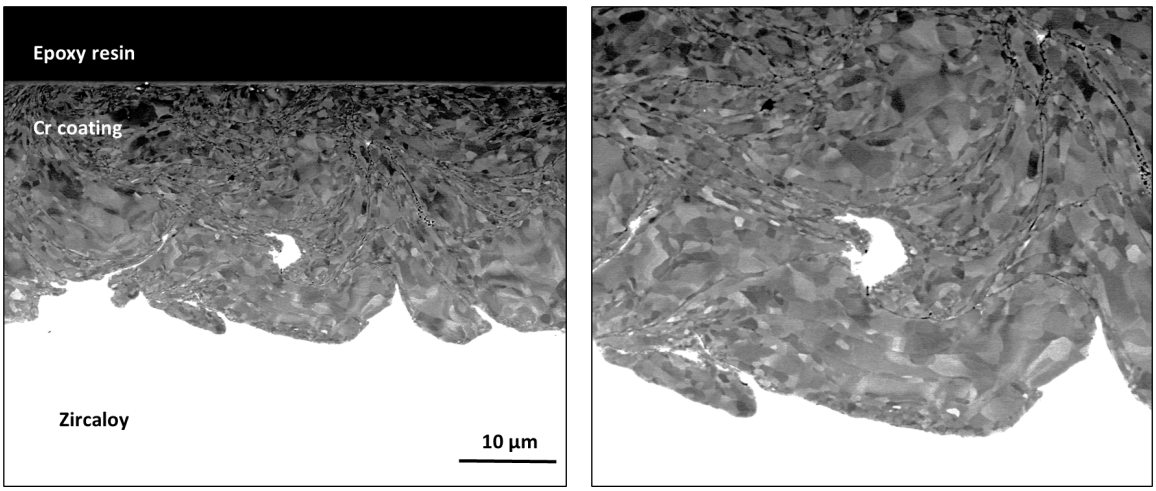

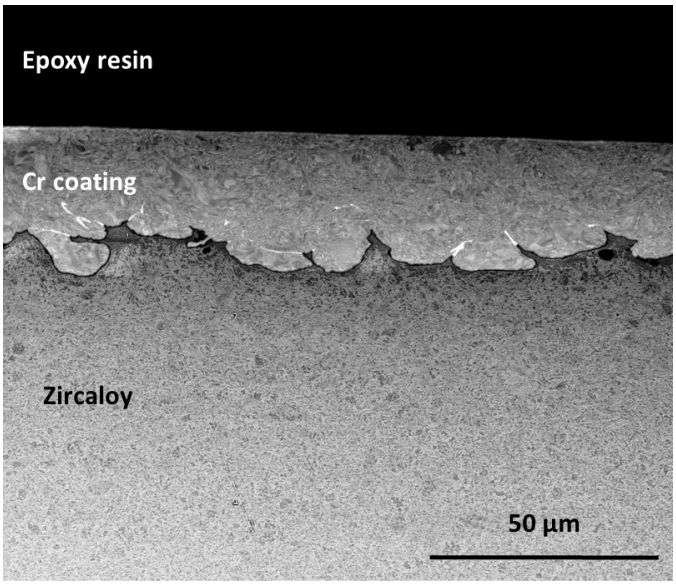

Figure 3.2. (Top) Scanning electron microscopy high contrast grain structure images shown on the zircaloy substrate. (Bottom) SEM-Backscattered Electron (BSE) image of the Cr-coated non-radiological cladding sample to illustrate the substrate and Cr-coating.

The Cr-coating shows random grain orientation throughout, Figure 3.2, as observed in the lack of texture originating from the coating process. Within the sample existed a mixture of large and small grains, possibly also suggesting recrystallization in highly deformed areas. Due to the nature of the cold spray process, the coating consists of “splat-like” features of severely deformed Cr powder particles.

High magnification images in Figure 3.2 show the presence of microcrack-like features and the occasional microporosity in the Cr-coating. Defects are present in the intrasplat space, which is expected as it is inherent to the cold-spray process.

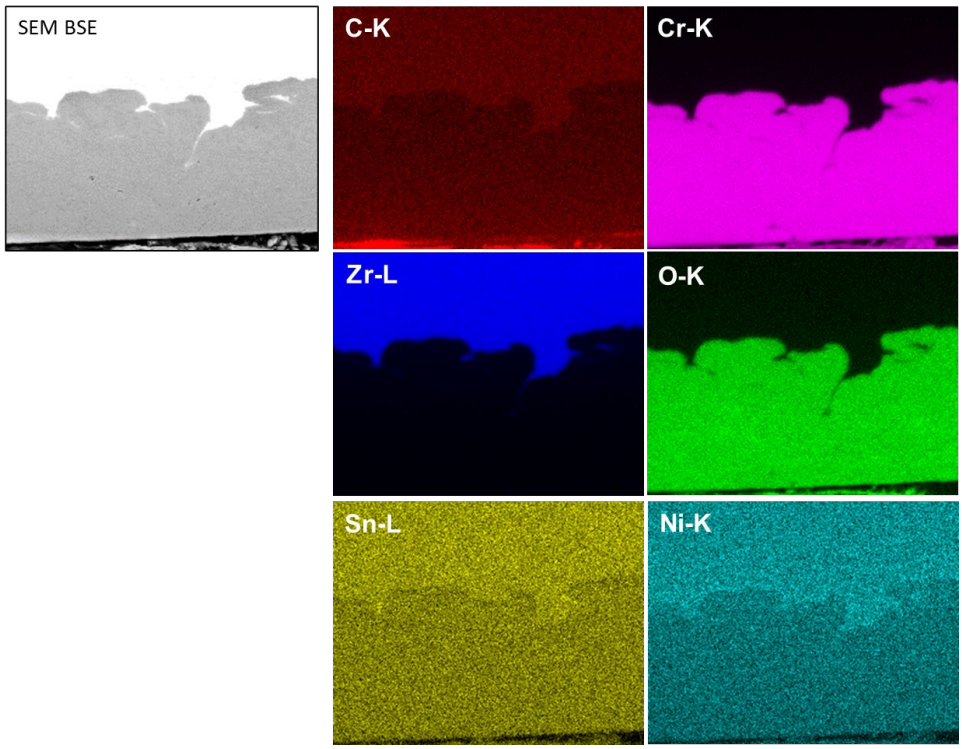

Figure 3.3. SEM-energy dispersive spectroscopy (EDS) mapping of the CS Cr-coated non-radiological material. The SEM-BSE is shown in the top left.

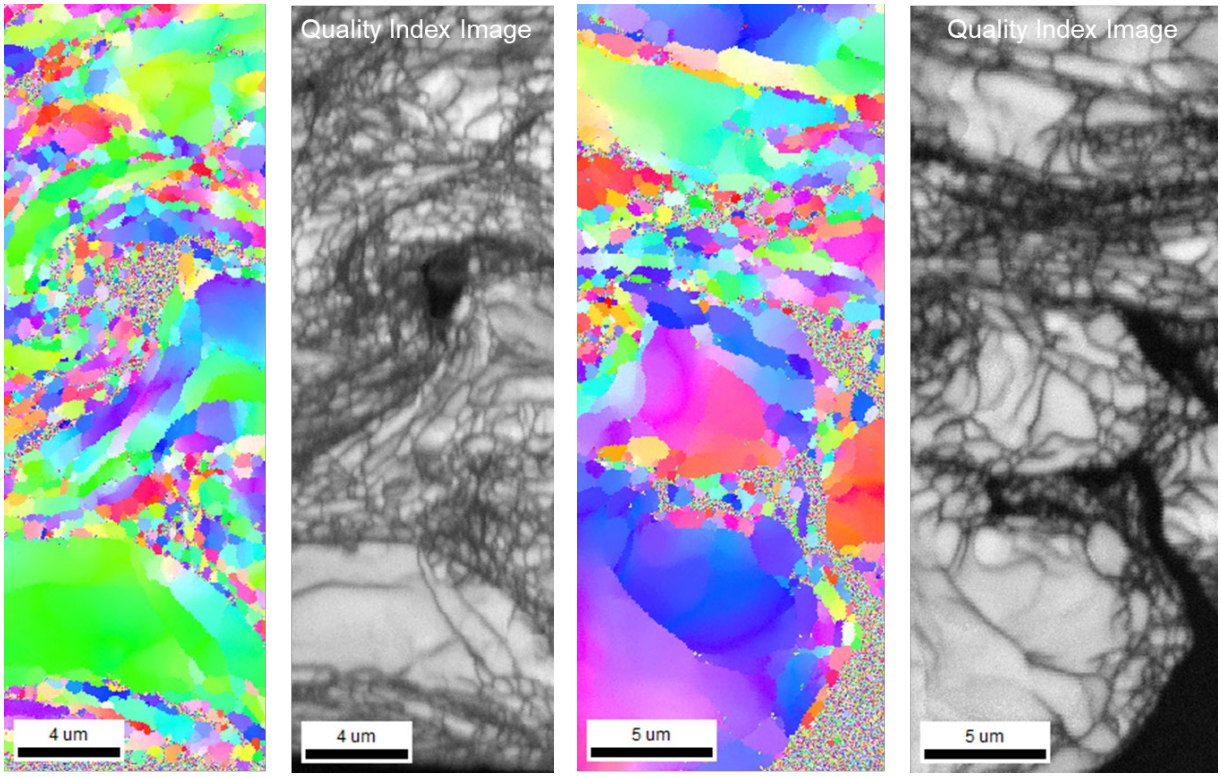

Figure 3.4. EBSD of the Cr-coated non-radiological cladding showing large grain orientation and a mix of large and small grains.

Microstructural analysis using scanning electron microscopy – energy dispersive x-ray spectroscopy (SEM/EDS) in Figure 3.3 and electron backscatter diffraction (EBSD) in Figure 3.4 of the cold spray reference sample showed severe deformation of the substrate/coating interface, as expected. While the substrate deformation promises mechanical interlocking of the coating, it can decrease the materials fatigue lifetime.

3.2.1.2 Physical Vapor Deposition Cr-coated Materials

The Cr-coating in the PVD specimen was thin and measured less than 10 µm, Figure 3.5. The chromium grains lined up perpendicular to the zircaloy surface, Figure 3.6.

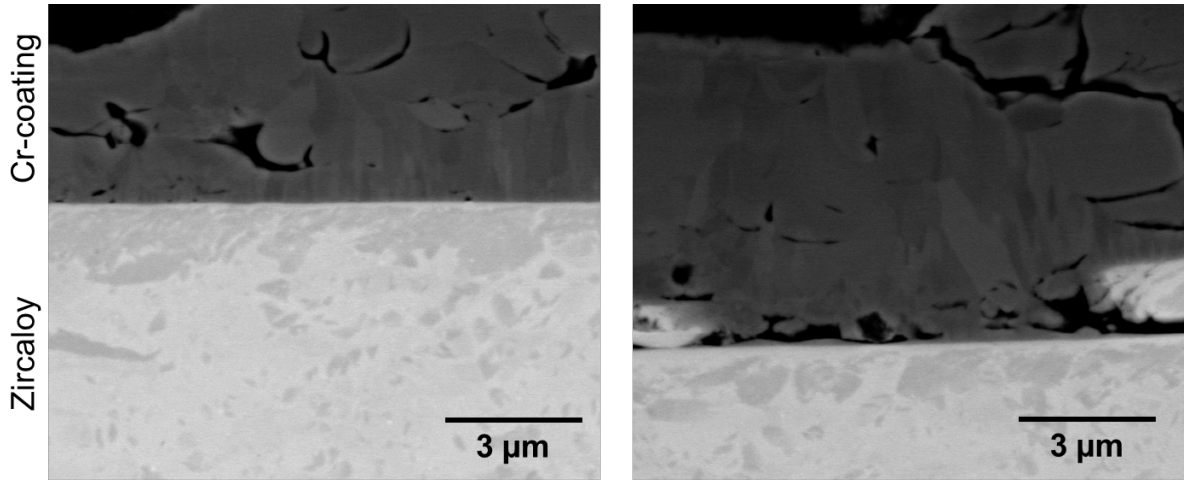

Figure 3.5. SEM images of the zircaloy substrate and the Cr-coating in R-Z-P1.

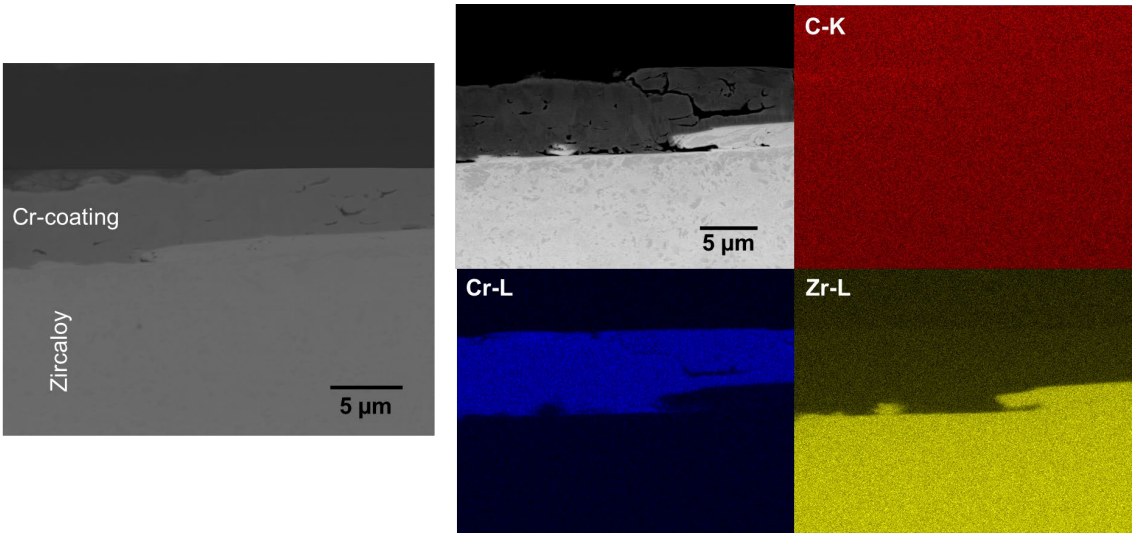

Figure 3.6. SEM/EDS elemental mapping of the PVD Cr-coated non-radiological material. The SEM-BSE is shown in the top left.

The grain structure of the Cr was prominent and visible in the microscopy images collected, Figure 3.7, showing a non-uniform grain distribution. It was noted that there were some cracks, pores, and voids existing within the coating. To fully visualize both the Cr and zircaloy substrate, a high contrast image was generated using two images collected. Microscopy images of the

chromium layer show both how thin the layer is, and further how the grains run perpendicular to the zircaloy surface.

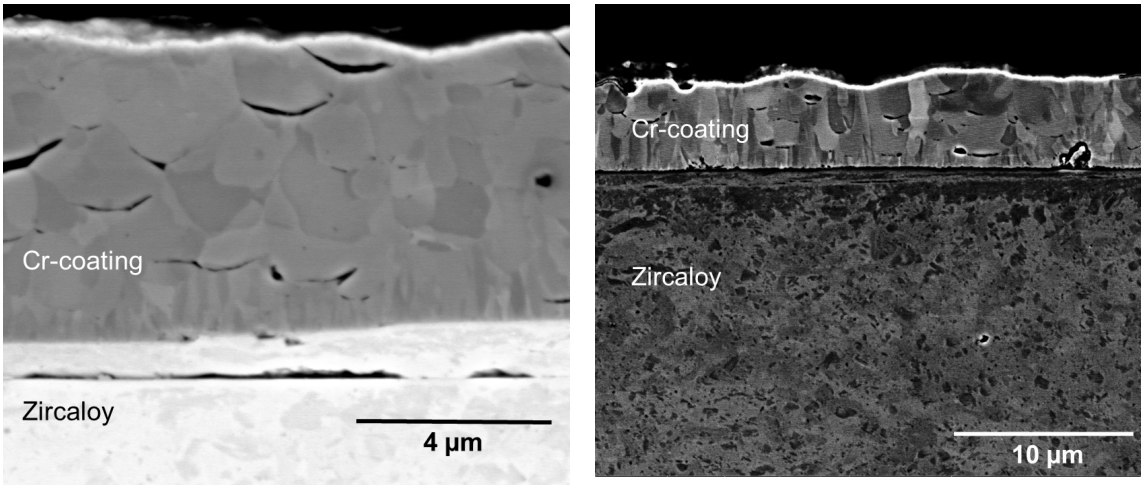

Figure 3.7. SEM images showing the grain structure of the PVD Cr-coated cladding. Left – cracks and pores visible in the PVD Cr-coating of the cladding. Right – a combination of two microscopy images showing both Cr and the zircaloy substrate at high contrast.

Electron backscatter diffraction maps taken at high magnification did not completely reveal the nature of the grain orientations, Figure 3.8. The phase in the Cr-coating matched well with body-centered cubic (BCC) structure. The presence of zirconium particles were noted in the Cr-coating, which is likely introduced during the deposition process. Unfortunately, even when angling the specimen, it was not possible to obtain an EBSD map of the grain orientations from the zircaloy. The lower magnification EBSD images collected illustrate the grain orientation and columnal microstructure of the PVD Cr-coating, matching to a BCC phase, Figure 3.9.

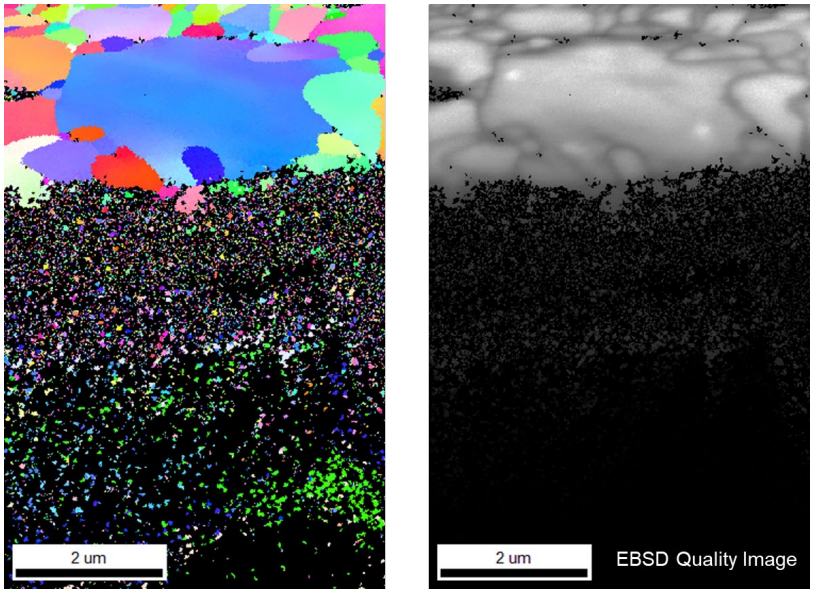

Figure 3.8. EBSD mapping collected at high magnification of the PVD Cr-coated non-radiological cladding.

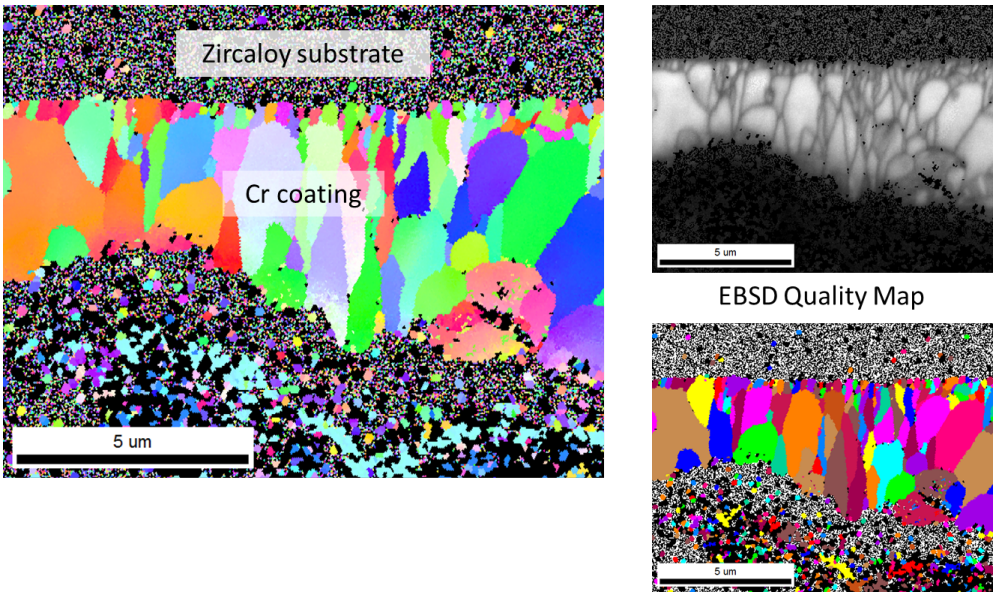

Figure 3.9. EBSD mapping collected at lower magnification of the PVD Cr-coated non-radiological cladding.

Ultimately, the results from the PVD sample specimen supplied show the sample was of lower quality compared to the CS sample as observed through microscopy techniques. The Cr-coating contained extensive crack networks and macro-voids, with some of these voids occasionally present at the substrate/coating interface. The thickness observed on the specimen was highly variable (~3 to 5 µm). Coating thickness variation and inherent defects in the Cr-coating are reflected in its fragility, as expressed in the detachment of the tops of the quasi-columnal grains during the solidification of the epoxy resin used for sample potting and polish.

The Cr-coating microstructure does not illustrate an optimized columnar microstructure as would be expected from mature PVD coatings (K. Quillin et al. 2022; Y. Zhang et al. 2025). Experimental analysis indicates that the coating may have occurred in two stages; between the fine columnar grains at the coating/substrate interface and the coarser grains, there is an abrupt change in the grain morphology and many voids exist here. Further analysis of the reference PVD materials were not recommended based on the appearance of the reference sample.

3.2.2 Radiological Material Analysis

3.2.2.1 Out-of-Core Uncoated Materials

Uncoated materials that were subjected to the same conditions as Cr-coated cladding were tested to aid in interpretation of the impacts of the Cr-coating.

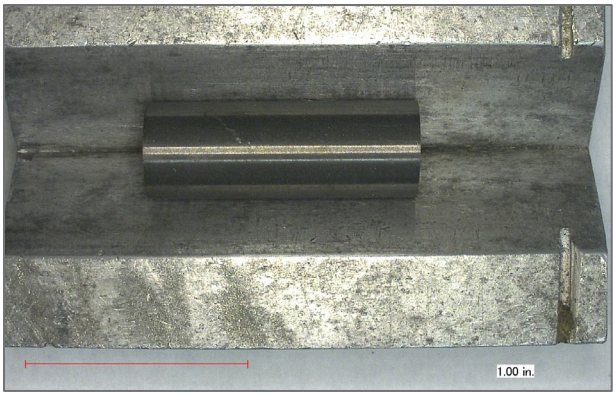

Figure 3.10. Out-of-core uncoated sample MO-Z-U1.

Prior to metallographic preparation, the parent sample exhibited a metallic finish, showing a silver hue, as seen in Figure 3.10. From the parent sample, the cladding was cut to 3 mm specimen rings and potted and polished per Section 3.1.1 through 3.1.3.

The polished uncoated specimen from MITR that experienced the out-of-core conditions exhibited a smooth polished surface with no observed hydriding, as seen in Figure 3.11. Minor imperfections or deformations observed in the optical microscopy images were attributed to remaining aqueous phase during the preparation process(see the line observed in quadrant A, Figure 3.11), and minor imperfects as a result of prior handling (as noted in quadrant A, Figure 3.11).

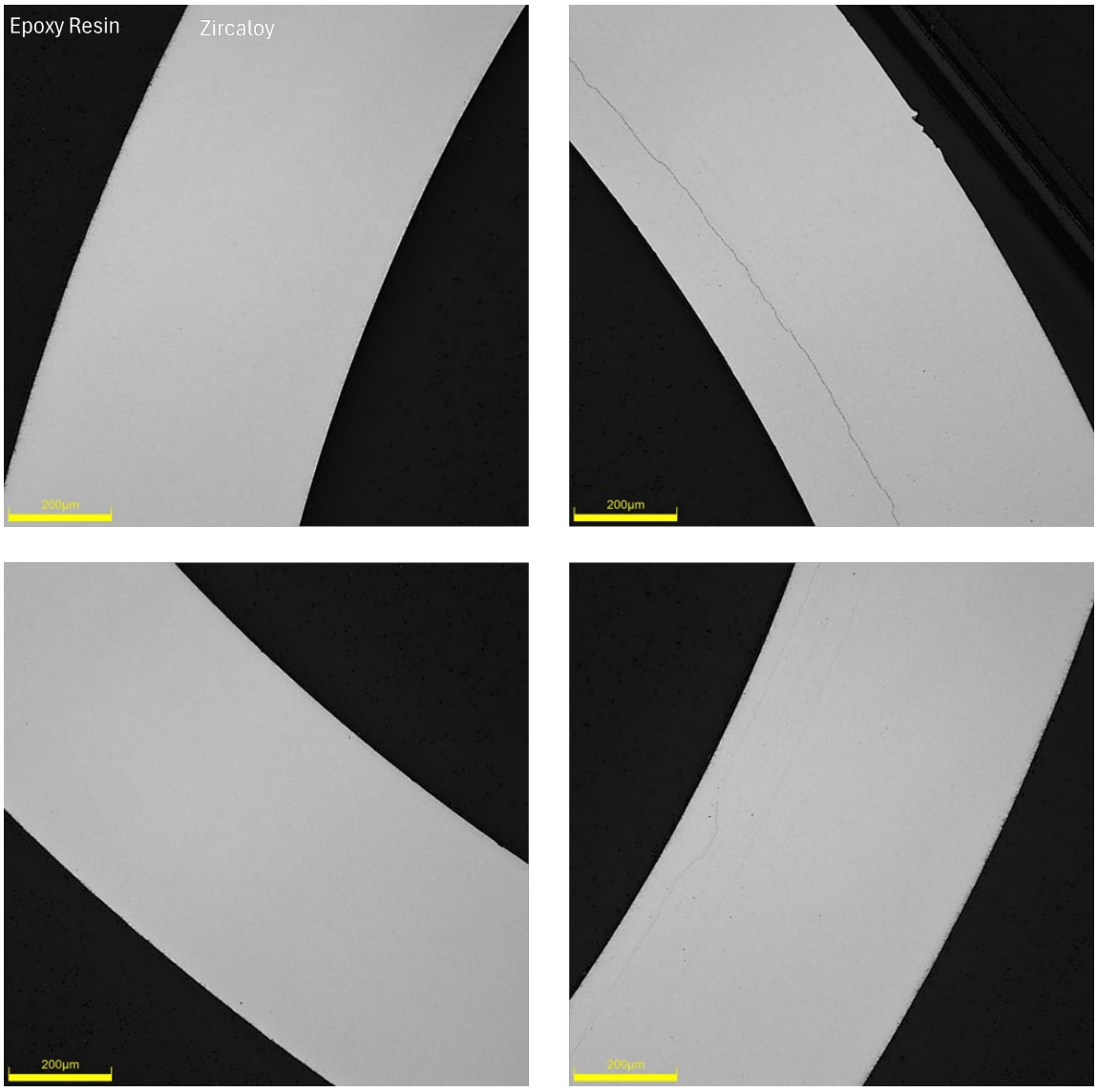

Figure 3.11. Optical microscopy of uncoated MO-Z-U1-1 S1 showing portions of quadrants A, B, C, and D (clockwise from the top right).

A second polished uncoated specimen from the MITR exposed to out-of-core conditions from the same parent sample also exhibited a smooth polished surface with no observed hydrides, Figure 3.12. This sample exhibited some minor debris remaining on the sample as a consequence of sample preparation – the dark spots on the cladding observed (see quadrant B and C in Figure 3.12).

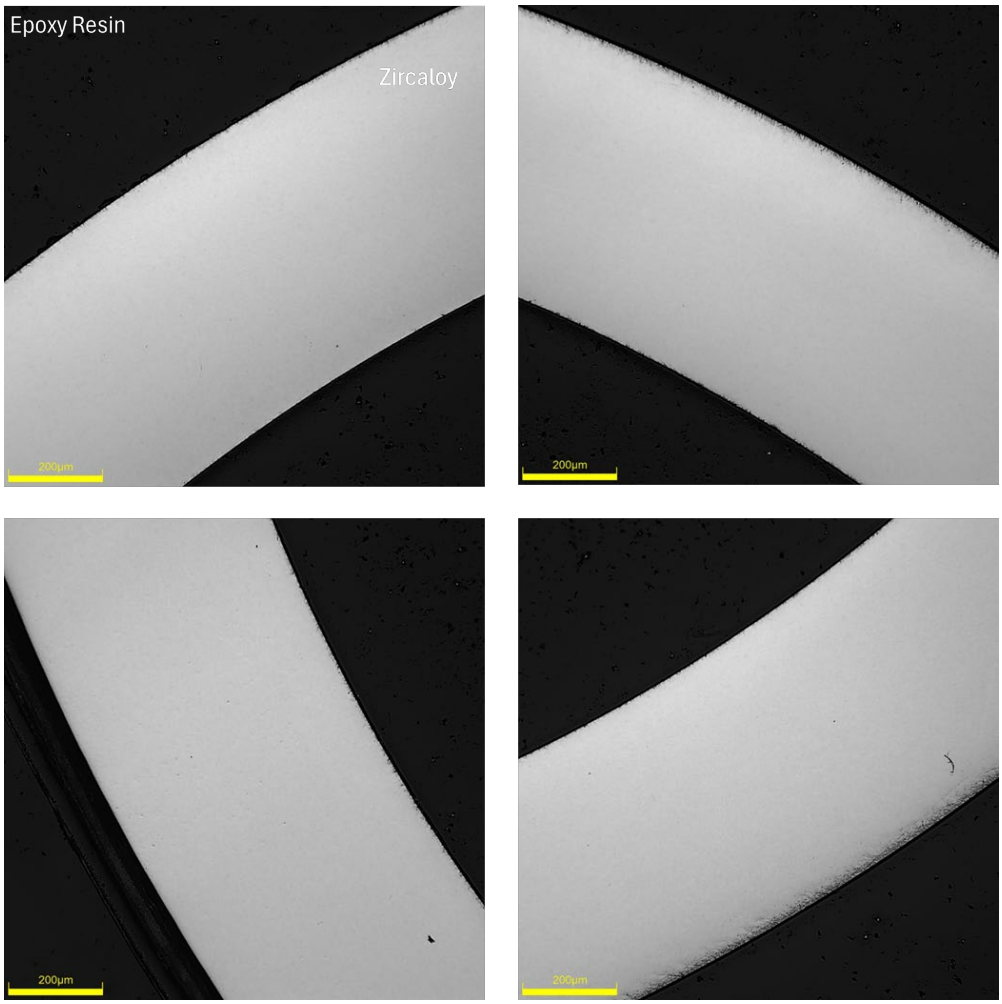

Figure 3.12. Polished OM images of uncoated MO-Z-U1-1 S2 showing portions of quadrants A, B, C, and D (clockwise from the top right).

From the out-of-core uncoated reference materials studied, no notable defects or hydrides were observed. Oxide coating on the inner and outer walls was not easily viewed or identified using OM, indicating any oxide layers present were minimal.

The out-of-core uncoated material was tested using the LECO instrument for total hydrogen content in the bulk sample. Total hydrogen content for the out-of-core sample MO-Z-U1 was 12 wppm hydrogen.

3.2.2.2 In-Core Uncoated Materials

Uncoated materials that were positioned in-core for testing were also prepared in 3 mm specimen rings and potted and polished per Section 3.1.1 through 3.1.3. From parent sample MI-Z-U1-1, samples S1 and S2 were cut and analyzed. Visually, before metallography preparation, the sample exhibited a silver hue, with slight darkness observed on one end, Figure 3.13.

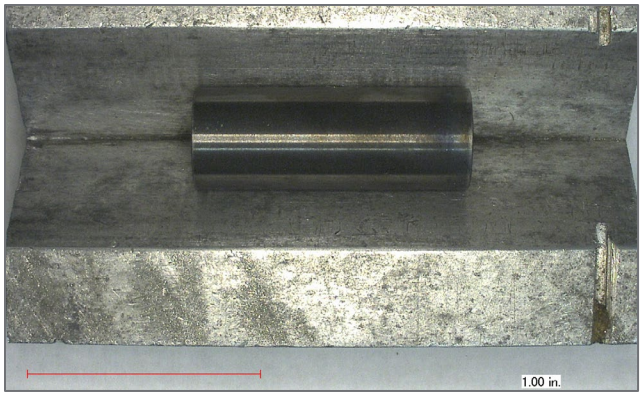

Figure 3.13. In-core uncoated sample MI-Z-U1.

The in-core polished uncoated specimens from MITR exhibited smooth, polished surfaces with no observed hydrides at lower magnifications. Minor imperfections in the optical microscopy images were attributed to imperfections from sample preparation in potting and polishing (as noted in all quadrants in Figure 3.14).

Two samples from the uncoated in-core sample were prepared (S1 and S2) to allow for comparison (Figure 3.14). In both cases, no notable defects were observed. There was no thick oxide coating identified on the inner or outer diameter through OM imaging.

The total hydrogen concentration was measured using the LECO analyzer, which is an indication of total hydrogen in the substrate and the coating. Total content for MI-Z-U1 S1 was 20 wppm hydrogen. This result was slightly higher than the out-of-core equivalent uncoated sample.

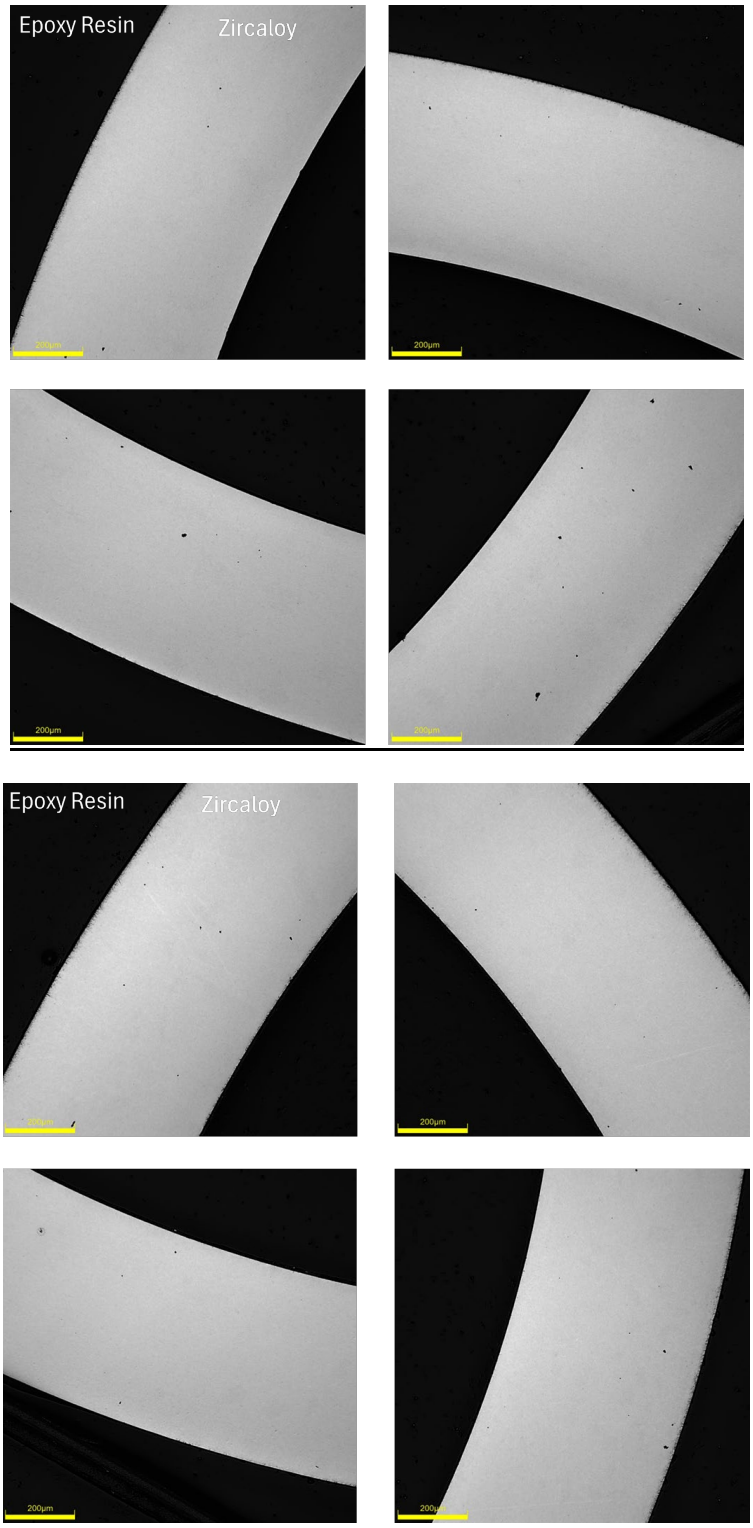

Figure 3.14. Polished OM images of MI-Z-U1-1 S1 (top) and MI-Z-U1-1 S2 (bottom) showing portions of quadrants A, B, C, and D (clockwise from the top right).

3.2.2.3 Out-of-Core Cold Spray Cr-coated Coated Materials

Specimens from MO-Z-C1-1 (parent) were N_2 CS Cr-Coated cladding with a coating thickness noted to range from 15-25 µm. The parent sample was situated in the out-of-core testing loop, and as such was subjected to the same water chemistry and temperature as in-core samples, but in the absence of radiation. Two specimens, each nominally 3 mm in cladding length, were prepared from the parent sample (-S1 and -S2) to compare results.

Figure 3.15. Out-of-core N_2 cold spray Cr-coated sample MO-Z-C1.

Visually, the out-of-core CS Cr-coated sample exhibited a dark blue/purple hue across the length of the sample, Figure 3.15. This color discrepancy is notable as it differs from the other out-of-core samples, which typically exhibit a gold or silver hue. The color differences are characteristic of thin-film optical interference, where thickness variations of only tens of nanometers can produce visibly distinct hues.

Optical microscopy was performed on both polished, Figure 3.16 and Figure 3.17, and etched samples, Figure 3.18. For further analysis, the substrate thickness and the Cr-coating thickness were also measured on polished samples. Multiple measurements of the thickness of the coating and substrate were captured, and the values were averaged to obtain an average substrate thickness measurement and Cr-coating thickness measurement. Post OM, etching was performed on specimen MO-Z-C1-1 S1 to give detailed imaging of the hydrides in the sample.

The substrate thickness of the samples remained quite consistent in measurements with little variability, Table 3.2. The coating thickness showed a slight range as observed in Figure 3.16, and documented in Table 3.3, which is consistent with the cold spray application process.

Table 3.2.Substrate thickness of cold spray Cr-coated out-of-core Optimized ZIRLO™.

Sample	Quadrant	Substrate Thickness µm	Average Substrate Thickness µm
MO-Z-C1-1 S1	A	567, 566, 565	566 ± 1
	C	566, 566, 568	566 ± 1

Table 3.3. Coating thickness of cold spray Cr-coated out-of-core Optimized ZIRLO™.

Sample	Quadrant	Cr-coating Thickness, µm	Average Cr-coating Thickness, µm
MO-Z-C1-1 S1	A	20, 14, 17	17 ± 3
	C	16, 15, 14	15 ± 1

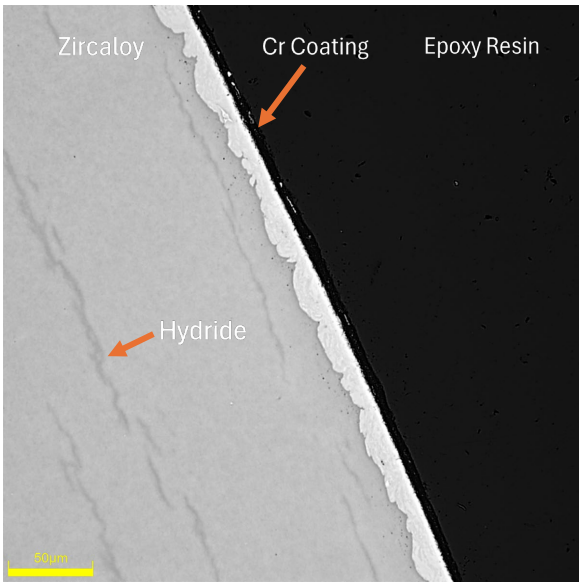

Figure 3.16. Polished image of the Cr Coated MO-Z-C1-1 S1 cladding showing the Cr-coating/substrate interface, with hydrides in the substrate.

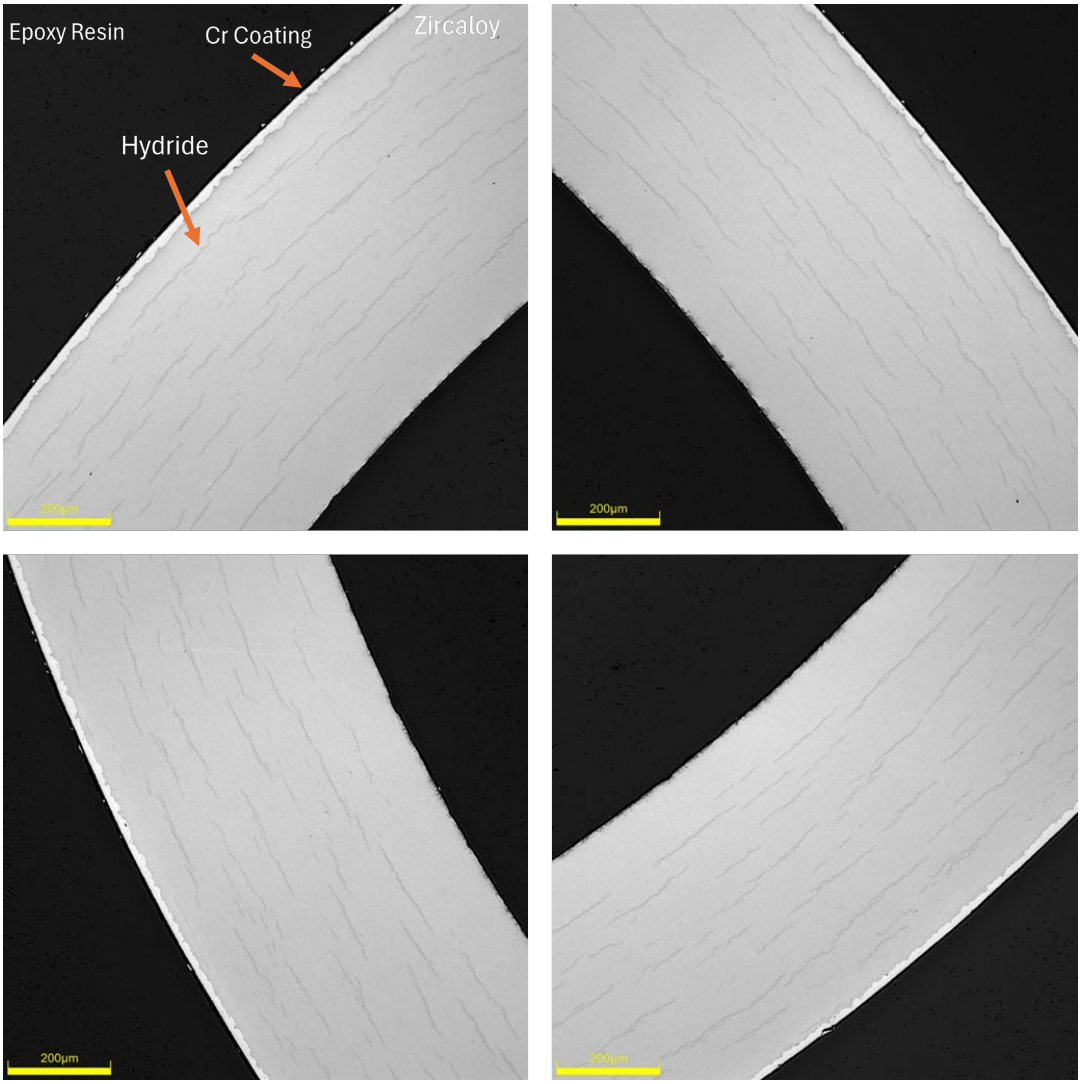

Figure 3.17. Polished OM images of MO-Z-C1-1 S1 showing portions of quadrants A, B, C, and D (clockwise from the top right) for hydride visualization.

Hydrides were immediately observed in the out-of-core Cr-coated sample. To further analyze these chemical etching techniques per Section 3.1.4 were performed on MO-Z-C1-1 S1 to better observe the hydrides within the zircaloy substrate. However, the etching process masked the hydrides in comparison to the polished specimens. Chemical etching was not pursued further for hydride analysis and polished images were instead used for the second specimen.

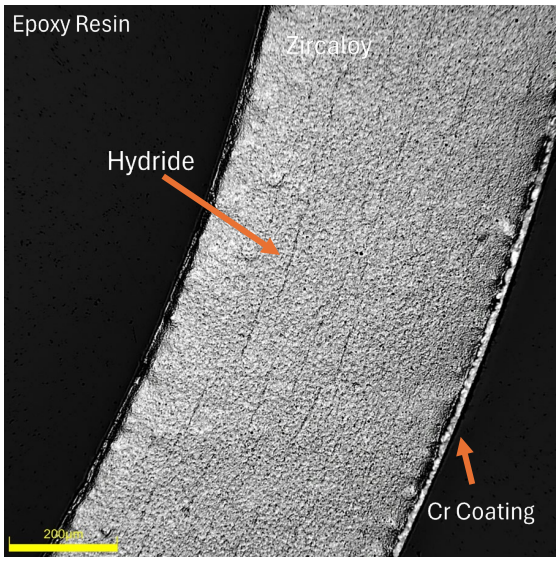

Figure 3.18. Chemically etched OM image of MO-Z-C1-1 S1, showing hydrides in the cladding substrate.

Sample S2 from the out-of-core CS Cr-coated sample was prepared in the same manner as S1 for comparison analysis. The results from S2 agree with S1, showing hydrides well into the zircaloy substrate region of the cladding. As observed in Figure 3.19 and Figure 3.20, the hydrides are distributed through the substrate. However, as observed in S1 (Figure 3.17), it is visually seen that the hydrides are located close to the outer diameter and Cr-coating of the sample, but are notably not as closely located at the inner diameter.

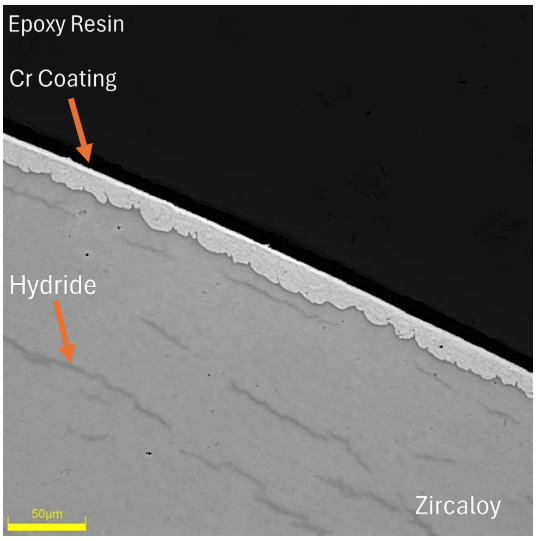

Figure 3.19. Polished image of the MO-Z-C1-1 S2 cladding showing the Cr-coating/substrate interface, with hydrides in the substrate.

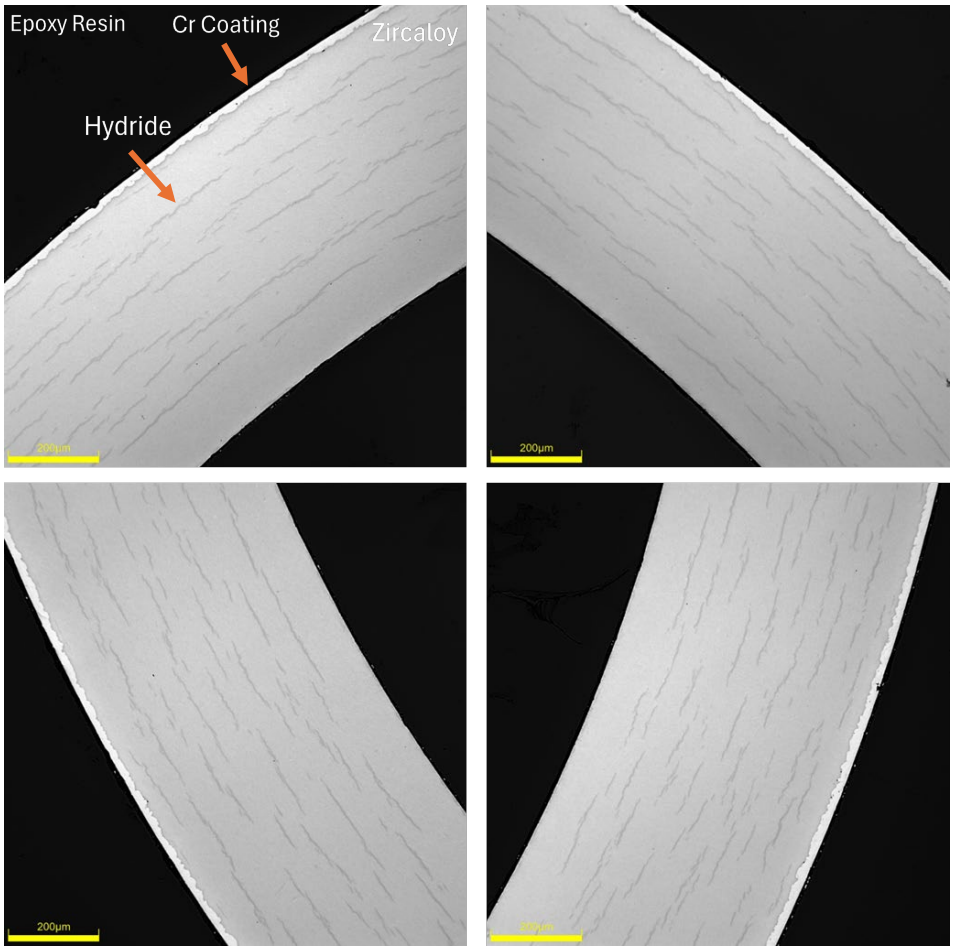

Figure 3.20. Polished OM images of MO-Z-C1-1 S2 showing portions of quadrants A, B, C, and D (clockwise from the top right) for hydride visualization.

Both samples MO-Z-C1-1 S1 and MO-Z-C1-1 S2 showed hydrides and their orientation distributed throughout the cladding zircaloy substrate. The hydrides were distributed closer in proximity to the outer diameter and Cr-coating, whereas a notable gap was observed in the proximity of the hydrides to the inner diameter of the cladding. Oxide layers on the outer and inner diameter were not observed using OM techniques.

The out-of-core Cr-coated material was tested for total hydrogen concentration as a bulk measurement using the LECO analyzer. Two specimens were tested for content from MO-Z-C1, generating a weighted average measurement of 101±3 wppm. This hydrogen content is greatly increased from the value observed in the uncoated out-of-core material, which was 12 wppm.

SEM analysis of the MO-Z-C1-1 S2 also showed the occurrence of the hydrides in the material. The Cr-coating was also examined in closer detail. One issue with SEM-EDS analysis is resolving the severe overlap of the Cr-L and O-K x-ray lines. With the irradiated specimens, a more advanced EDS system was used which was not available for the non-irradiated specimens that were reported earlier in this report. The Oxford Aztec software does account for the overlap between these elements by modeling the K- and L- lines from Cr. The results showed consistently the occurrence of a thin oxide layer on the outermost surface of the Cr-coating. Figure 3.21 shows SEM images of the MO-Z-C1-1-S2 material revealing the complex nature of the Cr-coating and at lower magnification, the hydrides. It was not possible to reveal

the coating and the hydrides clearly in the same image. In Figure 3.22 high resolution SEM images of the coating and elemental maps are shown. The oxide layer is apparent on the outermost surface of the Cr-coating.

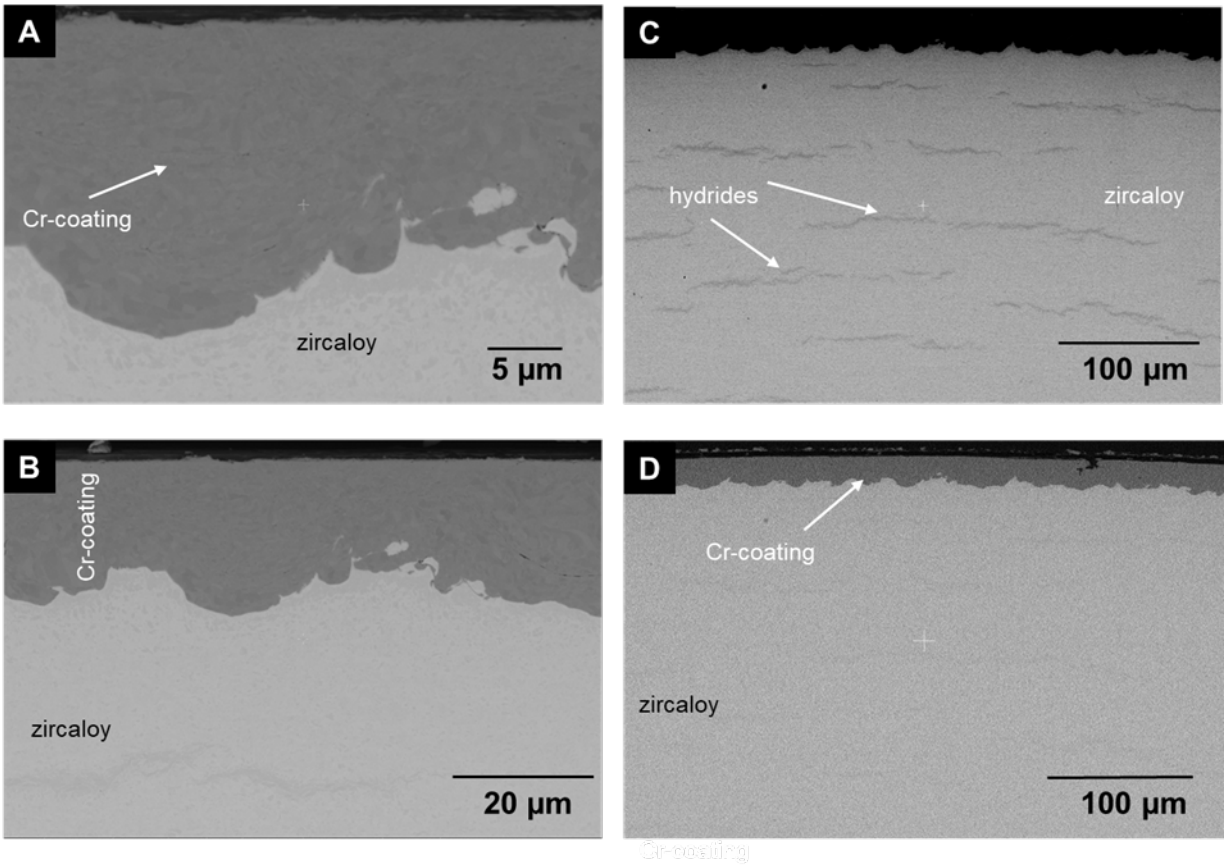

Figure 3.21. SEM images of MO-Z-C1-1 S2 showing different regions of the sample. (A and B) high magnification images of the Cr-layer, (C, and D) showing low magnification SEM images with different contrast levels to show the coating and the hydrides.

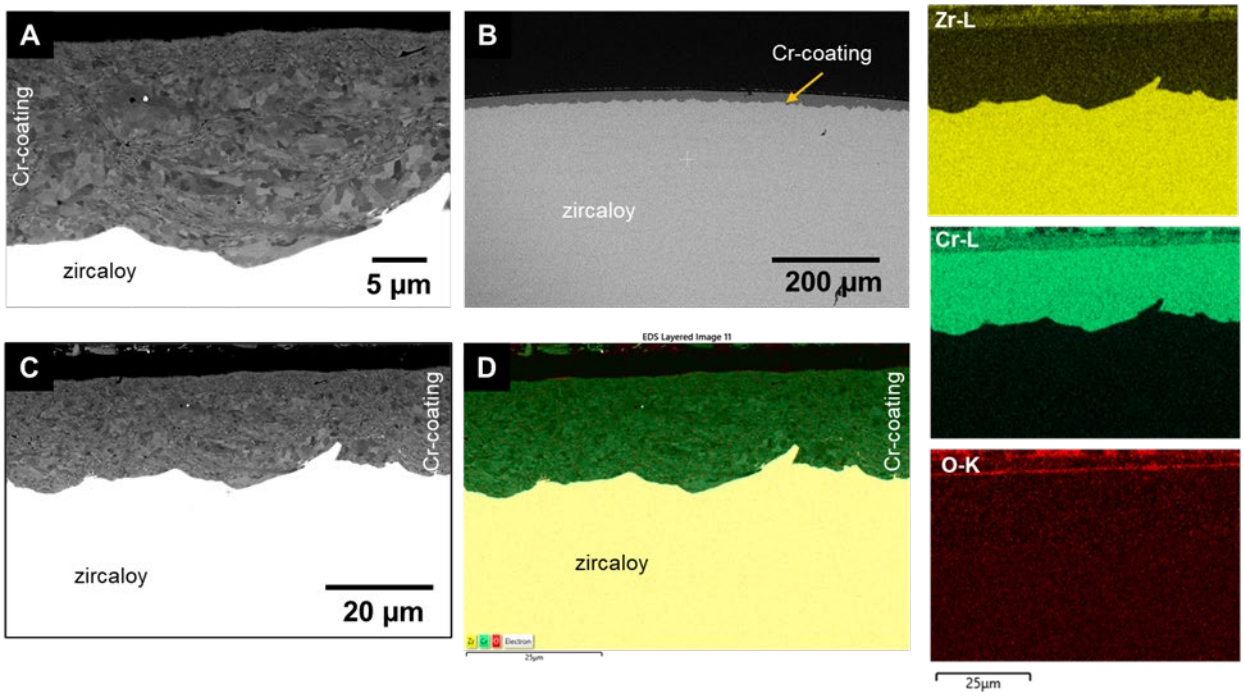

Figure 3.22. SEM high resolution images of the coating and elemental maps of the Cr-coating. The elemental maps show that the outer portion of the Cr-coating does possess an oxide layer.

The Cr-coated out-of-core samples were further analyzed using TEM and SEM techniques for characterization. For TEM preparation, two lift outs were completed, and the general lift out areas are shown in Figure 3.23 in red.

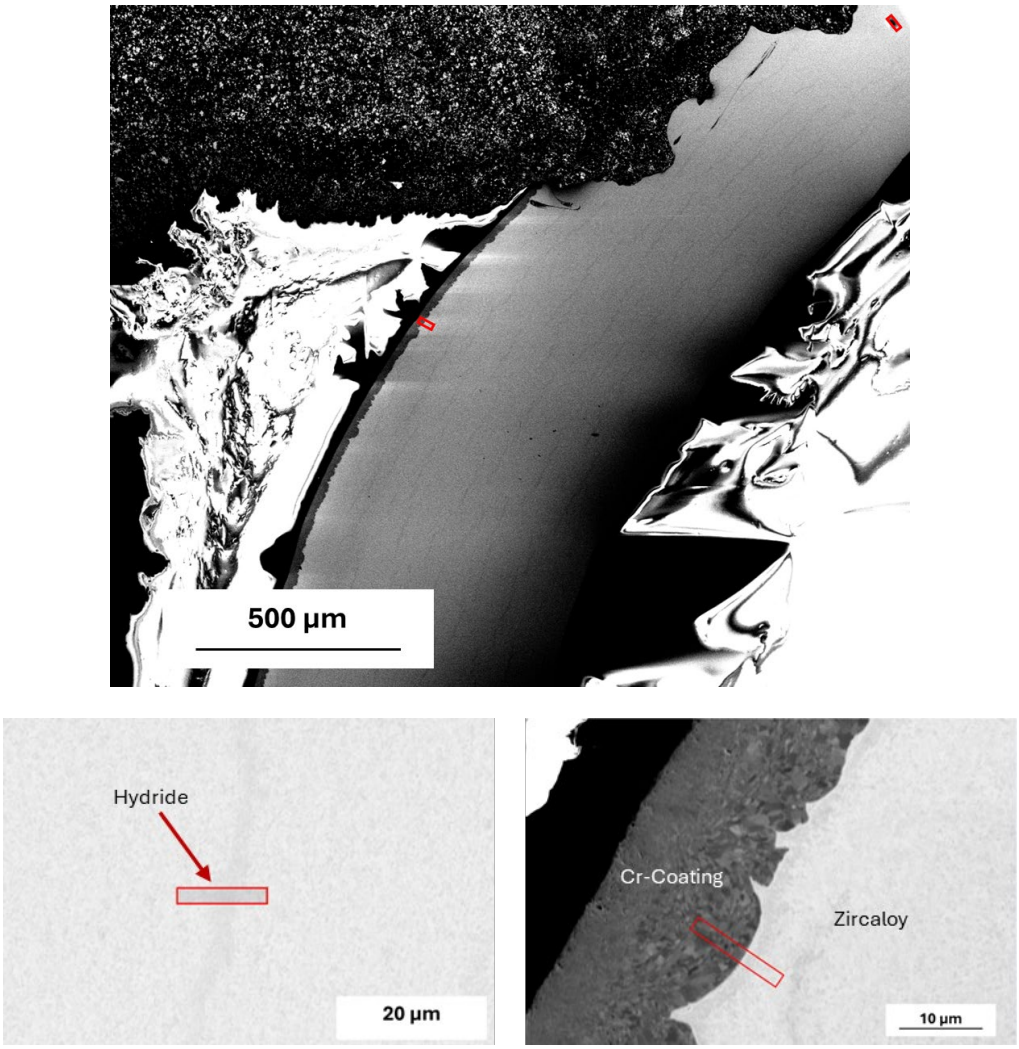

Figure 3.23. (Top) General areas (red) for three lift outs completed on MO-Z-C1-1 S1. (Bottom) Specified lift out areas.

The lift outs were focused on two areas to provide material for TEM analysis, specifically across a hydride in the zircaloy substrate, and across the Cr-coating/substrate interface (see Figure 3.24). Efforts were made to reduce the formation of hydrides during ion irradiation using cryo-conditions. This also necessitated the use of the Mo-grid instead of the more common Cu-grids. Nevertheless, ion irradiation during sample preparation did cause some damage to the specimens (see Figure 3.25 and Figure 3.26).

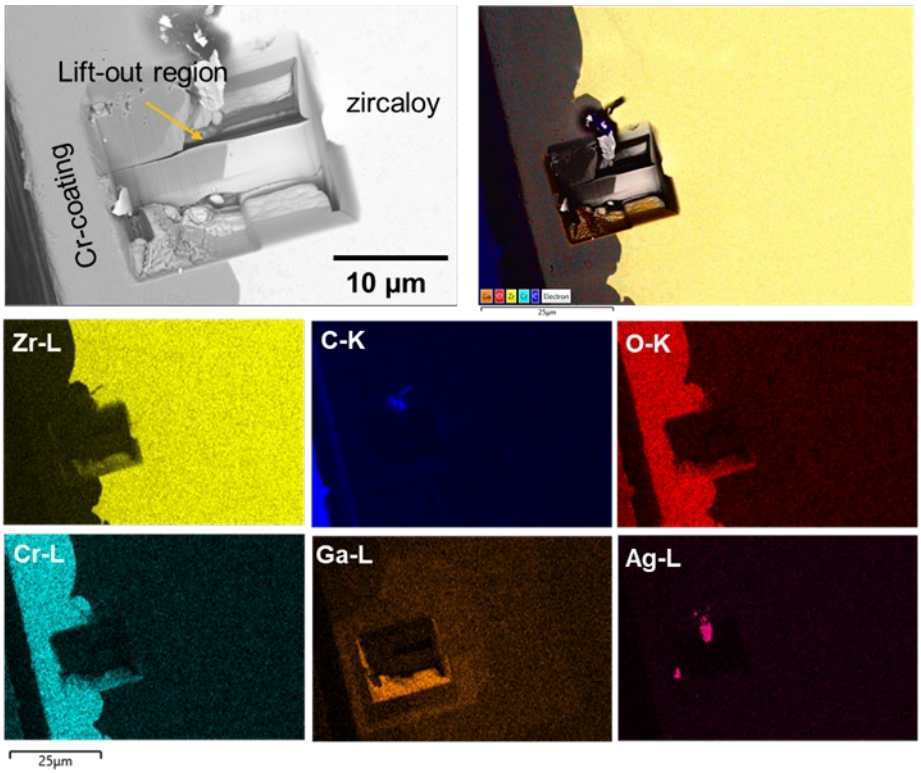

Figure 3.24. SEM analysis of the region from the TEM lift-outs, showing the Cr-Zr interface area. Ga and Ag were contaminants from the ion gun and the conductive coating, respectively.

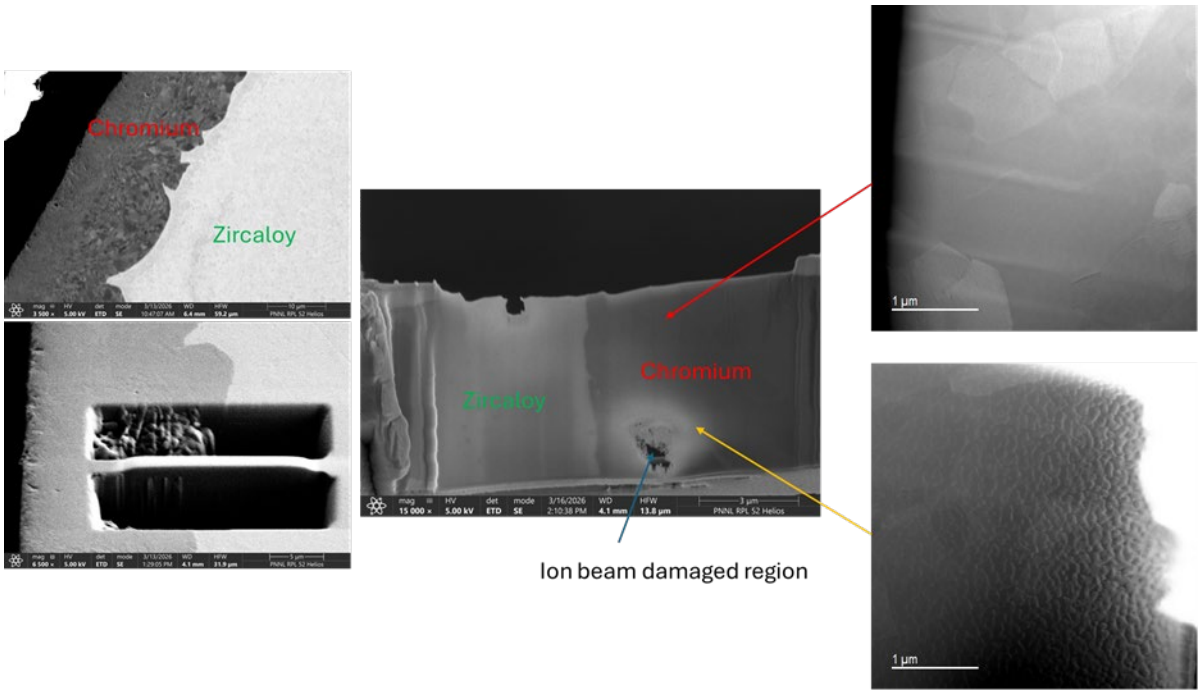

Figure 3.25. SEM image and selected region for the lift-out at the Cr-Zircaloy interface from MO-Z-C1-1 S1. The STEM images indicated severe beam damage from the Ga-ion beam on the region closest to the Pt-protective coating.

Higher magnification TEM images from the lift out are shown in Figure 3.26 where two regions are visible. One was undamaged but the other had significant beam damage that prevented further analysis. However, the Cr-Zr interface was still intact on one side. SAED was obtained from the Zr and Cr regions and compared to standard structures (see Figure 3.27). The polycrystalline regions of the Zircaloy provided a ring pattern that was analyzed with CrysTBox software and the Cr-region provided some single crystal patterns. The matches were not perfect but were sufficient to confirm that the Cr phase was BCC and the Zr phase was hexagonal close-packed (HCP). Table 3.4 shows the results from the SAED from the zirconium phase and matches well with α-Zr, as expected.

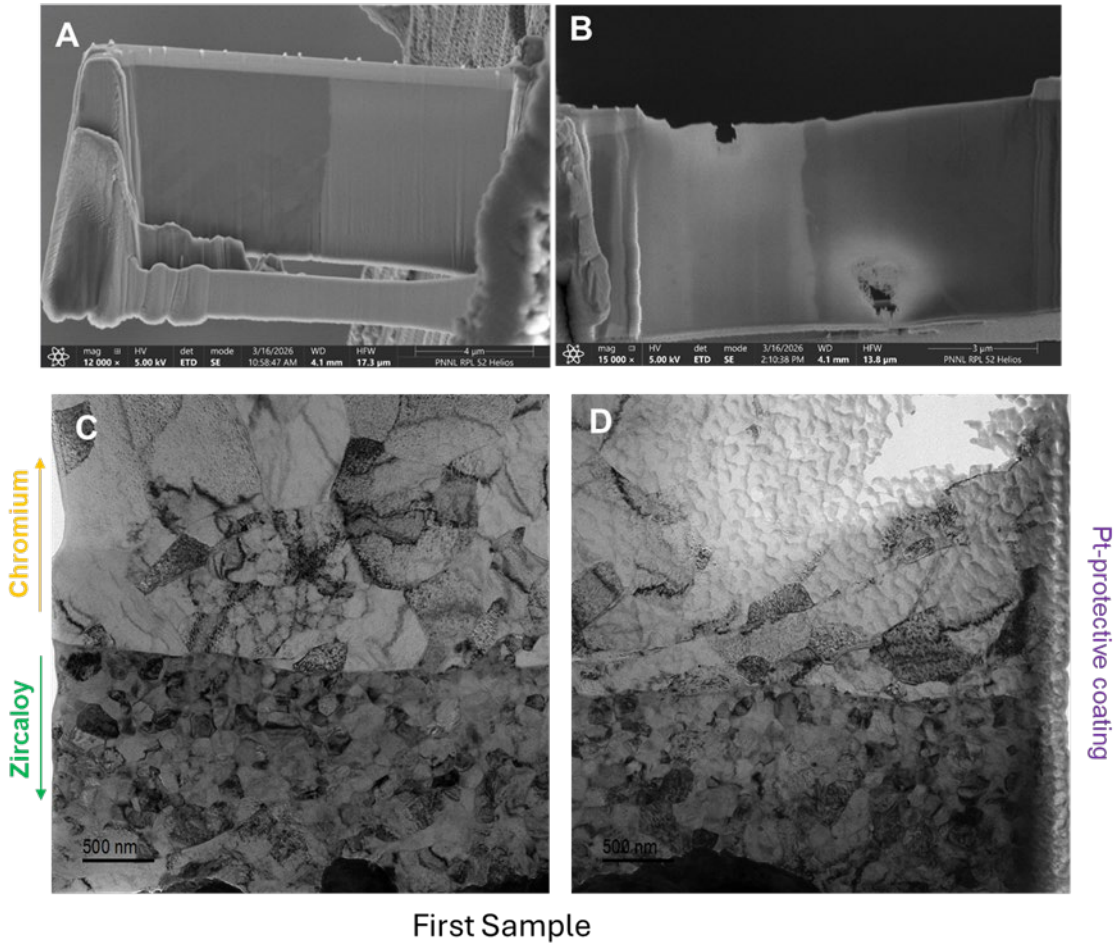

Figure 3.26. SEM images of the MO-Z-C1-1 S1 lift-out region (A) low magnification image of interfacial region prior to thinning and (B) SEM showing the damaged region, TEM images (C) and (D) showing a good quality interface on one side and a damaged interfaces on the other.

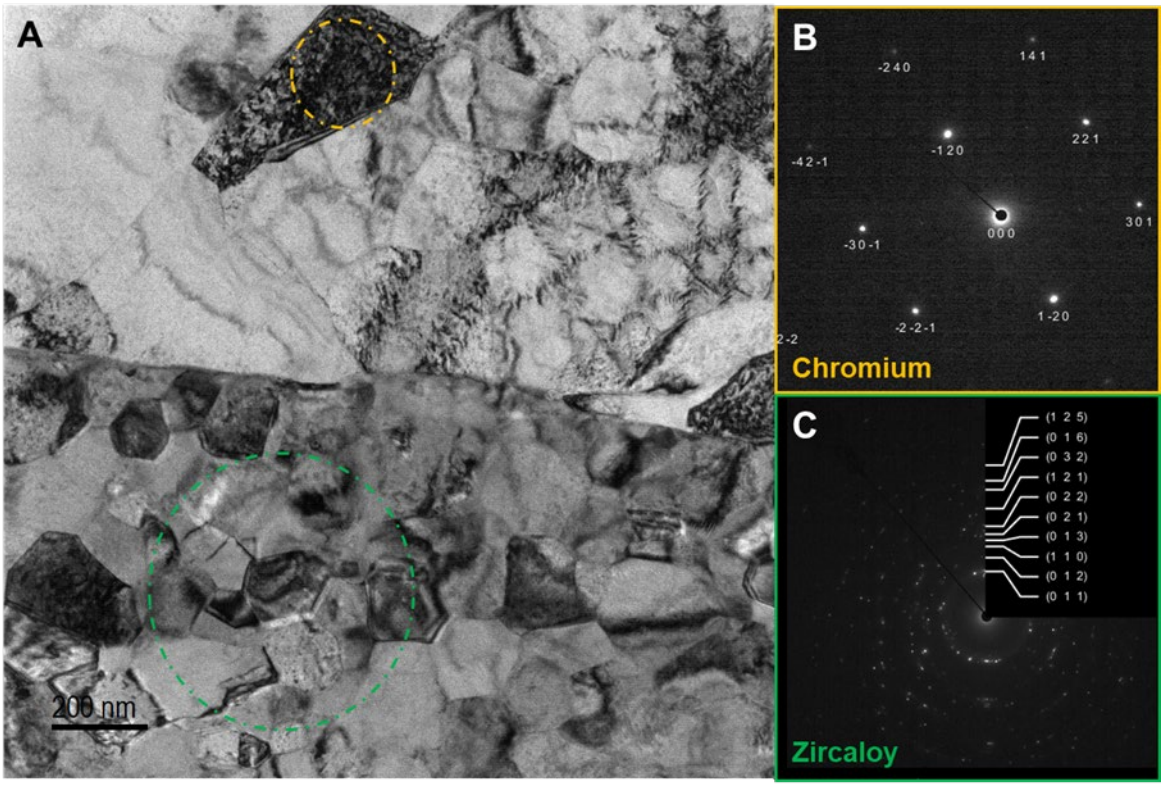

Figure 3.27. A) TEM image of the interface and electron diffraction obtained from the Zircaloy and Cr regions and (B and C) for diffraction pattern analysis with a reasonable match to Cr metal and α-Zr.

Table 3.4. Electron diffraction results from the Zircaloy from MO-Z-C1-1 S1 compared to HCP α-Zr.

	d-spacing [nm]	
Plane	theor.	measured
(0 1 1)	0.246	0.247
(0 1 2)	0.189	0.190
(1 1 0)	0.162	0.159
(0 1 3)	0.146	0.147
(0 2 1)	0.135	0.136
(0 2 2)	0.123	0.124
(1 2 1)	0.104	0.103
(0 3 2)	0.088	0.088
(0 1 6)	0.082	0.082
(1 2 5)	0.074	0.074

To better image and understand the grain structure analysis, 4D STEM was utilized as an advanced imaging technique. In Figure 3.28, the 4D STEM analysis was obtained over the Cr-Zr interface. The region contained the ion beam damaged region however, the result in (D) is an effective orientation map.

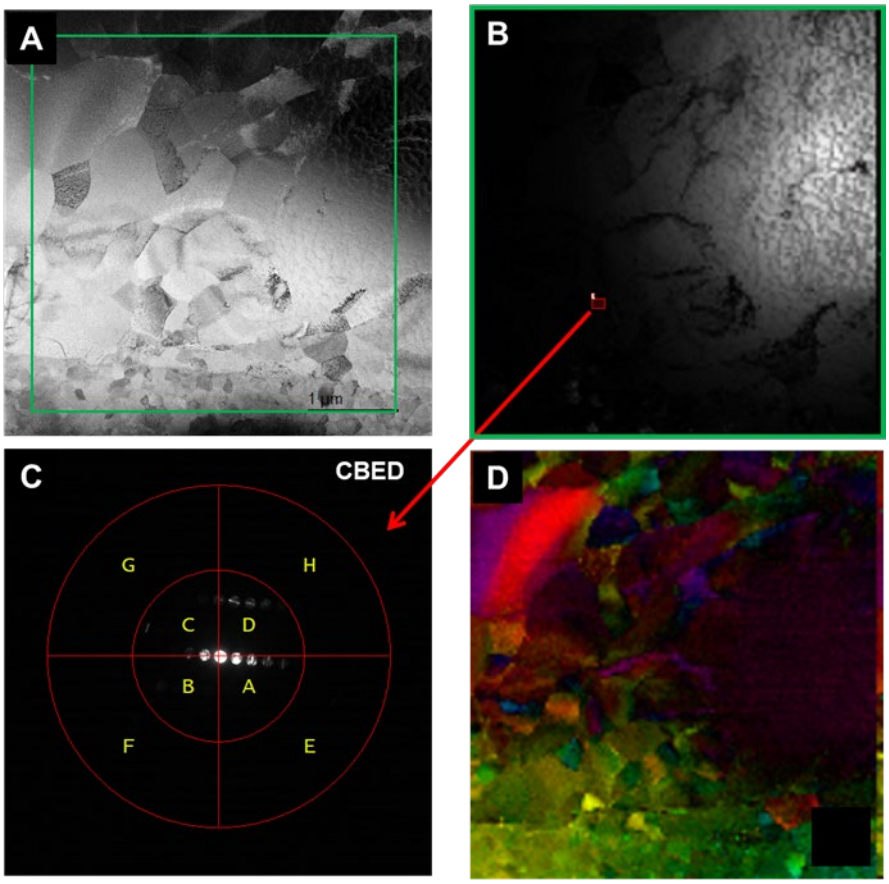

Figure 3.28. 4D-STEM analysis of the interface from MO-Z-C1-1 S1 in the ion-beam damaged region. (A) medium magnification STEM image of the region, (B) 4D-STEM output, (C) electron diffraction pattern from the marked point, (D) 4D-STEM analysis showing grains but indicated some amorphization in the damaged region.

The Cr-coating and zircaloy substrate interface were analyzed using STEM-EELS for elemental identification, Figure 3.29. The resulting STEM-EELS analysis indicated the presence of oxygen enriched at the surface of the sample.

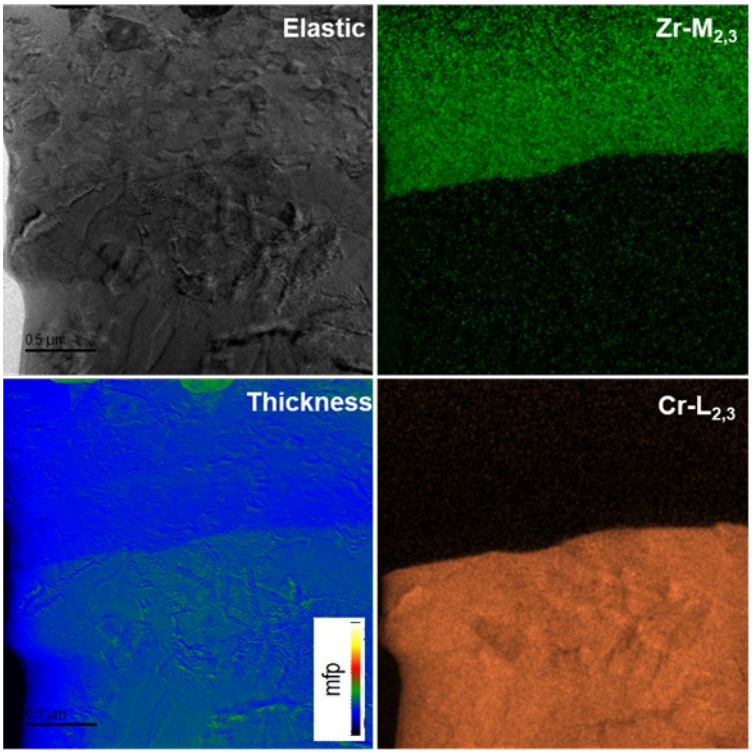

Figure 3.29. EFTEM analysis of the Cr-coating and zircaloy substrate interface of MO-Z-C1-1 S1 showing the elastic (zero-loss image), and images using the Zr, and Cr edges, and the thickness map demonstrating uniform thickness.

STEM-EELS analysis showed that there was no evidence of oxygen in the Cr-layer present in the TEM lift-out. It will be shown later that the oxygen was detected on the outermost surface. A thin oxygen layer was observed on the lift-out but this was an artifact that was formed after the lift-out was made. The layer was <10 nm thick and was on the thinnest region of the section. EELS analysis confirmed the occurrence of the O-K edge in this area. During the SEM analysis, by running the microscope at 10 keV, both the Cr-K and L-lines were excited. This enabled the Aztec software to separate out the O-K and Cr-L signals.

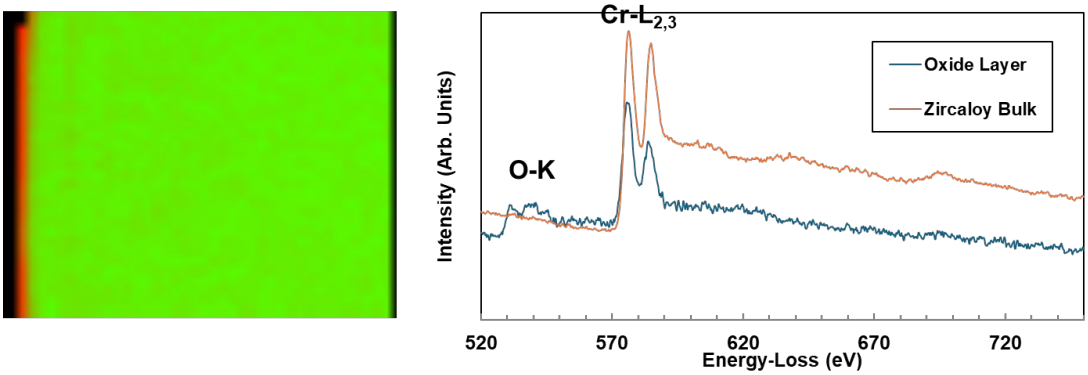

Figure 3.30. There was evidence of an oxide layer in MO-Z-C1-1 on one side of the lift-out in the bulk chromium region from the TEM lift-out with EELS.

The second TEM lamella specimen (see Figure 3.31) was captured through a hydride in the zircaloy substrate. With normal STEM and TEM imaging the hydride was not clearly visible. STEM-EDS maps shown in Figure 3.32 do not indicate the hydride however Nb-Fe precipitates were visible.

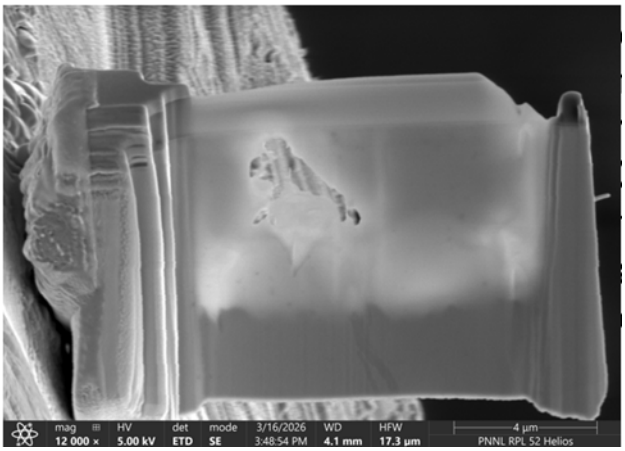

Figure 3.31. TEM image of the lamella containing the zircaloy substrate which was known to contain hydrides.

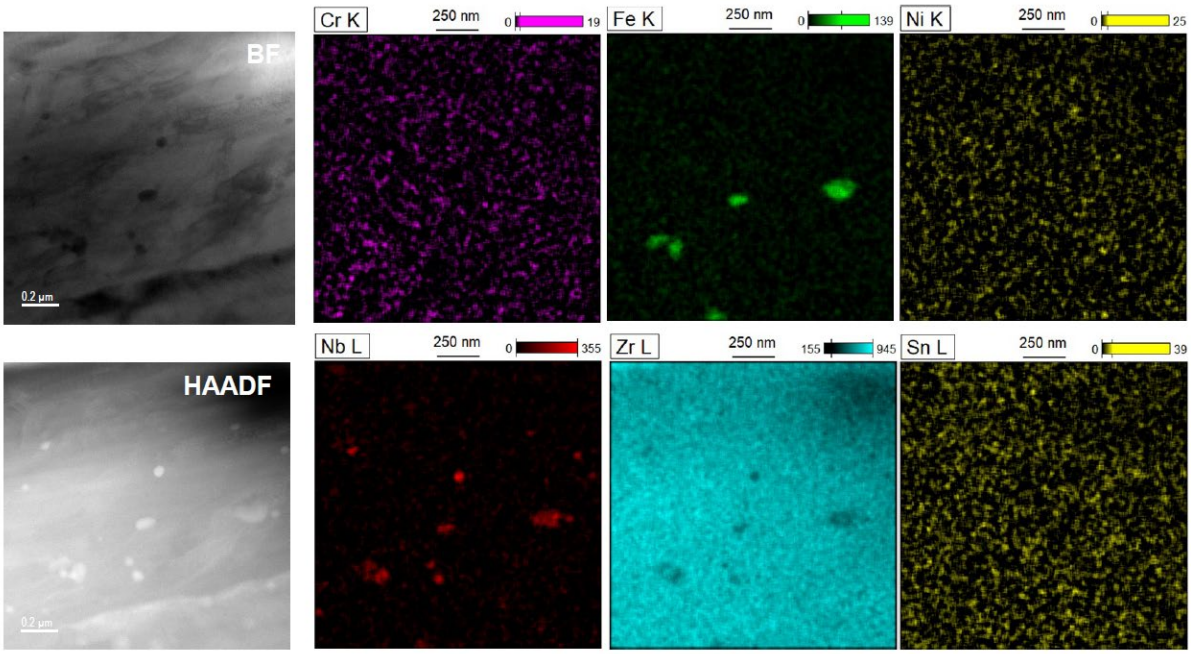

Figure 3.32. STEM-EDS show the occurrence of a mixed Fe-Nb phase in the Zircaloy. Hydrides could not be identified in the TEM/STEM analysis.

Results from the STEM-EDS shows that the zircaloy substrate contained particles of a mixed Niobium-Iron (Nb-Fe) intermetallic. 4D-STEM is an analysis technique that can provide information similar to EBSD where each point in the image is defined by a 2D electron diffraction pattern. Figure 3.33 shows three panels; (A) the bright field STEM image, (B) convergent beam pattern from the point marked by the red- box in (A), and (C) the computed 4D grain orientation map. The 4D image was constructed by dividing the CBED image into

segments, and then analyzing the individual images extracted from the resultant images. The image in (C) shows three distinct diagonal lines (indicated by the arrows), which are regions with the same grain orientation. These are most likely hydrides in the zircaloy that were not visible otherwise.

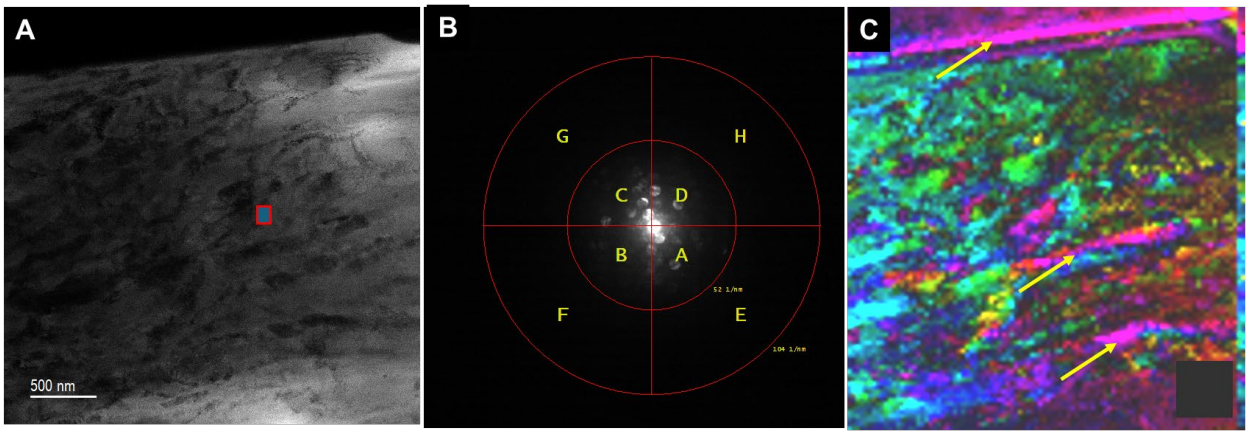

Figure 3.33. 4D-STEM of the second (Zircaloy-only specimen) of MO-Z-C1-1 S1. (A) medium magnification STEM image, (B) electron diffraction pattern, and (C) 4D-STEM result showing elongated structures that are possibly hydrides.

3.2.2.4 In-Core Cold Spray Cr-coated Coated Materials

The in-core Cs Cr-coated cladding sample appeared bright gold in hue across the majority of the length of the sample, Figure 3.34. The coloration differed from that of the out-of-core comparable sample.

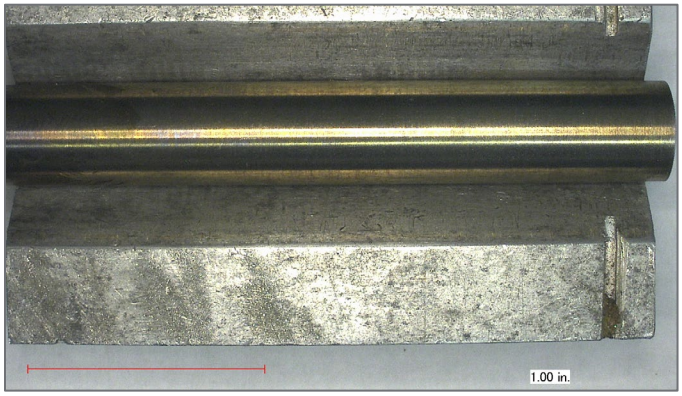

Figure 3.34. In-core N_2 cold spray Cr-coated sample MI-Z-C1.

Samples were prepared for polishing in the same manner as described in Section 3.0. Optical microscopy was completed on polished samples to show the hydride content within the substrate, Figure 3.35. Measurements of the Cr-coating and the substrate thickness were made, with the values averaged to obtain the Cr-coating thickness measurement.

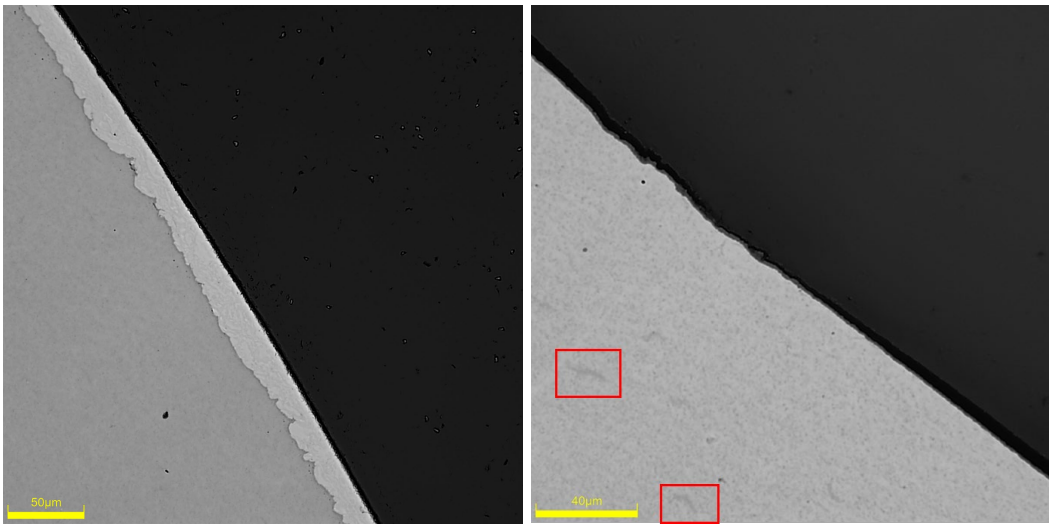

Figure 3.35. Polished image of the MI-Z-C1-1 S1 cladding showing the Cr-coating/substrate interface (left), and the inner diameter (right). Small, short hydrides (red boxes) observed in the in-core CS Cr-coated variant at higher magnification

Like the out-of-core sample, the substrate thickness of the samples remained consistent with little variability in the measured values, Table 3.5. The Cr-coating thickness showed similar variability to that observed in the out-of-core sample, but with a thicker Cr-coating layer on average, Table 3.6. The variability was expected due to the cold spray process, and the coating thickness is in adherence to the range noted by Westinghouse. Higher magnification, however, did reveal the presence of small, short hydrides within the substrate, Figure 3.35.

Table 3.5. Substrate thickness of cold spray Cr-coated in-core Optimized ZIRLO™.

Sample	Quadrant	Substrate Thickness μm	Average Substrate Thickness μm
MI-Z-C1-1 S1	A	561, 557, 558	559 ± 2
	C	559, 561, 563	561 ± 2

Table 3.6. Coating thickness of cold spray Cr-coated in-core Optimized ZIRLO™.

Sample	Quadrant	Cr-coating Thickness, μm	Average Cr-coating Thickness, μm
MI-Z-C1-1 S1	A	22, 23, 19	21 ± 2
	C	18, 20, 19	19 ± 1

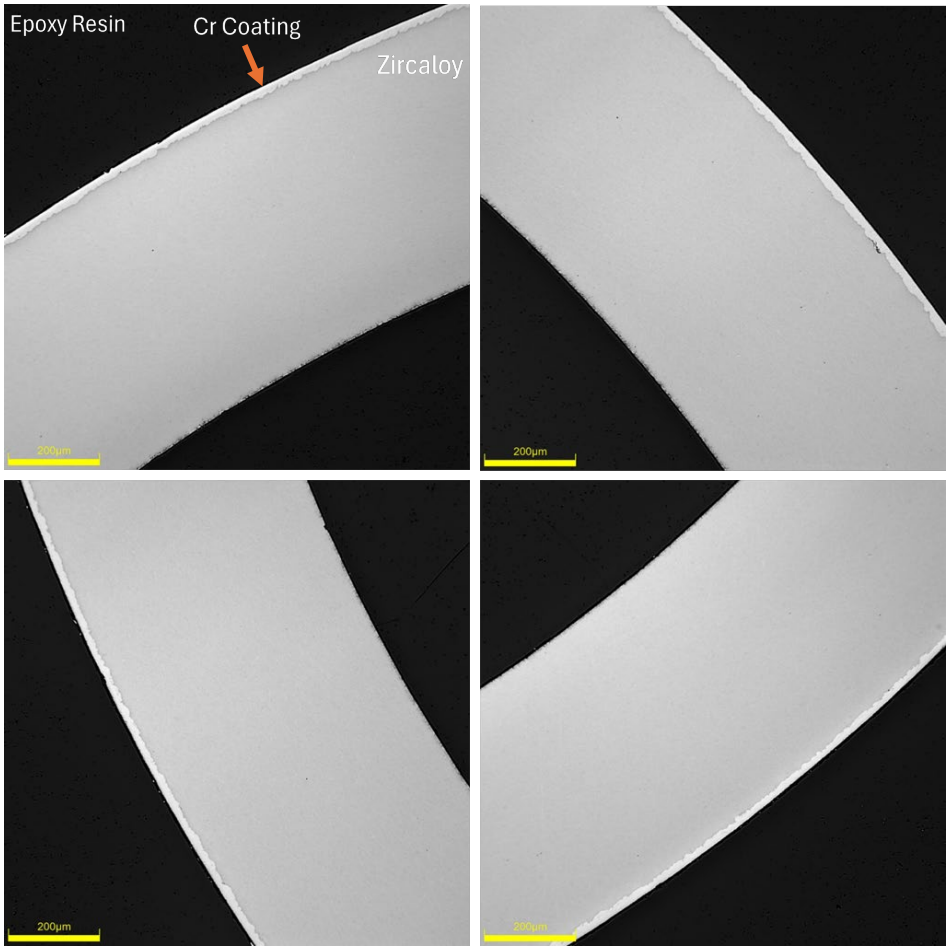

Figure 3.36. Polished OM images of MI-Z-C1-1 S1 showing portions of quadrants A, B, C, and D (clockwise from the top right) with no visible hydrides.

The polished cladding exhibited a smooth surface with no notable defects in the substrate itself. Some areas of the Cr-coating appear to have porosity (Figure 3.36, quadrant A), but there were no other notable features.

Post OM analysis the sample was taken one step further to chemical etching, as directed in Section 3.1.4, to further understand hydride content if observable. Figure 3.37 illustrates the results of the chemical etch process, which did not reveal hydrides in the sample. Rather, a dimpling effect became pronounced on the sample, for unknown reasons. As the chemical etching process generated concerns on the prior out-of-core sample tested as well, it was decided to no longer pursue chemical etching as a visual method for hydrides.

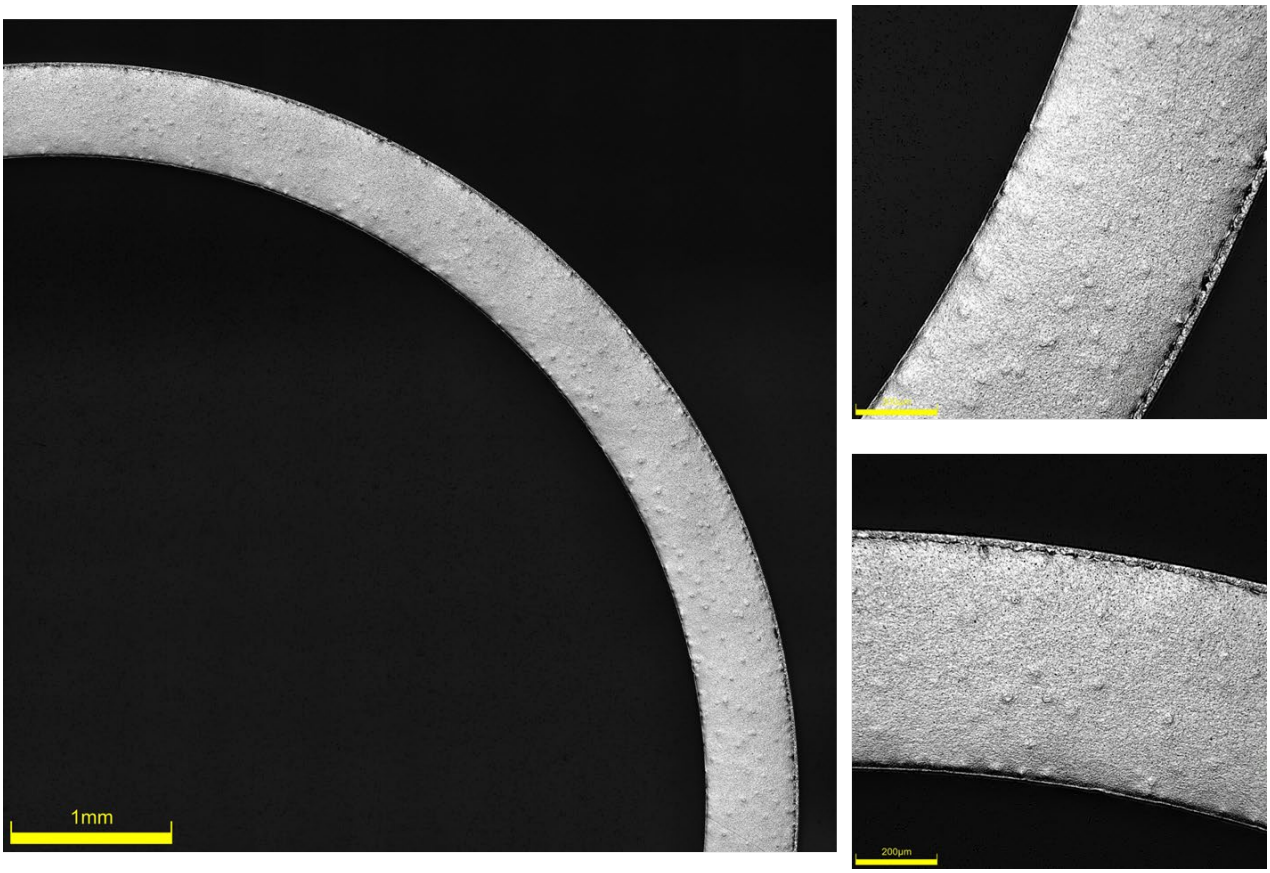

Figure 3.37. Chemically etched OM image of MI-Z-C1-1 S1, showing a dimpling effect generated from the etchant.

A second in-core sample, S2, was prepared to compare to S1. The S2 sample was not subjected to the chemical etching process due to the lack of information provided from the results and the poor state of the sample. In S2, the substrate and Cr-coating matched S1, as expected, Figure 3.38.

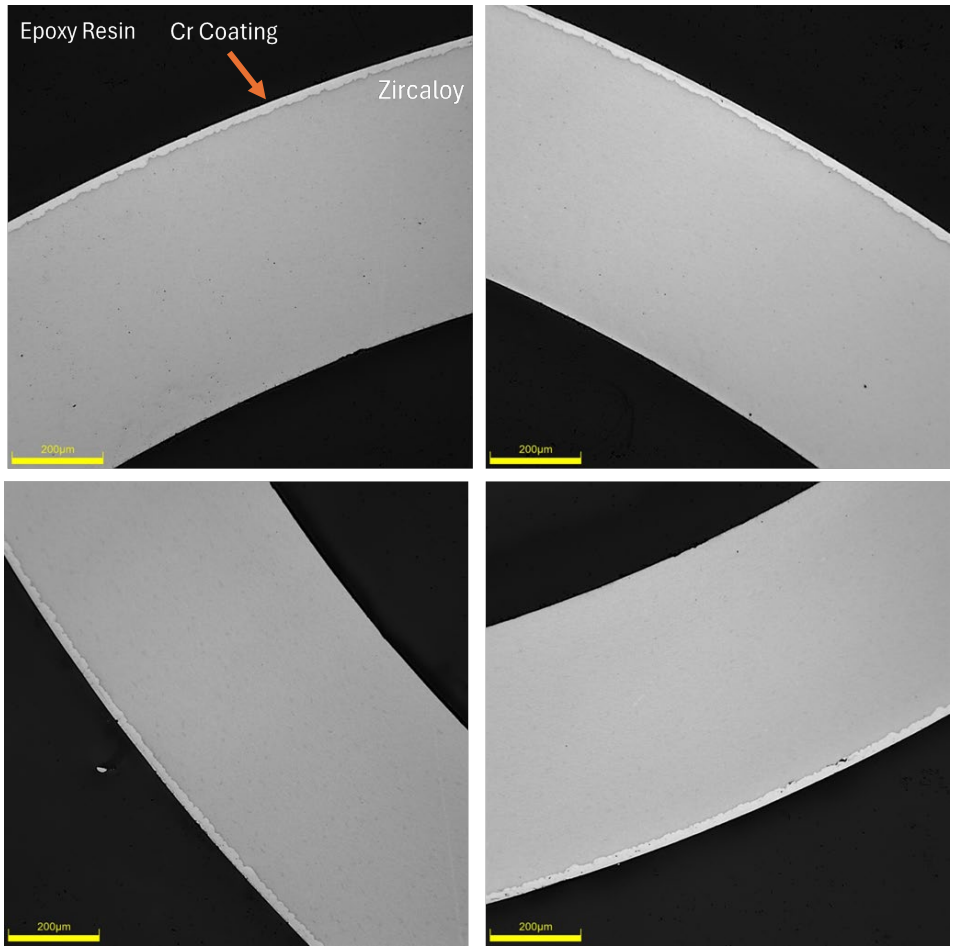

Figure 3.38. Polished OM images of MI-Z-C1-1 S2 showing portions of quadrants A, B, C, and D (clockwise from the top right) with no visible hydrides.

To aid in the understanding of hydride generation, and the impact of the oxide layer on this, images of the inner and outer diameter of the sample were captured to observe if an increased oxide layer was observed on either side. However, no oxide layer was readily observed on either the inner or outer diameter of the cladding ring in this in-core sample with OM.

High resolution SEM images of the Cr-coating are shown in Figure 3.39. There was no evidence of hydrides in agreement with the OM results. Elemental maps from the Cr-coated region are shown in Figure 3.40. There is a suggestion of a thin oxide layer on the outermost surface of the Cr-coating. Interpreting this layer is difficult because it is connected to the epoxy resin used for embedding the sample. Furthermore, there are questions about the ability for the O-K and Cr-L signals to be resolved. On the inner zircaloy side where there was no Cr present, a clear oxide layer was observed, Figure 3.41. The morphology of this layer in the SEM images is consistent with other oxidized Zircaloys observed. The Aztec software was able to correctly demonstrate that Cr was not present in the corrosion rind. This analysis confirms the ability of the Aztec system to separate out the Cr and O signals.

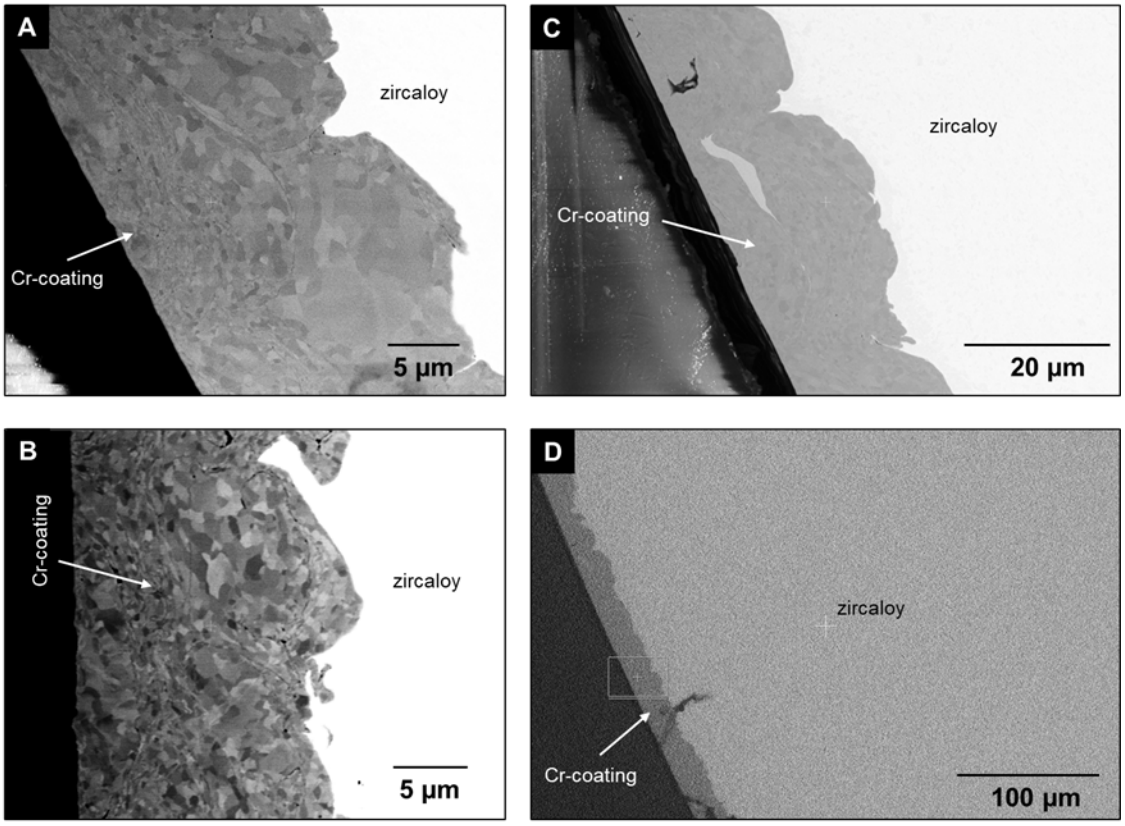

Figure 3.39. SEM high resolution images of the coating in M1-Z-C1-1-S2 showing no evidence of hydrides in the Zircaloy.

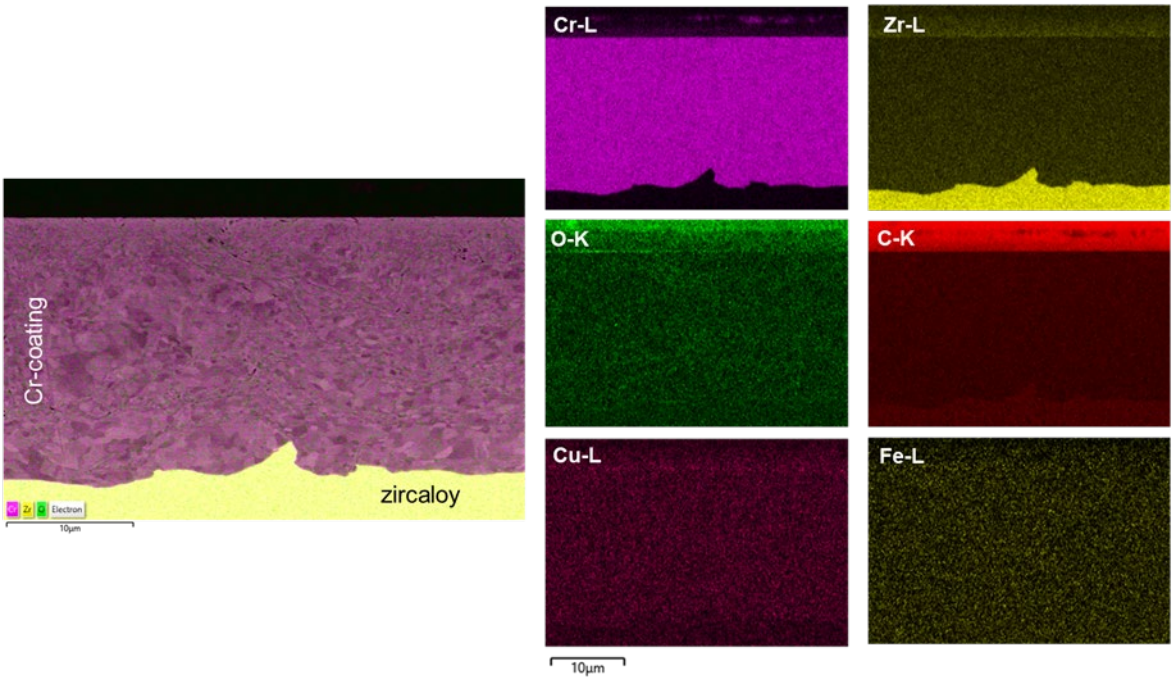

Figure 3.40. SEM-EDS analysis of the Cr-coated layer on the Zircaloy showing evidence of a thin oxide layer on the outer most surface.

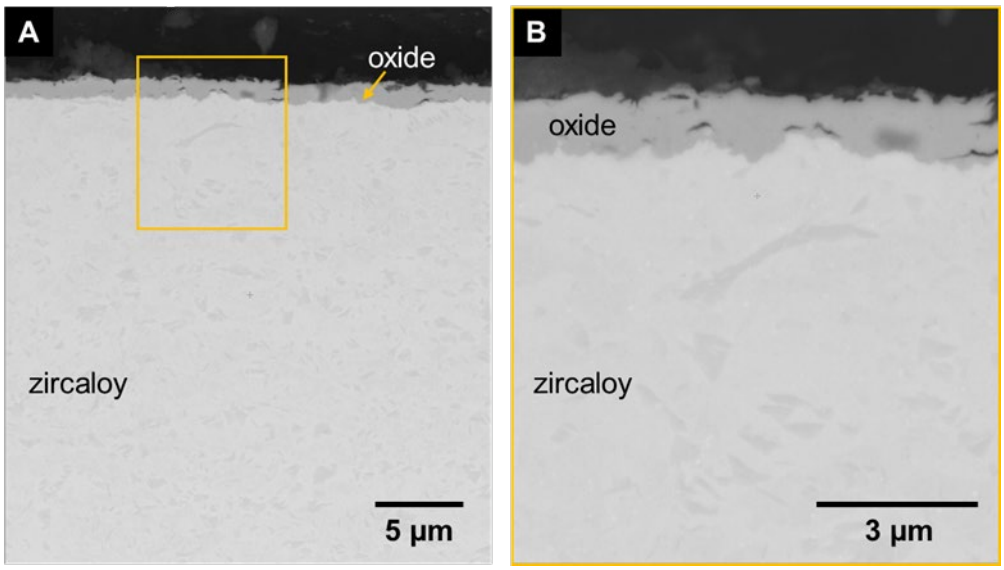

Figure 3.41. Inner diameter of MI-Z-C1-1 S2, showing a notable oxide layer.

SEM-EDS analysis of the inner oxide layer on the zircaloy demonstrated that ability of the Aztec software to separate out Cr and O (see Figure 3.42). In this case, there was no Cr present, even though Cr was included in the analysis to show that the analysis was working correctly.

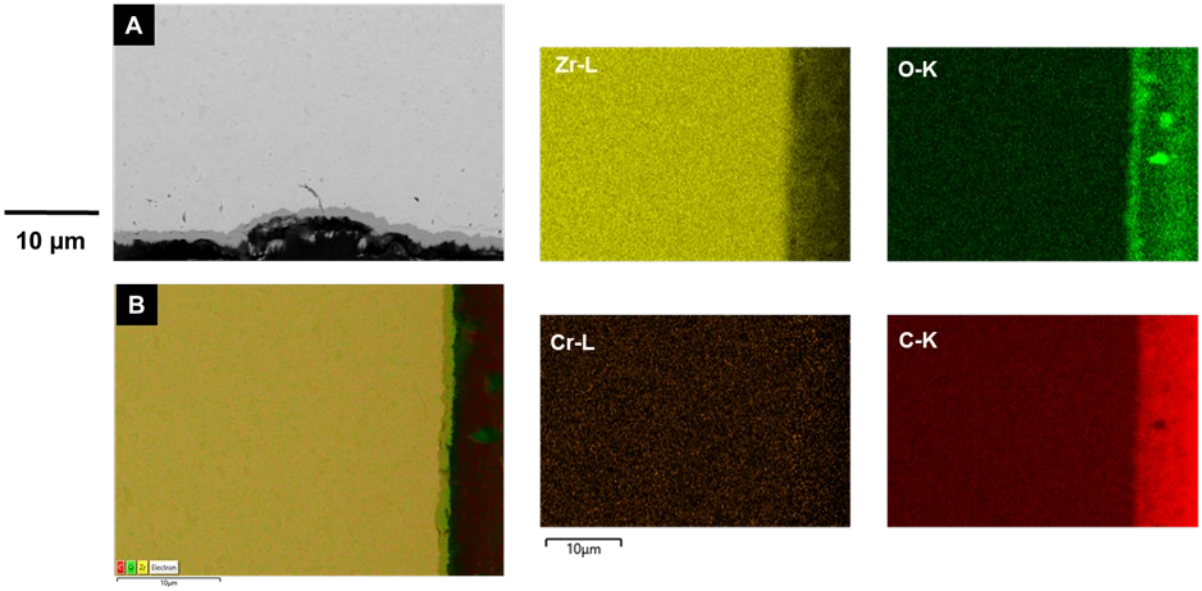

Figure 3.42. SEM-EDS of the oxide layer confirming the occurrence of an oxide corrosion layer. The EDS analysis was able to deconvolute the Cr-L signal from the O-K.

The in-core Cr-coated material was tested for total hydrogen concentration as a bulk measurement using the LECO analyzer for hydrogen content. Two specimens were tested for content from MI-Z-C1, generating a weighted average measurement of 19±1 wppm. This hydrogen content is greatly decreased from the value observed in the equivalent out-of-core material, which was 101 wppm. The value observed for the in-core Cr-coated sample closely reflected the hydrogen content to that of the uncoated in-core cladding, which was 20 wppm hydrogen.

3.2.2.5 In-Core Cold Spray Cr-coated Coated Laser Sample

The laser welded sample was irradiated in core. The CS Cr-coated segments were laser welded together with an uncoated portion in the center of the sample. The sample exhibited a slight gold hue on one side, but mostly appeared a metallic silver color overall, Figure 3.43. The coating on the Cr-coated sides was slated to be 15 to 25 µm in thickness.

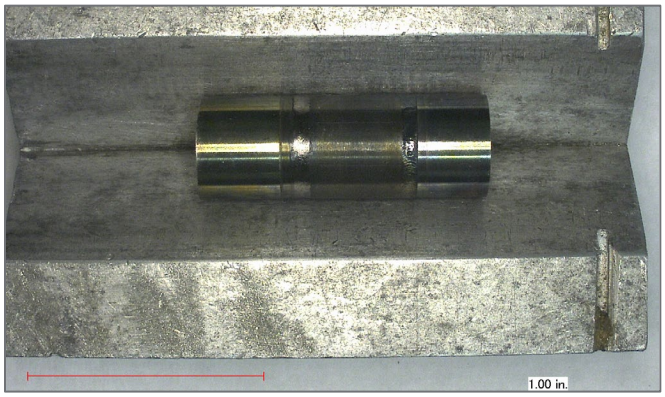

Figure 3.43. In-core N_2 cold spray Cr-coated sample MI-Z-L1.

The laser sample was cut into four quadrants at Westinghouse and distributed to the respective labs, which each lab receiving two quarters of the material. PNNL received samples 1 and 3, while INL received samples 2 and 4. The sample cutting scheme is shown in Figure 3.44.

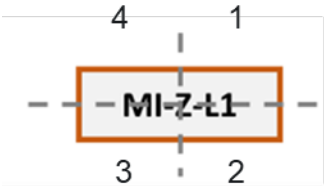

Figure 3.44. Sample cutting scheme for MI-Z-L1. Numbers 1 through 4 indicate sample number in the cutting scheme, with samples 1 and 3 shipped to PNNL, and 2 and 4 shipped to INL.

To pot and polish the laser welded sample, it was decided to cut the sample longitudinally into three sub-samples, and orient the cut surfaces down in the potting and polishing process. Three of these longitudinal samples were able to be potted in one epoxy puck, as depicted in Figure 3.45.

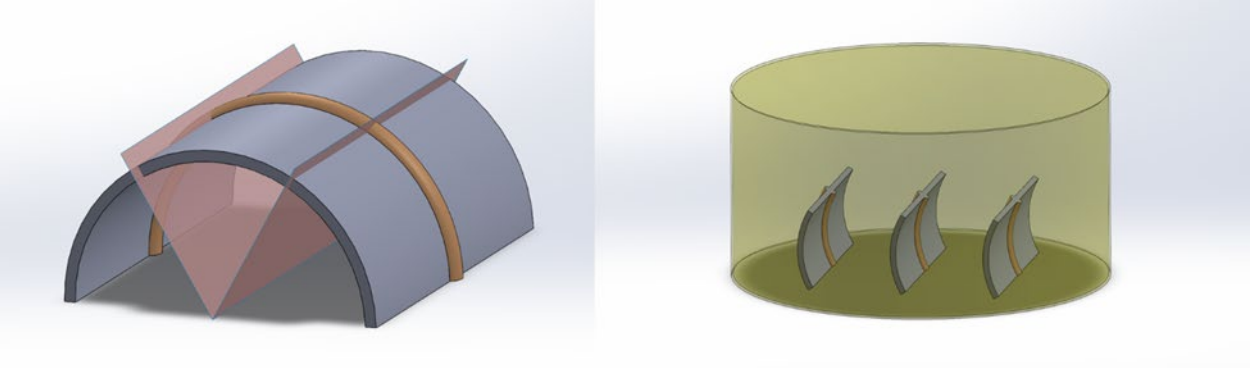

Figure 3.45. Cut and mounting diagram for MI-Z-L1-1 and MI-Z-L1-3.

The longitudinal lengths imaged on the OM post polishing are shown in Figure 3.46.

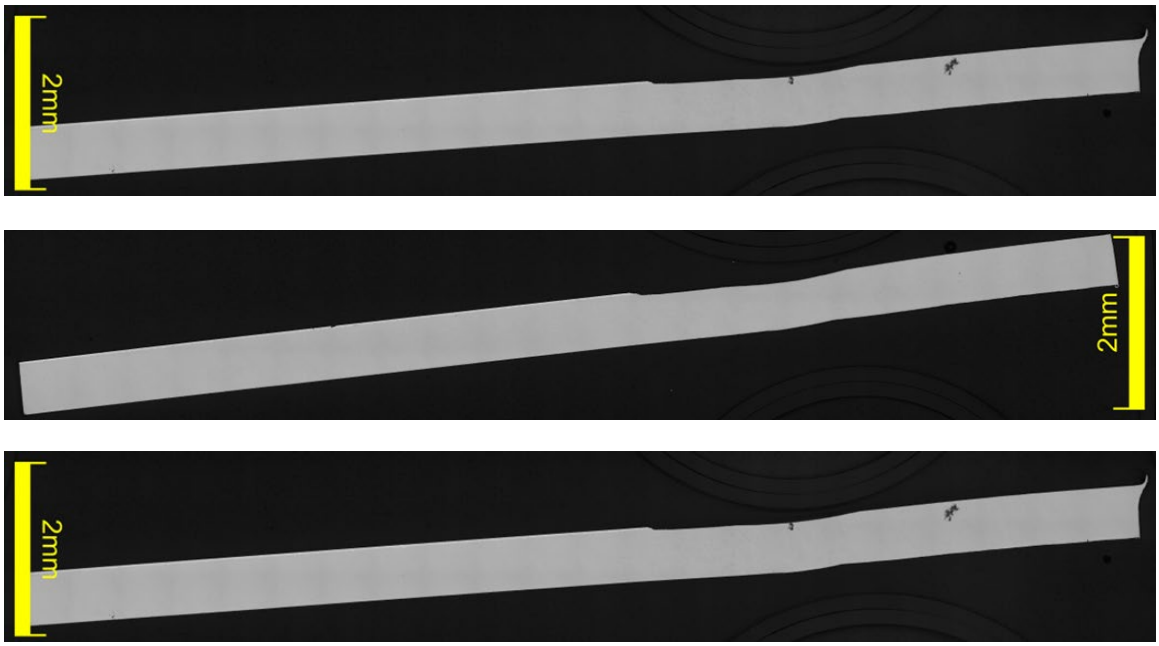

Figure 3.46. Polished longitudinal edges of MI-Z-L1-1, sample 1, 2, and 3. The welded area has lost straightness.

The laser polished sample exhibited smooth polished surfaces with no observable hydrides. The welded area was clearly visible based on the alignment of the sample and the lack of Cr-coating in the area. The sample lost straightness in this area as observed in Figure 3.46.

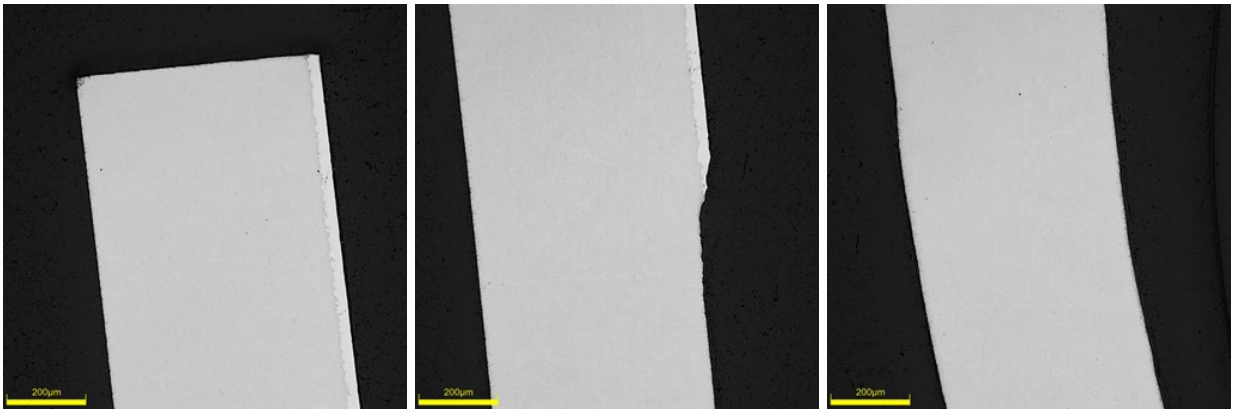

Figure 3.47. Polished images of the welded MI-Z-L1-1 S2 sample, showing the thickness of the Cr-coating (left), the start of the laser weld area (center), and the weld area (right).

These observations were consistent across the welded sample in the MI-Z-L1-1 sample. The laser weld area exhibited a lack of straightness, and the Cr-coating was intact aside from the weld area (which was uncoated and expected). No notable or observable defects or deformities were observed in sample MI-Z-L1-1 in the OM analysis.

The second laser sample, which captured the second weld on the parent sample, was also prepared in the same longitudinal manner, and potted in epoxy and polished for OM observation. Figure 3.48 shows the longitudinal images from the OM, with the samples showing high variability in straightness in the welded zone nearing the center of the specimen. In agreement with the L1-1 sample, the L1-3 laser welded sample exhibited no hydrides in the material.

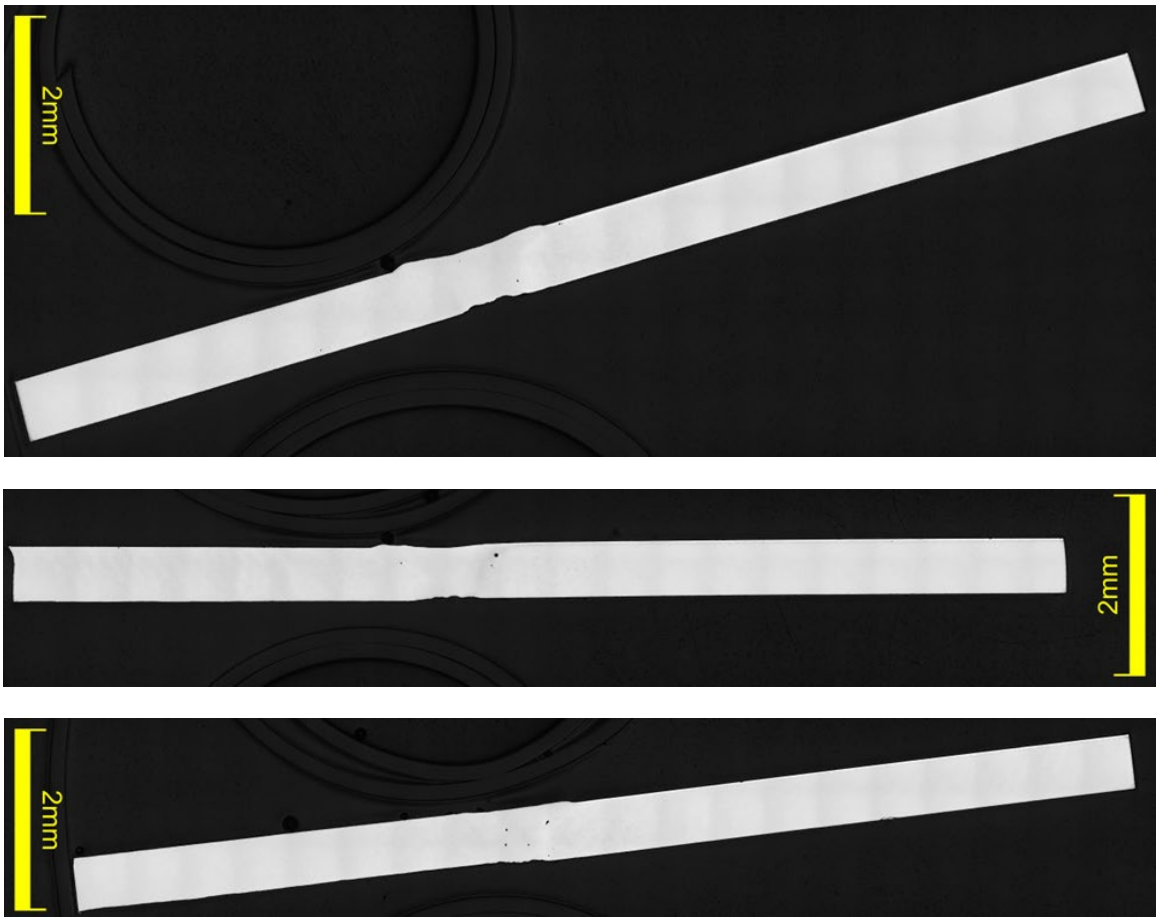

Figure 3.48. Polished longitudinal edges of MI-Z-L1-3, samples 1, 2, and 3.

Images of the welded zone show high variability and deformity in the general welded area. It is unclear what the black speckles observed in the welded area are, but given they are concentrated in the heat affected weld area, this could be a consequence of the welding process as opposed to debris remaining from potting and polishing process. The variability in the weld area and black speckling was further pronounced in Figure 3.49.

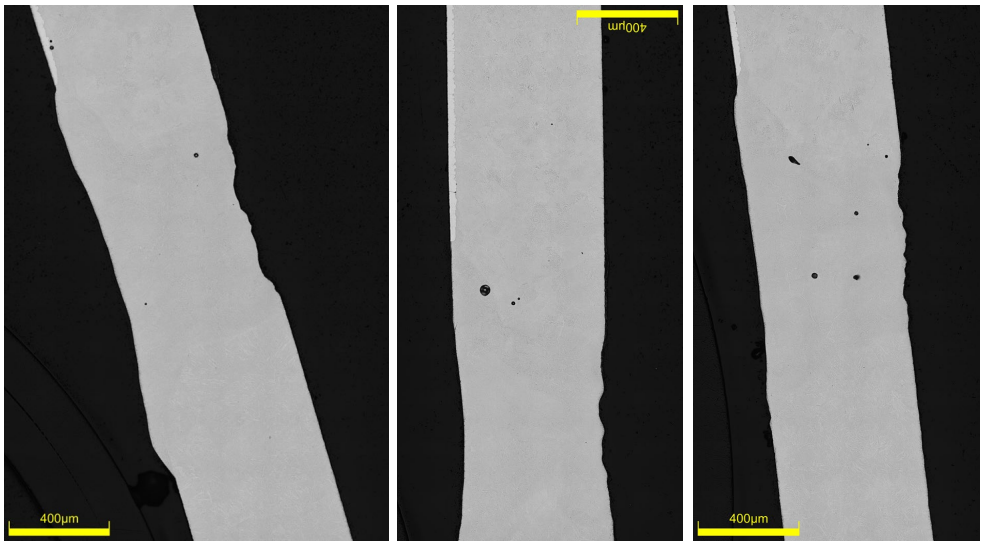

Figure 3.49. Variability in the welded area of MI-Z-L1-3, samples 1, 2, and 3.

The regions from Figure 3.49 were further examined with SEM and EDS. The Cr-coating possessed the typical microstructure observed for the CS coating. There was no evidence of hydriding. The SEM was not effective at visualizing differences distant from the weld region. It was not possible to obtain EBSD from the zircaloy in these areas. The Cr-coating had variable thicknesses ranging from 10 µm to 30 or 40 µm at times. Figure 3.50 shows high resolution images of the Cr-coating.

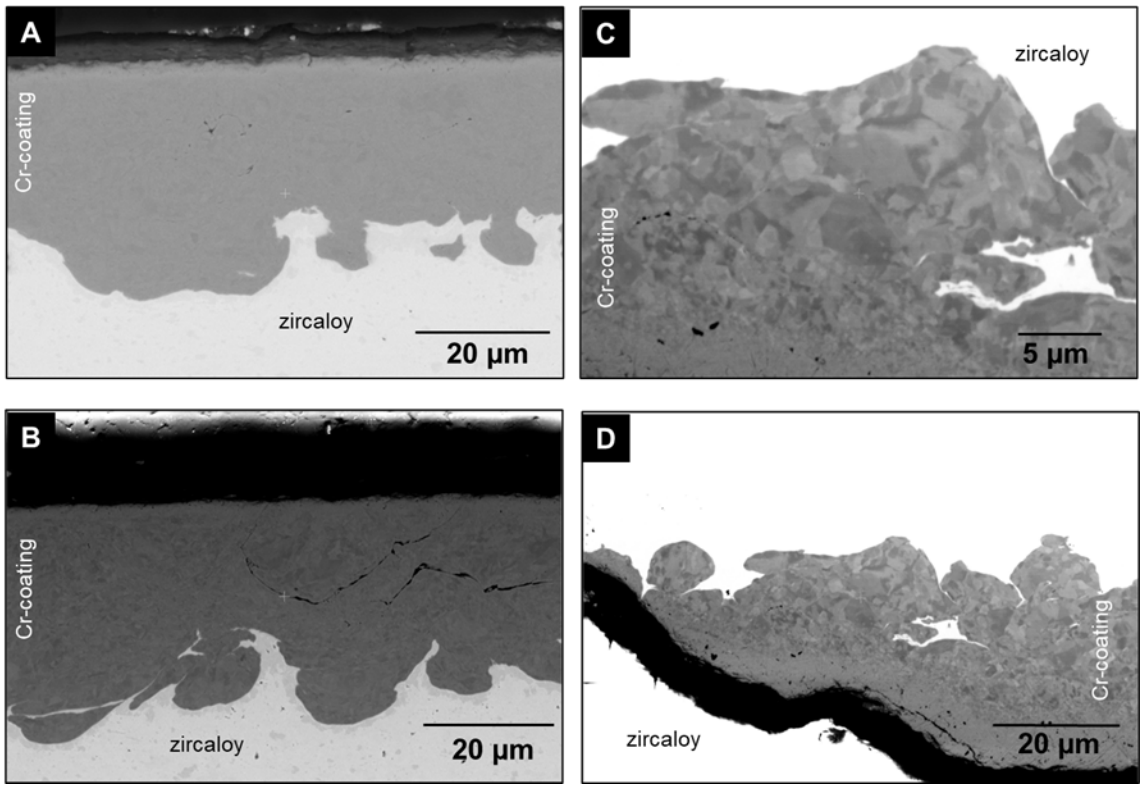

Figure 3.50. SEM detailed analysis of the Cr-layer on specimen M1-Z-L1-1.

SEM-EDS analysis of the Cr-coating is shown in Figure 3.51 and near the weld region in Figure 3.52. The Cr-coating terminates in the weld region and there was evidence of a minute amount of corrosion in the non-coated area (Figure 3.53). However, this would need to be confirmed with high resolution methods.

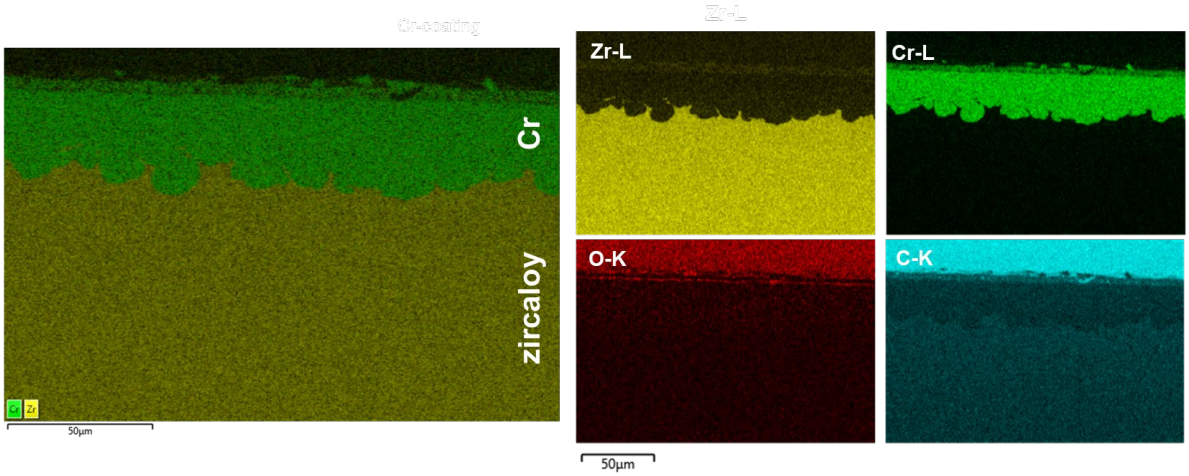

Figure 3.51. SEM-EDS analysis of the Cr-coated cladding in MI-Z-L1-1 showing minor evidence of an oxide layer on the outermost surface.

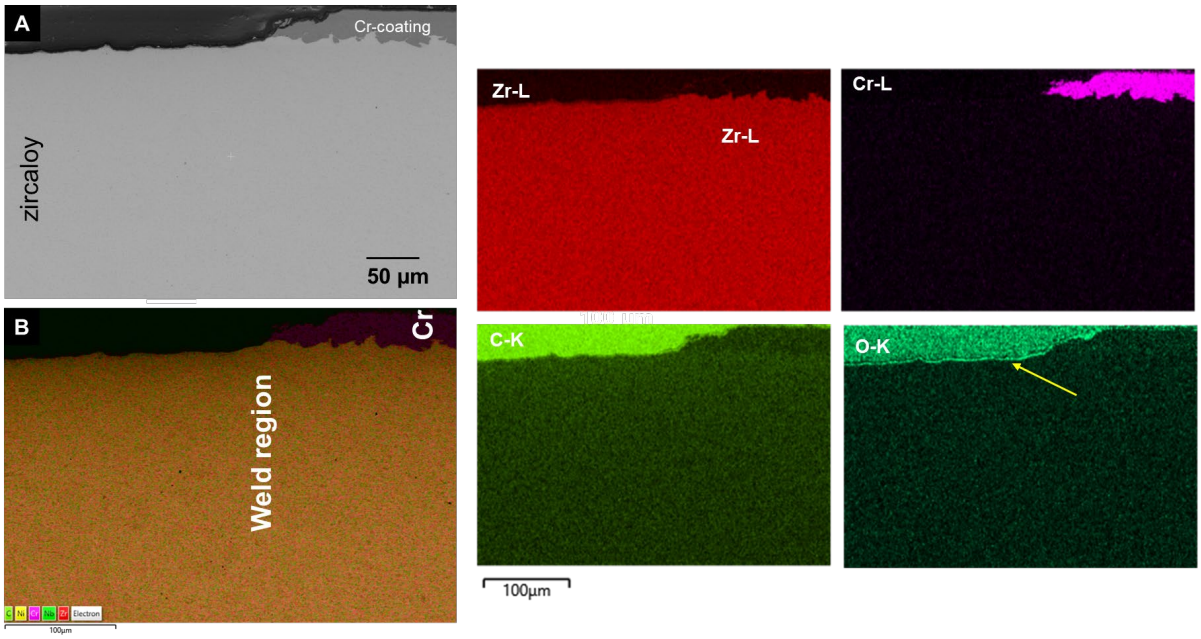

Figure 3.52. SEM-EDS analysis and elemental maps of the weld region in MI-Z-L1-1 showing a clear oxide layer on the non-coated region of the specimen.

Another example of SEM-EDS analysis of the Cr-coating is shown in Figure 3.53. In this series of images, a small crack can be seen running vertically from the surface of the coating. The O-map indicates that this area oxidized. This is an excellent example showing that Zr oxidizes faster than Cr in water at approximately 300°C.

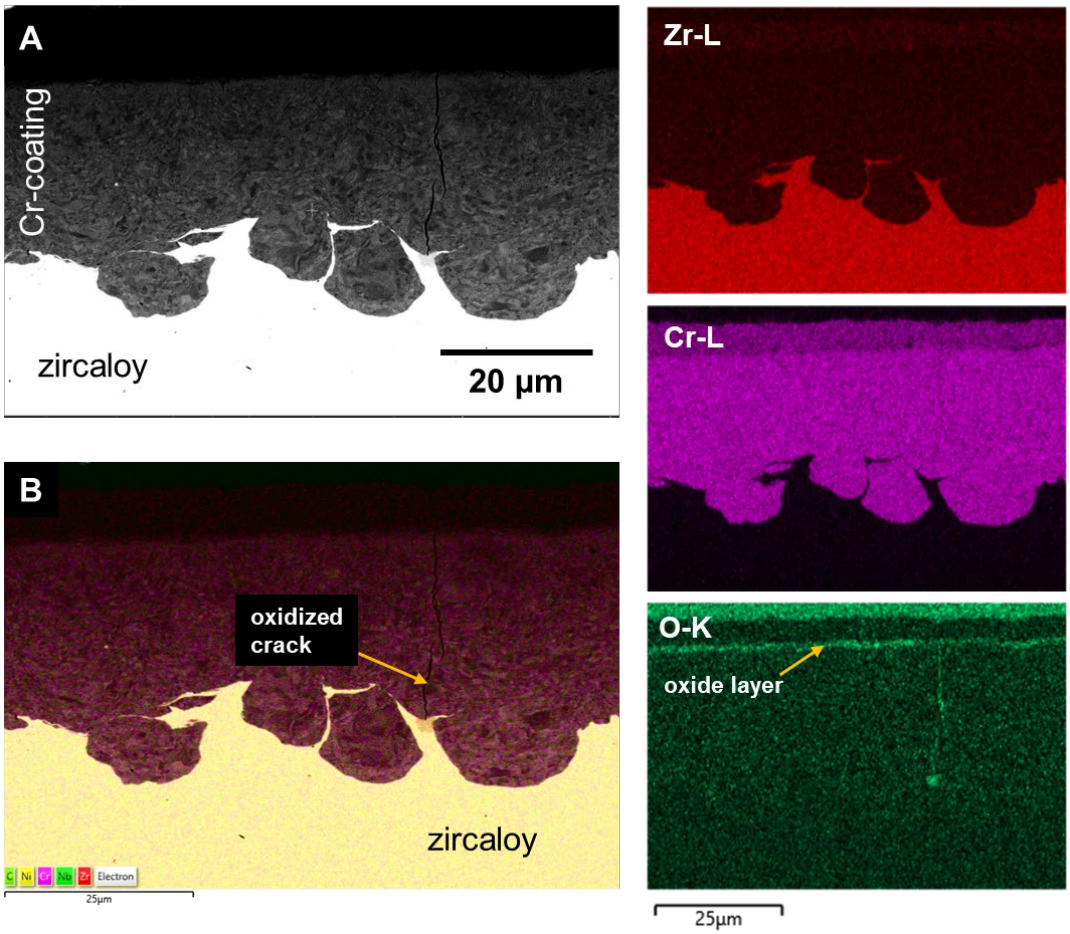

Figure 3.53. SEM-EDS analysis of the Cr-coating showing a small crack in the layer that has undergone corrosion.

To determine the baseline hardness of the two fused materials, microhardness measurements were taken far from the weld in either direction. The manufacturing process for the fused materials is unknown and therefore the only distinguishing feature is the presence or lack of chromium coating. Figure 3.54 shows an example of location selection and indents for baseline material hardness measurements. Table 3.7 and Table 3.8 report the measurements for each sub sample and total average hardness for uncoated and coated material respectively.

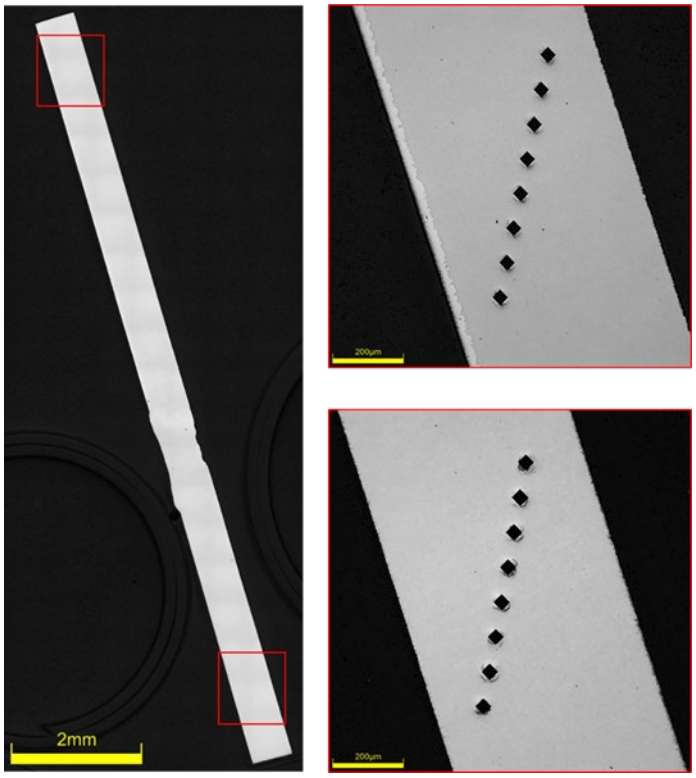

Figure 3.54. Location and indents for MI-Z-L1-3 S1 baseline coated and uncoated hardness measurement.

Table 3.7. Bulk microhardness measurements for uncoated material.

Sample ID	Microhardness Measurements HV	Sample Avg, Std HV	Material Avg, Std HV
MI-Z-L1-3 S1	271, 260, 277, 263, 268, 258, 244, 273	264 ± 10	264 ± 8
MI-Z-L1-3 S2	272, 262, 268, 267, 268, 262, 255, 243	262 ± 9	
MI-Z-L1-3 S3	270, 269, 258, 270, 265, 257, 262, 263	264 ± 5	

Table 3.8. Bulk microhardness measurements for coated material.

Sample ID	Microhardness Measurements HV	Sample Avg, Std HV	Material Avg, Std HV
MI-Z-L1-3 S1	285, 284, 285, 285, 284, 281, 286, 279	284 ± 2	282 ± 3
MI-Z-L1-3 S2	283, 283, 283, 283, 279, 280, 272, 280	280 ± 4	
MI-Z-L1-3 S3	284, 282, 283, 281, 281, 282, 276, 281	281 ± 2	

To construct a hardness profile for the weld, an initial line of hardness indents was taken with a coarse spacing of 0.25 mm from center point to center point. This line was used to help identify the edges of the fusion zone. Two more lines of indents were then taken with a finer spacing of 0.1 mm to increase the sample size, especially in the areas where one might expect to see the

transition from bulk material to the heat affected or fusion zones. Figure 3.55 shows an example of this measurement scheme for the MI-Z-L1-3 S2 sub sample.

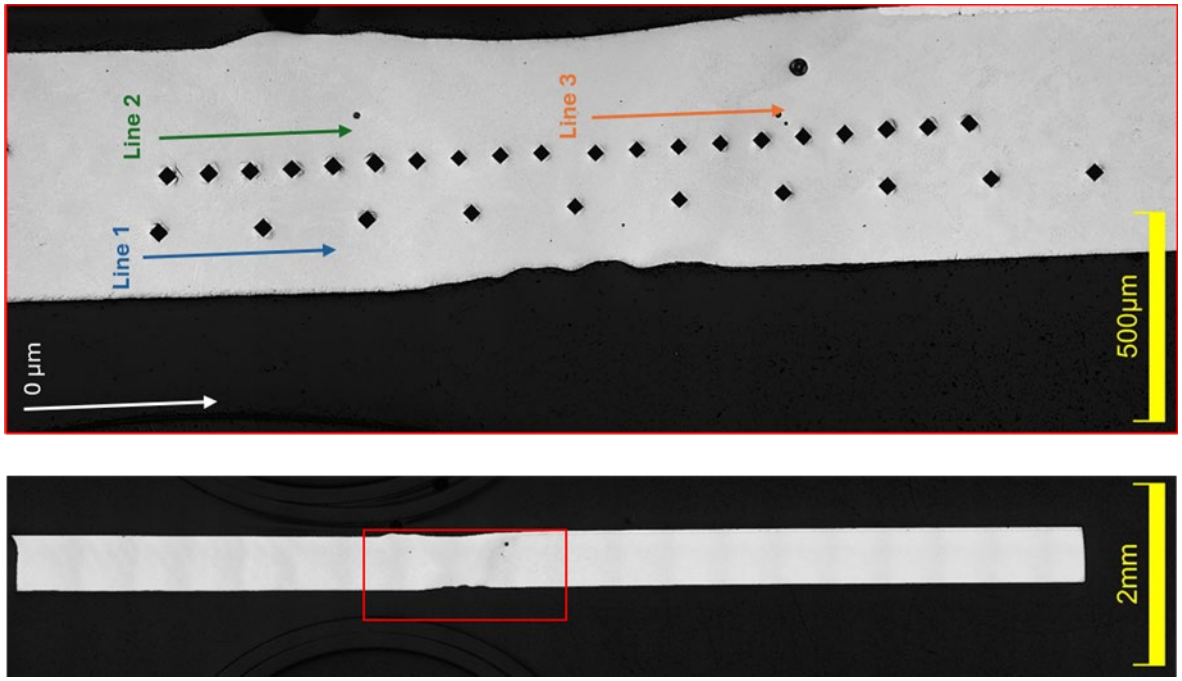

Figure 3.55. Weld hardness profile example measurement scheme for MI-Z-L1-3 S2.

This measurement profile was repeated for each subsample, with the values in agreement in each profile measurement. Figure 3.56 shows a plot of the weld hardness profile for sub sample MI-Z-L1-3 S2, which mirrored the results of all the weld profiles. In the plot, the distance on the x-axis is measured from the top edge of the image as indicated by the white arrow in Figure 3.55. Measurements were taken using the open-source software ImageJ and based on the scale bar in each image. These measurements should only be used to determine the relative distance between indents to show the weld hardness profile. Table 3.9 reports the measurement values for the MI-Z-L1-3 weld profiles.

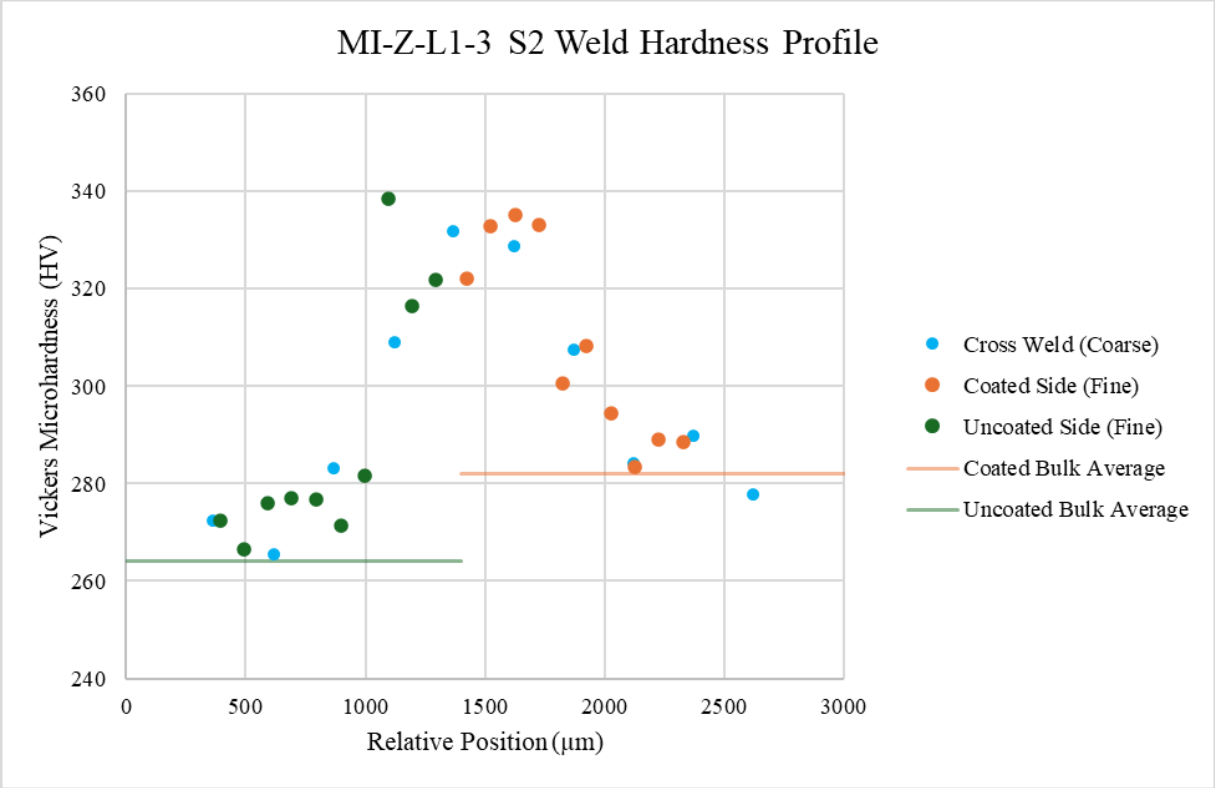

Figure 3.56. Weld hardness profile of MI-Z-L1-3 S2.

Table 3.9. Weld hardness profile measurements of MI-Z-L1-3.

Sample ID	Line ID	Microhardness Measurements HV	Line Min, Max HV	Sample Min, Max HV
MI-Z-L1-3 S1	Cross Weld (Coarse)	290, 304, 300, 317, 320, 320, 347, 258, 267, 287	258, 347	256, 347
	Coated Side (Fine)	295, 291, 291, 305, 292, 309, 332, 316, 328, 330	291, 332	
	Uncoated Side (Fine)	322, 320, 321, 335, 281, 274, 275, 265, 256, 271	256, 335	
MI-Z-L1-3 S2	Cross Weld (Coarse)	278, 290, 284, 307, 329, 332, 309, 283, 265, 272	265, 322	265, 338
	Coated Side (Fine)	289, 289, 283, 294, 308, 301, 333, 335, 333, 322	283, 335	
	Uncoated Side (Fine)	322, 316, 338, 282, 271, 277, 277, 276, 267, 272	267, 338	
MI-Z-L1-3 S2	Cross Weld (Coarse)	293, 292, 310, 324, 325, 331, 319, 268, 262, 273	262, 331	251, 345
	Coated Side (Fine)	299, 304, 307, 294, 282, 288, 331, 345, 326, 333	282, 345	
	Uncoated Side (Fine)	330, 330, 285, 267, 276, 257, 251, 272, 264, 261	251, 330	

3.2.2.6 Out-of-Core Physical Vapor Deposition Cr-Coated Materials

The out-of-core PVD samples had two different thicknesses of Cr-coating, 5 µm and 10 µm. These samples were situated in the out-of-core testing loop and subjected to the same water chemistry and temperature as in-core materials. Due to time constraints, only the out-of-core sample with the Cr-coating of 10 µm was studied. The parent sample, MO-Z-P2, exhibited a metallic, golden straw colored finish, as observed in Figure 3.57.

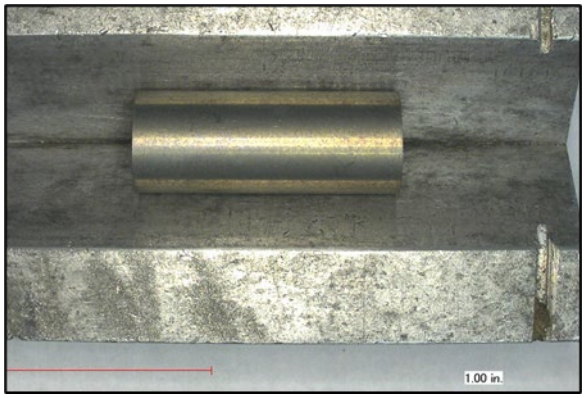

Figure 3.57. Out-of-core PVD Cr-coated sample MO-Z-P2.

Samples were prepared for metallography per Section 3.0, and imaged using OM. The polished PVD Cr-coated specimen showed a thin Cr-coating on the outer diameter. Notably, hydrides are observed in the greater magnification OM image, as seen in Figure 3.58, though not as prevalent as in the CS Cr-coated counterpart (MO-Z-C1 samples).

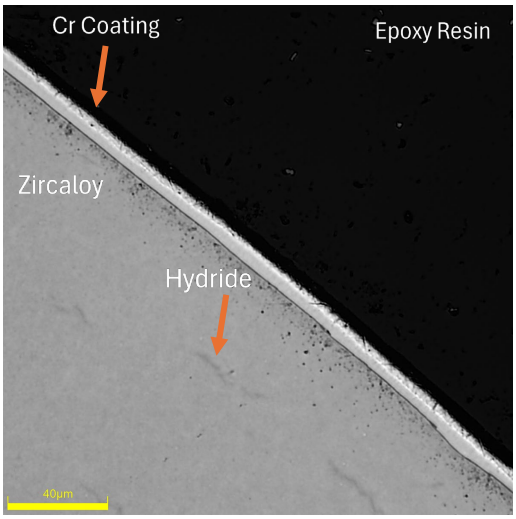

Figure 3.58. Polished OM image of the MO-Z-P2-1 S2 cladding showing the PVD Cr-coating/substrate interface, with hydrides observed in the substrate.

The polished OM images at lower magnification illustrate the distribution of the hydrides throughout the substrate, Figure 3.59. The hydrides are short in length, but are mostly evenly distributed throughout the cladding substrate with the exception of near the inner diameter. Hydride clustering was not observed in the sample, which would be indicative of a surface coated defect (C. Varvenne et al. 2016).

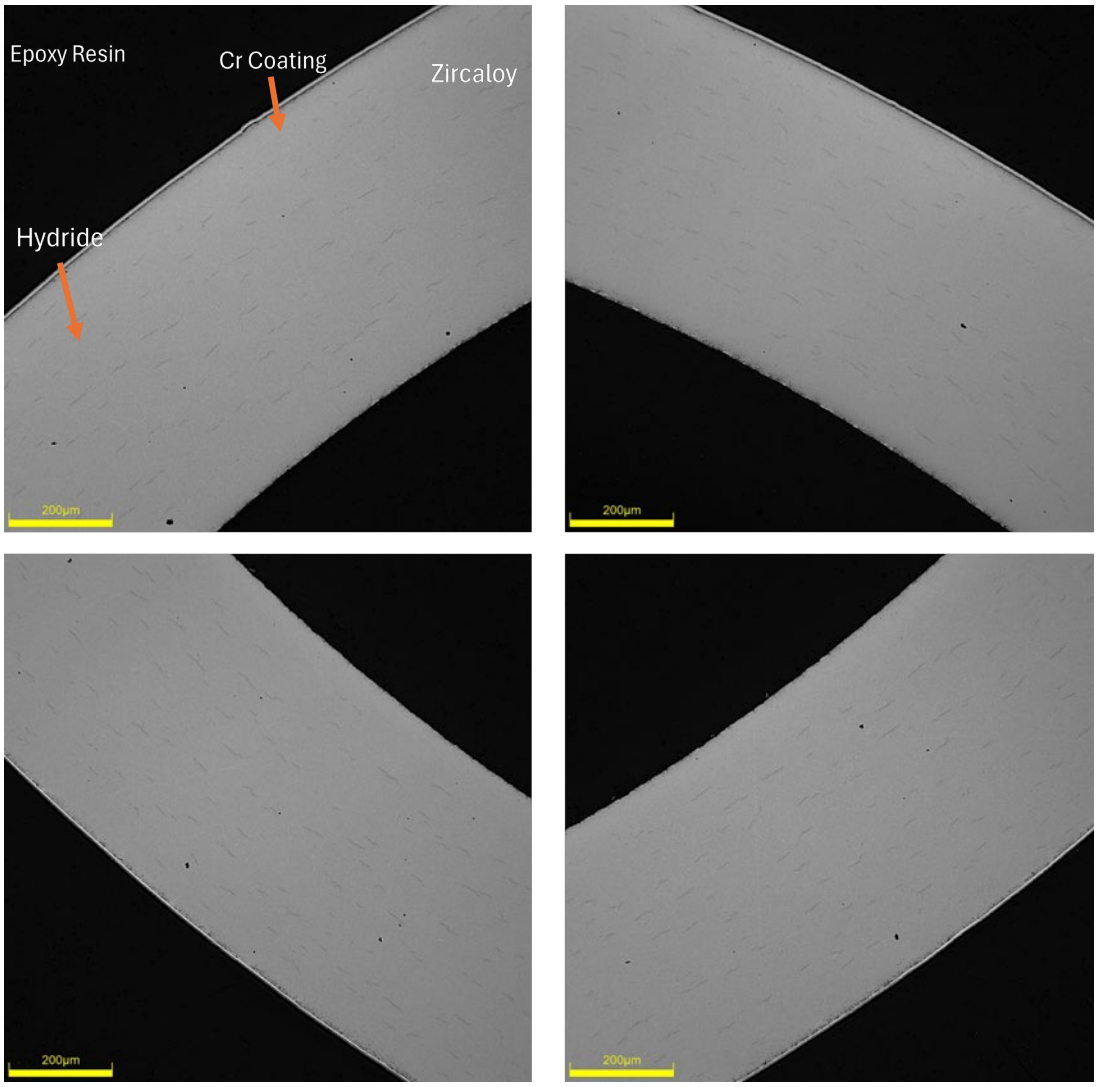

Figure 3.59. Polished OM images of MO-Z-P2-1 S2 showing portions of quadrants A, B, C, and D (clockwise from the top right) with clear hydrides visible.

SEM and EDS analysis of the PVD coated Cr-coated sample had significant differences from the other coating methods. There appeared to be evidence of a thin oxide layer between the Zircaloy and the Cr-coating (see Figure 3.60).

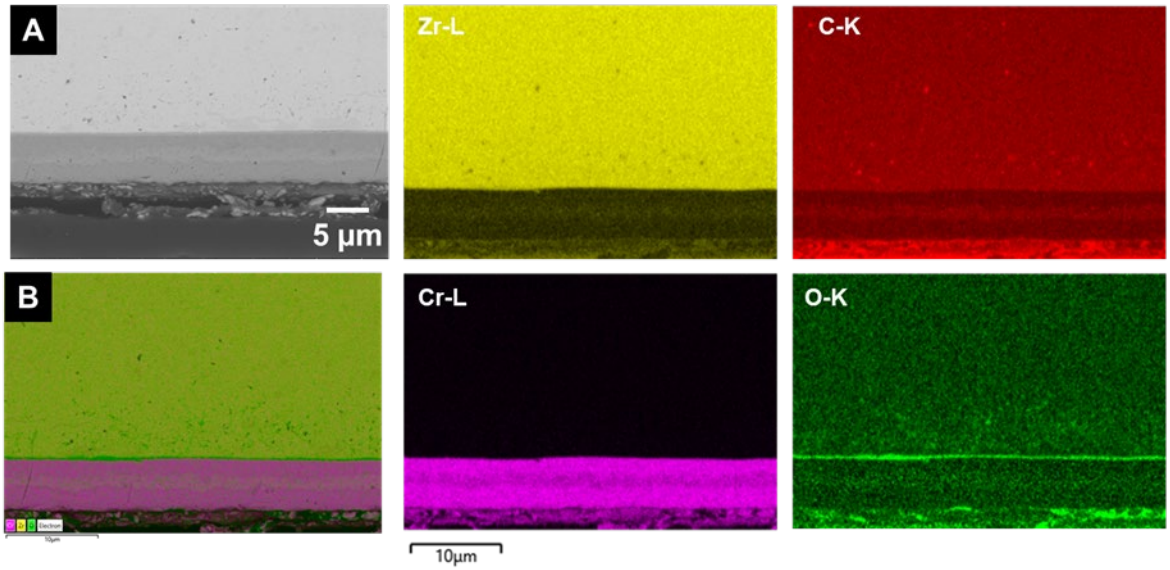

Figure 3.60. SEM/EDS analysis of the out-of-core PVD sample showing the occurrence of an oxide layer between the Zircaloy and the Cr-coating. Contrast within the layer also indicates compositional variations within this layer.

This SEM-EDS analysis was taken further with the results shown in Figure 3.61. There a thin oxide layer between the Zircaloy and the Cr-coating was observed, again showing that Zr oxidizes much faster than Cr in water at approximately 300°C, and there was enrichment of Cu within the Cr-layer. The bond between the Cr-coating and the Zircaloy appeared to be much poorer than in the CS method.

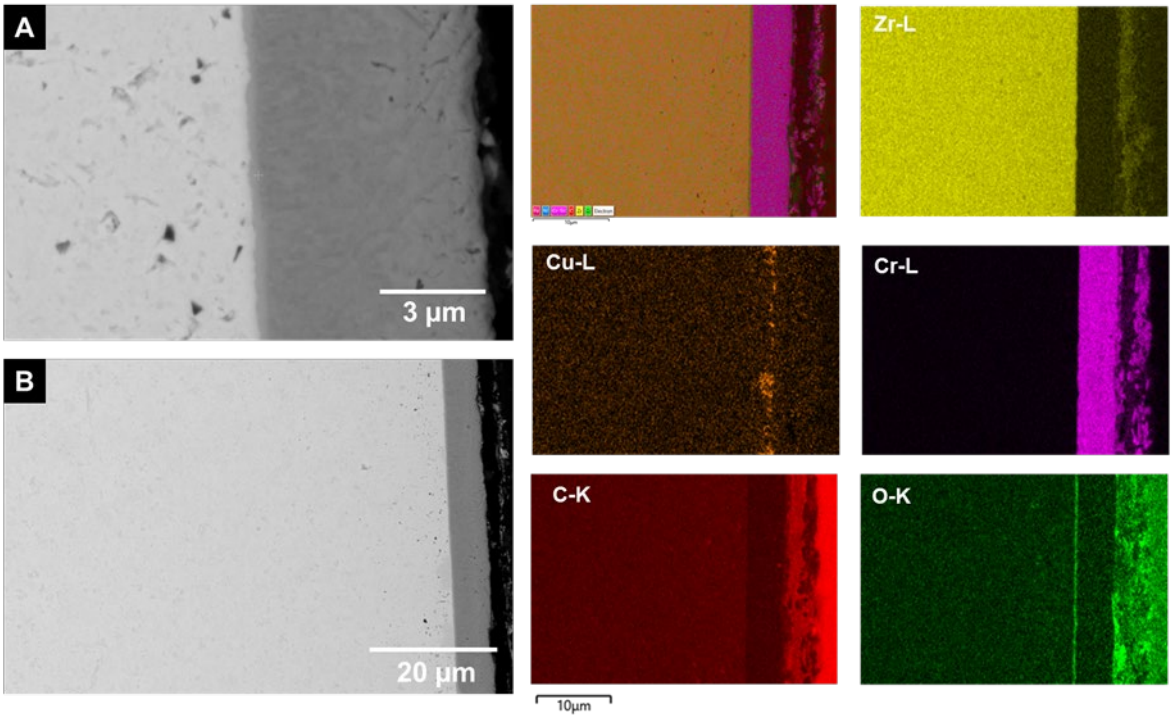

Figure 3.61. SEM/EDS analysis of the Cr-coated material showing the occurrence of a thin oxide layer between the Zircaloy and the Cr material, and evidence of Cu segregation within the Cr-layer. There may also be an oxide layer on the outer surface of the Cr.

3.2.3 In-Core Physical Vapor Deposition Cr-Coated Materials

Specimens from the in-core PVD coated samples were either 5 µm or 10 µm in coating thickness. These samples were situated in the in-core testing region, and as such were subjected to radiation from the core, as well as chemistry-controlled water and a controlled water temperature.

The in-core sample with a 5 µm coating (MI-Z-P1) was observed to have a slightly variable color up the length of the sample of slightly gold to a deeper blue metallic color, Figure 3.62, which could be attributed to oxide thickness generated on the outer layer of the Cr-coating. Two 3 mm samples were cut from this parent sample to analyze for any difference across the color variation.

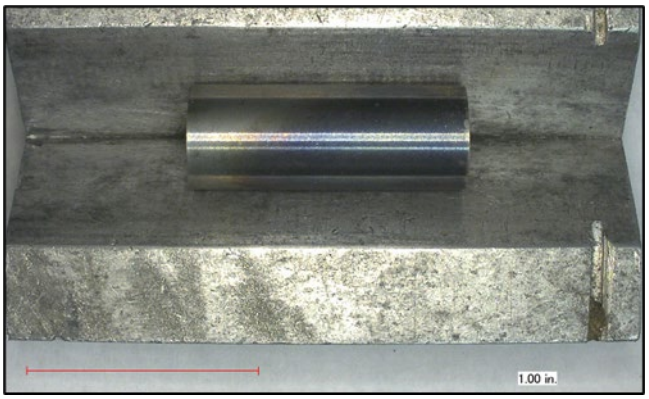

Figure 3.62. In-core PVD Cr-coated sample MI-Z-P1.

The sample was prepared for metallography as prescribed in Section 3.0. Higher magnification OM images showed smooth, polished surfaces in both samples, with thin Cr-coating films on the outer diameter of the sample. No visible oxide layer was observed at this magnification on the outer diameter. Small hydrides were visible in both samples, which can be seen as slightly darker lines in Figure 3.63.

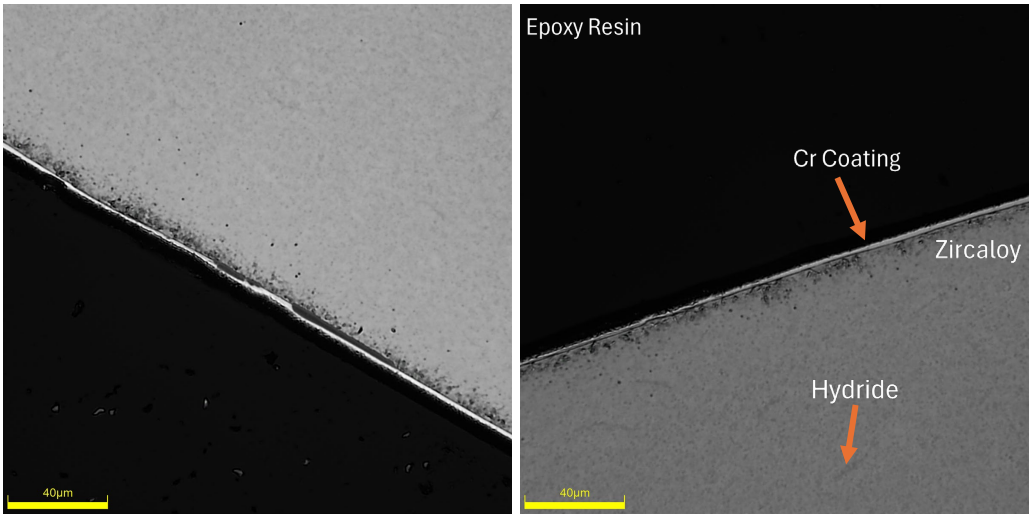

Figure 3.63. Polished OM image of the MI-Z-P1-1 S1 (left) and MI-Z-P1-1 S2 (right) cladding showing the PVD Cr-coating/substrate interface, with minor observed hydrides in the substrate.

Polished OM images at lower magnification further illustrate the distribution of small hydrides in the substrate. As these hydrides were more difficult to observe, the red boxes in Figure 3.64 highlight some of the hydrides observed. These hydrides are small, short hydrides, and appear to be evenly distributed throughout the substrate again, with the exception of a small gap nearing the inner diameter. No clustering of hydrides was observed in the sample.

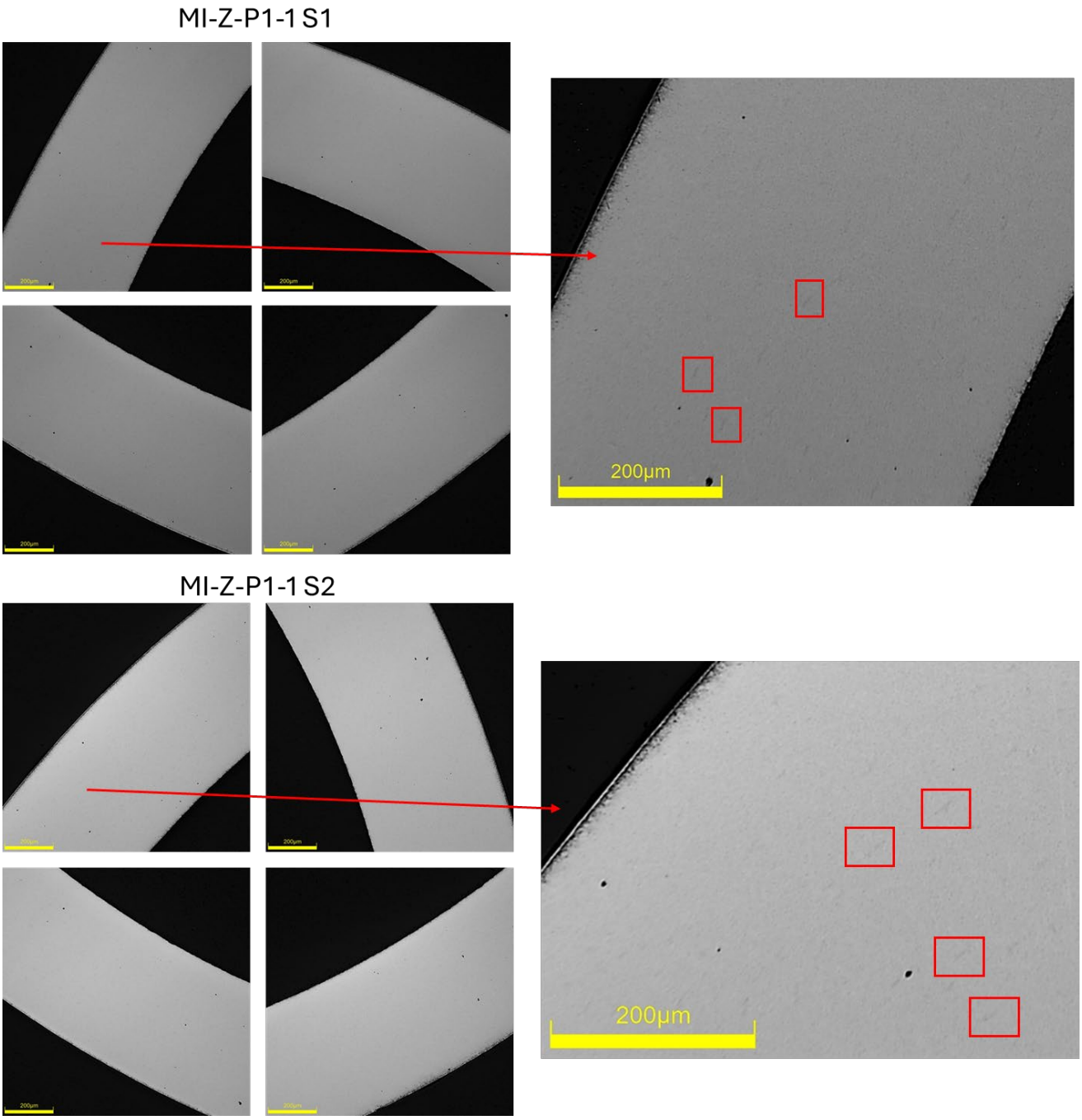

Figure 3.64. Polished OM images of MI-Z-P1-1 S1 and MI-Z-P1-1 S2 showing portions of quadrants A, B, C, and D (clockwise from the top right) with very minor visible hydrides in the substrate. Images with increased size show a small selection of hydrides (red squares).

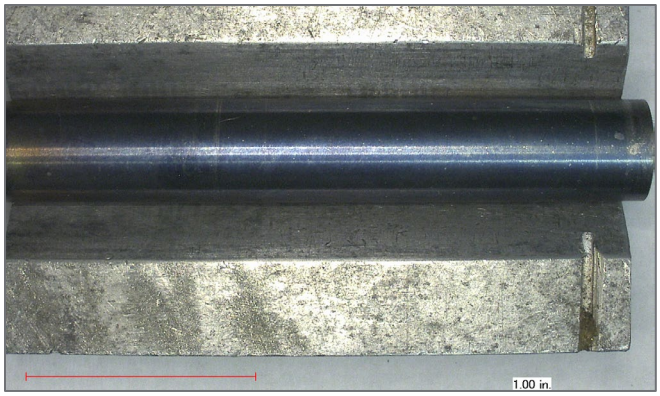

Figure 3.65. In-core PVD Cr-coated sample MI-Z-P2.

The second in-core sample with 10 µm coating (MI-Z-P2) was observed to have a mostly metallic blue coloration to it, with the exception of one end of the sample which was slightly lighter gold in color, Figure 3.65. This color difference is likely attributed to oxide layer thickness variations. One 3 mm sample was cut for analysis.

The polished OM image at increased magnification exhibited the thicker PVD Cr-coating on the sample with an intact exterior, Figure 3.66. No visible hydrides were readily observed in the OM image on the left, but the right image showcases some small minor hydride formation (red box).

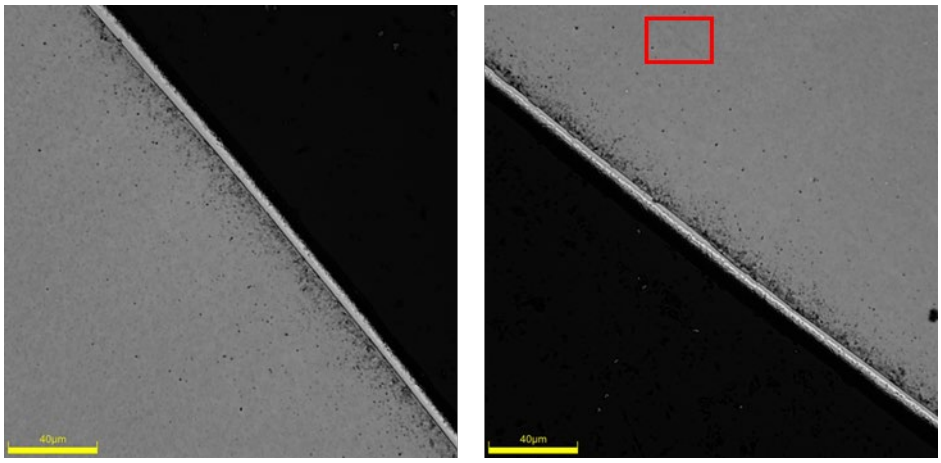

Figure 3.66. Polished OM image of the MI-Z-P2-1 S2 cladding showing the PVD Cr-coating/substrate interface. (Right) The red box is highlighting a hydride in the substrate.

Lower magnification polish OM images did not readily illustrate the small hydrides in the sample substrate, Figure 3.67. The polished sample showed smooth surfaces otherwise, with no notable defects in the coating, and no hydride clustering.

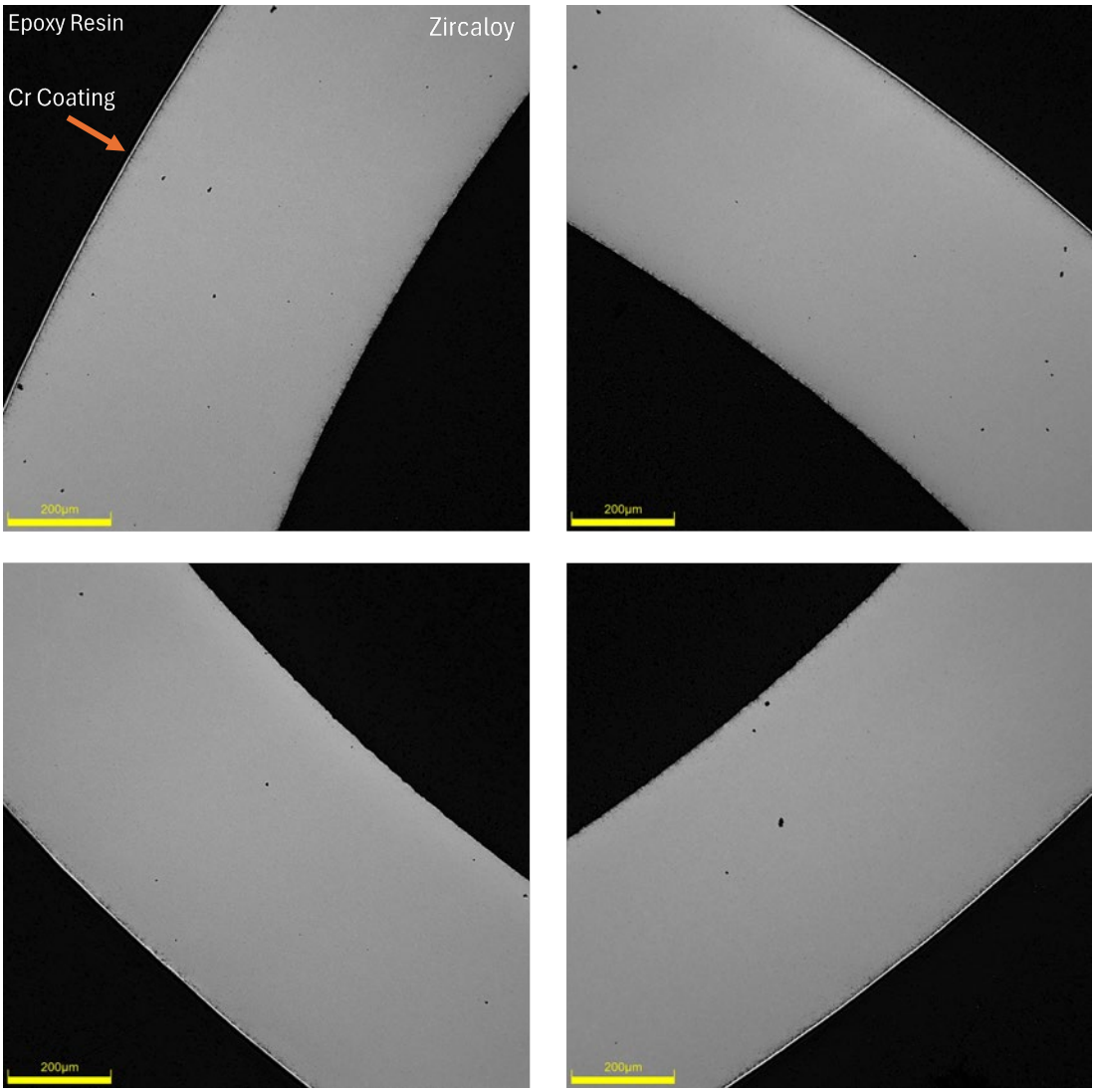

Figure 3.67. Polished OM images of MI-Z-P2-1 S2 showing portions of quadrants A, B, C, and D (clockwise from the top right). Minor hydrides are present but difficult to observe at this magnification.

3.3 Automated Hydrogen Analysis

The quantification of hydrides has been discussed and previously studied using various software packages to aid in analysis of micrographs, many of which center on radial hydrides (M. Maric et al. 2022; R.S. Daum et al. 2009; K.B. Colas et al. 2013). Using software and coding, radial hydride fractions within micrographs were analyzed and studied both qualitatively and quantitatively to streamline image analysis. This work also aimed to quantify hydrides using a streamlined image analysis that could provide source information in future hydride modelling efforts.

To quantify the hydrides observed in the OM images in support of generating a predictive model of hydride formation in cladding variants, a script was written in Matlab R2025b. This script leveraged the image processing toolbox to analyze OM images of the cladding in batches for hydride area fraction. Claude (Sonnet 4.6) was utilized to help write the script, and the main

driver script and its associated functions were reviewed and tested. Due to the time constraints the script was not fully optimized and may not provide perfect results for every image in a batch.

The script used a series of functions and iterated over all image files identified in a user-configured directory. First, the scale bar is cropped out, and the sample region is isolated using Otsu thresholding to separate the dark background from the bright cladding. Then, Canny edge detection is used to identify the boundary between the zircaloy substrate and the Cr-coating. Based on where that interface is in the image, the area outside the boundary is masked to remove the Cr-coating, which does not contain hydrides and would drive down the area fraction estimate (Figure 3.68).

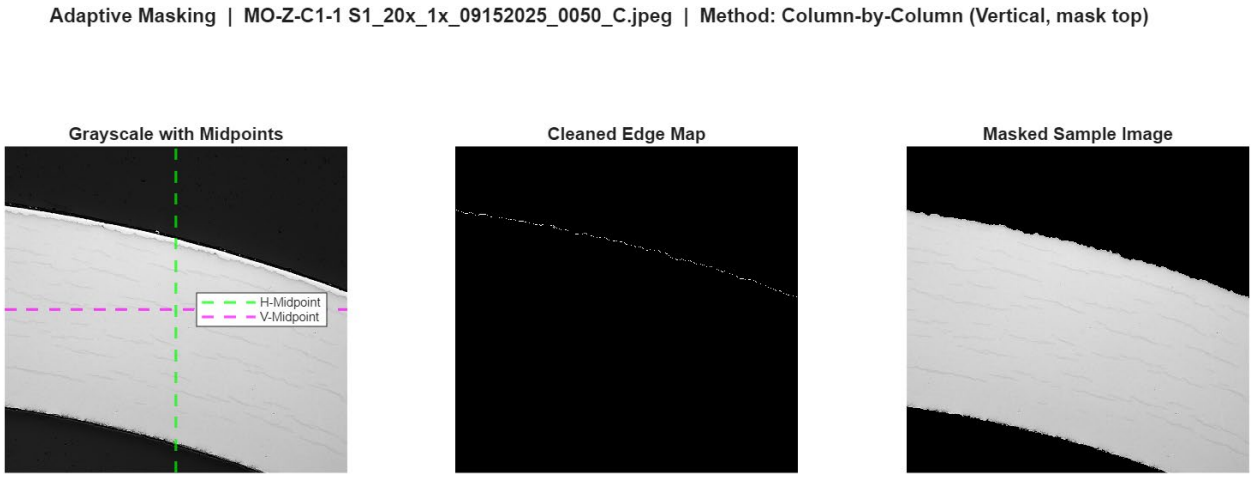

Figure 3.68. MO-Z-C1-1 S1 coating/substrate interface detection and masking

With the image fully masked, Sauvola adaptive thresholding was used to segment the remaining area. Objects smaller than a minimum hydride size configured by the user were removed from the binary image (Figure 3.69).

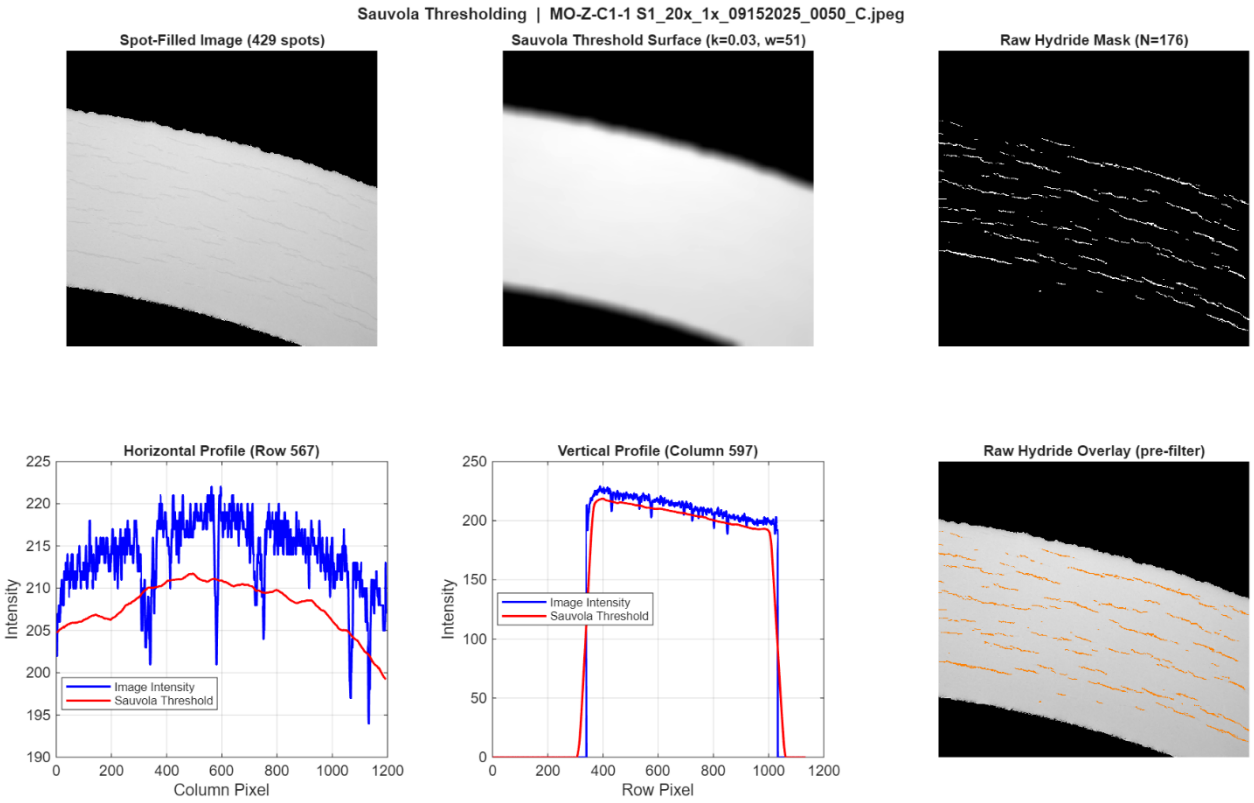

Figure 3.69. Sauvola thresholding process for sample MO-Z-C1-1 S1.

Additionally, a circularity filter was applied to the binary to remove any objects that exceed the minimum hydride size but are clearly not hydrides. In observation, hydrides form long, narrow, objects, so filtering based on circularity works well to remove artifacts like dust particles or pits (Figure 3.70).

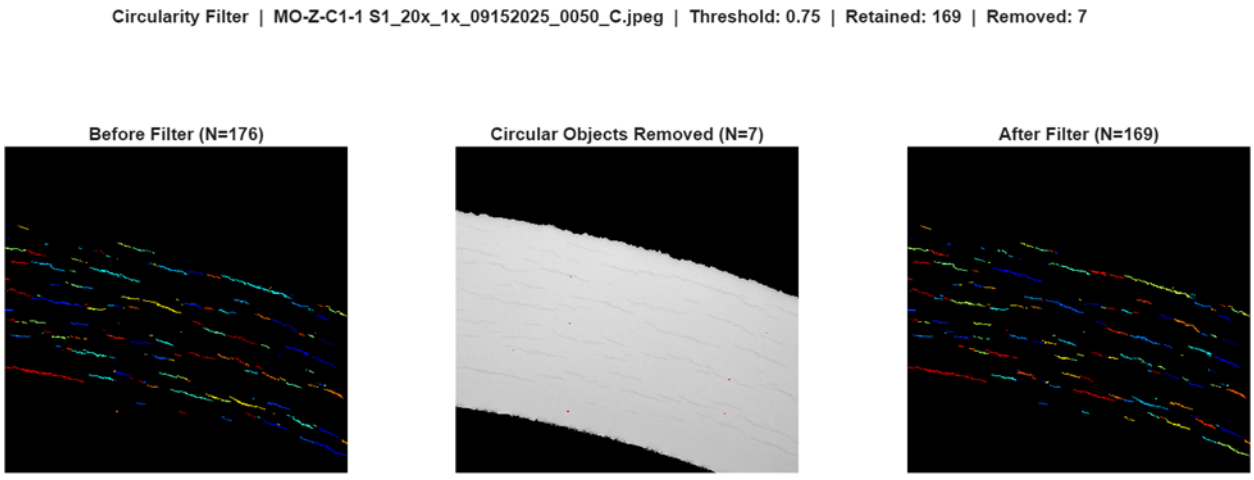

Figure 3.70. Circularity filter visualization for sample MO-Z-C1-1 S1.

Objects in the final binary image were then identified and measured (Figure 3.71). A comma-separated values (.csv) file was generated for each image that reported individual hydride sizes in pixels, an area fraction summary, and other basic statistics. A visualization report was also

provided for each image detailing the processing and results. Visualization and data reports for the entire batch were also provided.

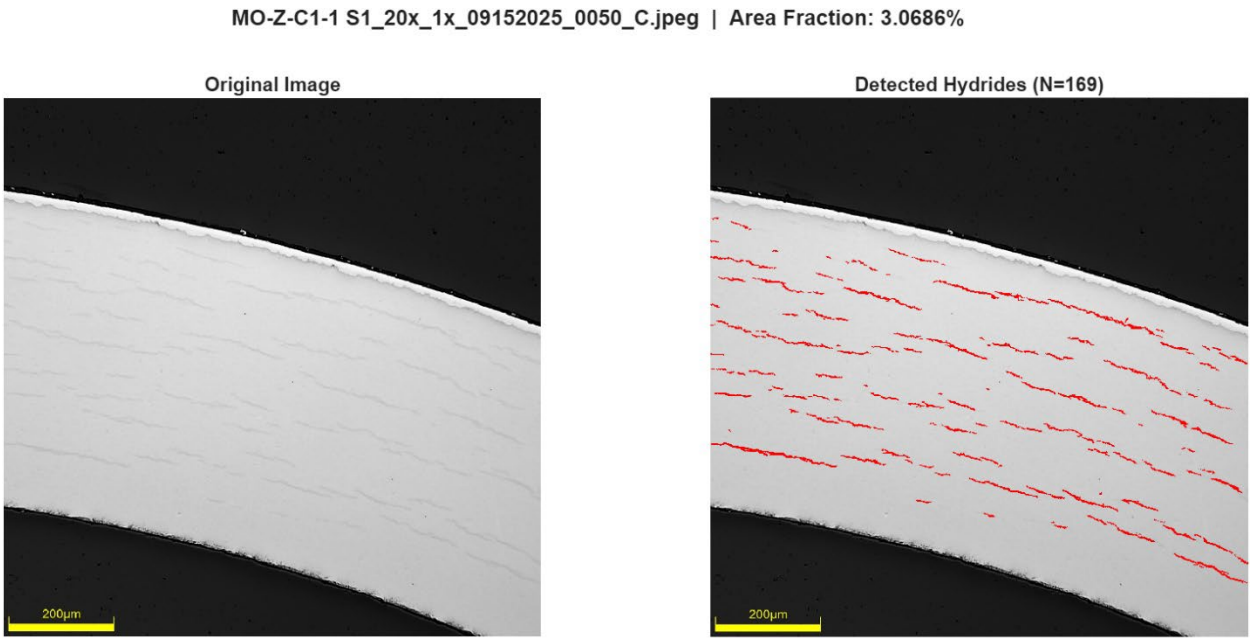

Figure 3.71. Example image original and final result of Hydride analysis script for sample MO-Z-C1-1 S1.

The hydride area fraction f_a was computed as the ratio of the number of pixels classified as hydrides N_H to the total number of cladding pixels N_C within the analysis region:

$$f_a = \frac{N_H}{N_C}$$

If it is assumed that the area fraction is similar in all dimensions, then the area fraction becomes an estimate for volume fraction (i.e., $f_a \approx f_V$). The hydride weight fraction w_H can then be calculated from the volume fraction based on phase densities such that:

$$w_H = \frac{f_V \rho_H}{f_V \rho_H + (1 - f_V)\rho_{Zr}}$$

where the density of delta-hydride phase ($ZrH_{1.6}$) is taken as $\rho_H = 5.65$ g/cm^3 and the density of the zircaloy sample matrix is taken as 6.56 g/cm^3. The estimated bulk hydrogen concentration C_H in weight parts per million was then obtained:

$$C_H\ (\text{wppm}) = w_H x_H \times 10^6 = 0.1737 w_H \times 10^6$$

where x_H is the mass fraction of hydrogen in the delta-hydride phase ($ZrH_{1.6}$):

$$x_H = \frac{1.6\ M_H}{M_{Zr} + 1.6\ M_H} = \frac{1.6 \times (1.008 \frac{\text{g}}{\text{mol}})}{(91.22 \frac{\text{g}}{\text{mol}}) + 1.6 \times (1.008 \frac{\text{g}}{\text{mol}})} = 0.01737$$

It is assumed that all hydrogen in excess of the terminal solid solubility limit has precipitated in the delta-hydride phase ($ZrH_{1.6}$), with no retention in solid solution. This is reasonable at room temperature, where the terminal solubility of hydrogen in zircaloy is less than 1 wppm. Also, the stoichiometry of the delta-hydride phase is assumed to be uniform at $ZrH_{1.6}$. It must also be acknowledged that the area fraction measured from optical microscopic images encompassing a specific azimuthal position on the cladding cross-section may not be fully representative of the average bulk hydrogen content.

For the images of MO-Z-C1-1 S1, an average hydride area fraction from an analysis across multiple images was determined to be ~4.25% (noting that individual image area fractions varied, as shown in Figure 3.71, where one representative image yielded an area fraction of 3.07%). Using the equations above, this corresponds to hydrogen values greater than 700 wppm. However, hydrogen measurements obtained by inert gas fusion analysis (LECO ONH) show that these samples contain closer to 100 wppm hydrogen. It is possible that the hydride area fractions determined by image analysis will slightly exceed the true volumetric hydride phase fraction. Under the polarized light conditions used here, image contrast may arise not only from the hydride precipitates themselves but may also reflect crystallographic distortions in the surrounding zirconium matrix induced by the strain field associated with hydride formation. A darkened region around each precipitate would be captured during the threshold-based image segmentation, resulting in a systematic overestimate of the hydride area fraction.

The correlation between image-derived hydride area fractions and bulk hydrogen content established here is based on a limited number of samples and measurement locations. A robust, statistically validated correlation would require a significantly larger dataset spanning a wider range of hydrogen contents, sampling positions and a larger number of paired optical microscopic images and LECO measurements per sample to account for local variability. Nevertheless, the observed connection between image-derived hydrogen estimates and bulk measurements for the samples examined in this work is encouraging. The results demonstrate that threshold-based image segmentation of pre-etched polarized light images is viable with the potential to become a powerful tool for spatial characterization of hydride distribution in hydride loaded cladding. Further development of this approach, including expanded validation against a broader sample set, could ultimately enable quantitative hydrogen mapping around the circumference of individual fuel rods from routine metallographic examination.

3.4 Discussion

Samples visually differed among all variants – the uncoated, CS Cr-coated, PVD Cr-coated, and laser welded Cr-coated materials. Further, sample color variation was not consistent between in-core and out-of-core materials of different variants. This is characteristic of thin-film optical interference, where thickness variations on the outer diameter of the sample produced distinct color differences. However, color variations were mostly consistent, between variants of the same coating and sample in-core or out-of-core conditions.

Uncoated As-Manufactured Control Samples: The uncoated out-of-core and in-core samples both exhibited a silver metallic hue. Resulting OM from polished samples showed smooth surfaces with no observed hydrides, no notable surface defects in the substrate or coating, and no clearly visible oxide layers on either the inner or outer diameter. Imperfections in the samples were attributed instead to sample preparation artifacts. The uncoated out-of-core and in-core samples were analyzed by gas fusion analysis on the LECO instrument. The total bulk hydrogen content in the out-of-core sample reading was 12 wppm hydrogen, while the in-core sample

measured 20 wppm hydrogen. However, this difference in hydrogen concentration within the sample is not large.

Cold Spray Samples: The CS Cr-coated cladding exhibited a blue/purple hued exterior on the out-of-core cladding, and a straw/gold hue on the in-core cladding. This immediate difference indicates visually that the oxide layer thicknesses between the two samples likely differ.

The coating from the CS deposition process exhibited a lamellar structure with random grain orientation throughout the coating, with a mixture of large and small grains. Some highly deformed areas were suggestive of recrystallization, and a “splat-like” appearance was observed. Large, deformed grains within the specimens have been identified as splat particles. These splats were located alongside ultra-fine grain particle regions at the splat boundaries. The intrasplat spaces observed in the samples showed clear evidence of oxidation. This indicates that the chromium feedstock powders were likely slightly oxidized prior to cold-spray application. Information provided by Westinghouse aligns with this observation, with Westinghouse stating that the feedstock powders are entrained in the hot helium with a low amount of oxygen impurities, but it is possible that the powders can oxidize slightly immediately prior to deposition.

Microcrack features and microporosity were also observed in the CS Cr-coating, which could promote oxide formation in these spaces. Nitrogen carrier CS coatings have exhibited higher porous structures and deformation in comparison to their helium counterparts. Alakiozidis et al. observed large pores and lateral cracks in the SEM imaging of their CS variants (I. Alakiozidis et al. 2025). Lateral cracks typically followed deposit boundaries, which were also observed in the CS Cr-coatings in this work. When hydrides within the material are sufficiently large, cracks can begin and propagate in the alloy (S. Di et al. 2015). The zircaloy itself has also shown surface oxidation. At locations of severe substrate deformation, the native oxide detached from the surface of the zircaloy, which could form needle-like structures that can initiate crack formation.

The polished CS Cr-coated materials showed very different results in OM – with the out-of-core materials showing long hydrides distributed within the substate, and the in-core sample showing only short, small hydrides visible at higher magnifications, Figure 3.72.

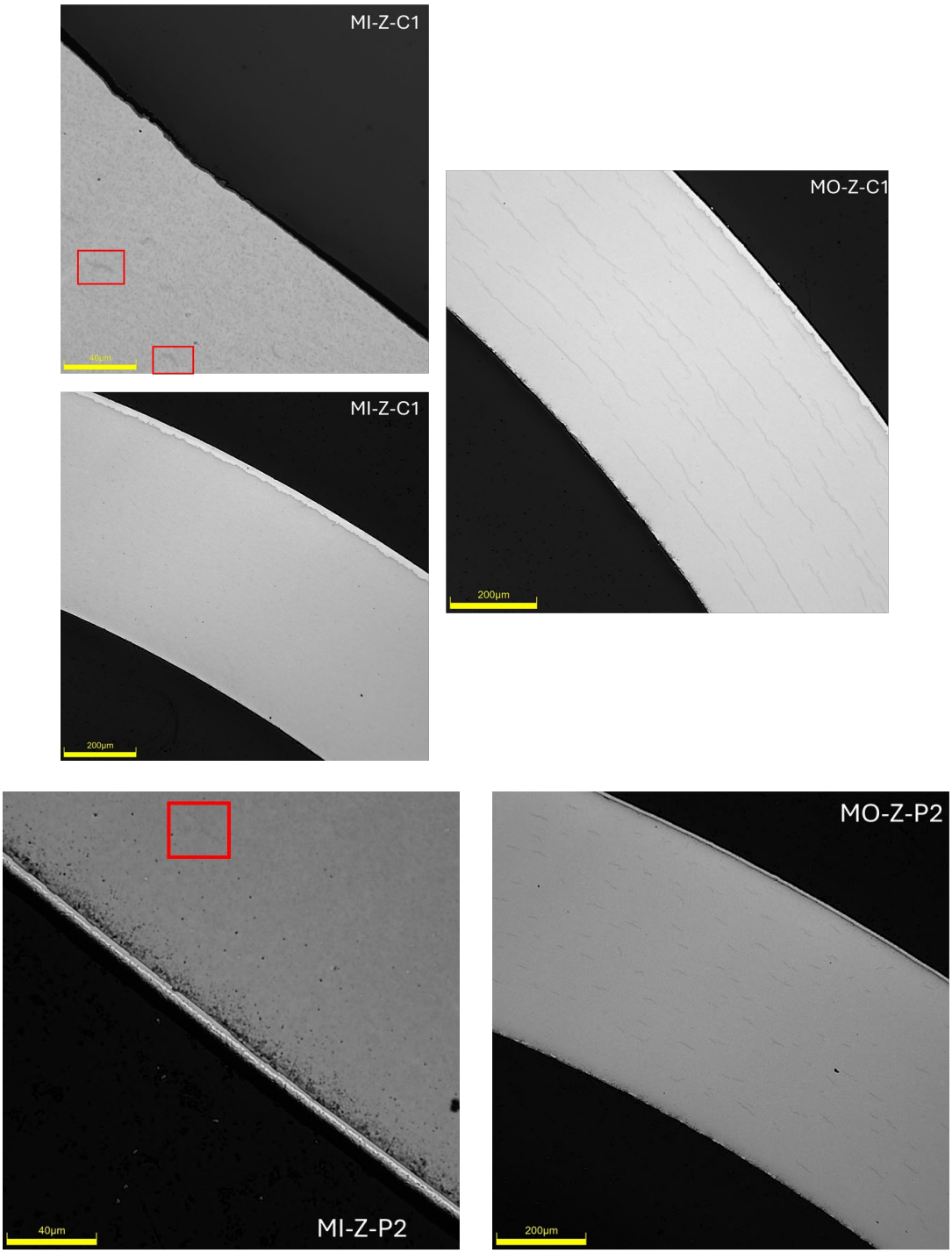

Figure 3.72. A comparison of OM images of in-core (MI samples) and out-of-core (MO samples) CS Cr-coated zircaloy (top -C samples) and PVD Cr-coated zircaloy (bottom -P samples).

PVD Coated Samples: Converse to the visual observation of the CS deposition samples, the PVD Cr-coated variants (both 5 µm and 10 µm coating thickness) exhibited straw/gold-colored samples from the out-of-core experiment loop, and blue/purple-colored samples from the in-core experiments.

Through SEM analysis, the Cr-coated PVD variants showed the columnar grain boundaries and structure expected from the deposition process as observed with the chromium grains lined perpendicular to the zircaloy surface. The grain structure was non-uniform throughout the Cr-coating and exhibited extensive crack networks, pores, and large voids. Zirconium particles were noted in the Cr-coating itself, which were likely introduced in the deposition process. It was observed that the coating deposition process may have occurred in two stages due to the change in grain morphology from the columnar grains observed at the coating/substrate interface versus the coarser grains near the outer diameter. Many voids, cracks, and defects were observed in this region of the coating.

Observations of the polished OM results showed similar trends between the PVD and CS variants of the out-of-core and in-core materials. In particular, the out-of-core samples visually displayed higher volumes of hydrides than the in-core counterpart, Figure 3.72. The in-core samples had hydrides present in the sample but these were only visible at higher magnifications, appeared much shorter, smaller and in fewer numbers in comparison to the out-of-core samples, where the hydrides were readily visible at lower magnifications.

It is counterintuitive that the hydrides were visually more prominent and of higher concentration in the out-of-core samples than the in-core samples. Typically, the presence of irradiation enhances hydrogen pickup due to radiolysis products and increased corrosion at the cladding waterside interface. To corroborate the visual hydride observations, bulk hydrogen measurements were completed via inert gas fusions analysis using a LECO analyzer. These hydrogen measurements are an indication of total hydrogen content throughout the entire sample (substrate and coating), as opposed to a single region.

Table 3.10. Bulk hydrogen concentration of select samples from inert gas fusion analysis.

Sample	Hydrogen wppm	Average Hydrogen Concentration wppm
MI-Z-C1-1 S1 in-core CS Cr-coated	19	19
MI-Z-C1-1 S2 in-core CS Cr-coated	20	
MO-Z-C1-1 S1 out-of-core CS Cr-coated	103	101
MO-Z-C1-1 S2 out-of-core CS Cr-coated	99	
MI-Z-U1-1 S1 in-core uncoated	20	--
MO-Z-U1-1 S1 out-of-core uncoated	12	--

Bulk hydrogen concentration measurements from the LECO analyzer show hydrogen concentrations in the uncoated (in-core and out-of-core) samples were comparable to the in-core CS Cr-coated variant tested. However, the out-of-core sample, which exhibited easily observed and identifiable hydrides on the polished OM images, had a greatly increased hydrogen content in comparison. This bulk hydrogen content aligns with expectations from these observations. While the PVD variants were not analyzed using this method, it is logical, from the visual analysis, that similar trends would be observed in the out-of-core versus in-core samples.

There are two hypotheses proposed to explain the apparent discrepancy in hydrogen pickup in-core compared to out-of-core. The first is that very slight temperature differences between the two conditions affect the oxide formation, which in turn affects the hydrogen diffusion into a sample. The second is that radiation can affect precipitates, such as hydrides, and inhibit or

delay their formation and growth. While there is not conclusive evidence with the current data, both hypotheses will be discussed.

First, under normal LWR conditions with fueled rods, the most prevalent hydrogen source for hydride formation is from waterside corrosion that occurs at the outer diameter of a fuel rod in reactor conditions (A. Couet et al. 2014; A.T. Motta et al. 2015). As the metal reacts with water and oxidizes, hydrogen is generated at the metal/water interface and some fraction is taken up in the metal. Once the solubility of hydrogen is exceeded, which is highly temperature dependent, hydrides will precipitate. In MITR, the source of hydrogen is the 50 cc/kg as part of the water chemistry. Factors within the reactor such as coolant flow, coolant chemistry, fast neutron flux, and cladding hydrogen content can increase the impact that temperature plays on corrosion. Temperature gradients during reactor operations impact hydride formation due to their temperature dependence (J.J. Kearns 1967; A.T. Motta et al. 2019; C.E. Ells 1968).

In a typical PWR, coolant enters the reactor core at 287°C to 291°C and exits at 326°C to 329°C (EPRI 1992). More importantly, the fissions within the fuel increase the surface temperature of the cladding for a typical 17×17 assembly to between 294°C and 345°C (NRC 2017). Increased temperature within a reactor core results in greater oxidation of the cladding outer diameter, and in turn, increased hydrogen pickup and higher hydrogen concentrations. PNNL has shown that for uncoated rods, the oxide layer and hydrogen concentrations increase steadily moving from the cooler bottom of the rod to the hotter top of the rod (R.W. Shimskey et al. 2022b; R.W. Shimskey et al. 2022a). These increased temperature areas keep hydrogen in solution due to the higher solubility. Alternatively, cooler regions with lower solubility typically exhibit more hydrides as the lower solubility of hydrogen causes it to reach saturation and precipitate. A fuel rod is sealed so no corrosion occurs at the inner diameter. Hydrogen diffuses from the outer diameter where it is generated and picked up by the metal towards the inner diameter because of the concentration gradient. However, the inner diameter is much hotter because of the heat generated from the fuel. Hydrides precipitate in the cooler regions which explains the typical hydride rim near the outer diameter in uncoated fuel rod.

The MITR has temperatures of only 296°C to 298°C and the samples are open, thus both the inner and outer diameters are at the same temperature. As there is no or minimal temperature gradient across the sample wall thickness, hydrogen diffusion will be driven mainly by a concentration gradient. As presented, samples that did exhibit hydrides were closer to the outer diameter and then moving through the wall thickness. Even when hydrides were found near the inner diameter, they typically appeared smaller and lower in concentration than elsewhere in the cladding. This strongly suggests that the bulk of hydrogen pickup was at the outer diameter and diffused inward, with or without a coating.

To understand the observations of hydrides in out-of-core samples but minimal hydrides in the in-core samples, the characteristics of the metals (Zr and Cr) and their oxides need to be considered. Hydrogen diffusion is orders of magnitude faster in metals than in oxides (D. Khatamian 1997; K.W. Kehr 1978; A.T. Motta et al. 2019). Zr will oxidize much faster than Cr in water at approximately 300°C. Thus, it would be expected that the inner diameter, which is Zr, will oxidize faster than Cr coated outer diameter. Not enough data was collected to conclusively state that the inner diameter was oxidized enough to reduce hydrogen uptake, but the evidence presented in Figure 3.51, Figure 3.52, and Figure 3.60 indeed show Zr oxidizing faster than Cr. Further, the much smaller presence of hydrides at the inner diameter provides additional evidence. For uncoated samples, the outer diameter, which is Zr, would also oxidize relatively quickly and reduce total hydrogen uptake relative to the Cr-coated samples, where the Cr oxidizes slower under the same conditions.

The biggest question remaining is why the out-of-core samples exhibited more hydrogen uptake and hydride formation than the in-core samples. It can be proposed that the temperature gradient documented in the MITR may have been more variable than anticipated. Temperature in the MITR is primarily managed via resistive heaters located outside the reactor vessel controlled by thermocouples located in the flow just above the core region – near the out-of-core samples. Due to the relatively low in-core mass of the MITR facility, the in-core heating is noted as relatively small. However, at the temperatures the samples were subjected to for this experiment, small temperature variations could result in significant oxidation and hydrogen uptake differences. It is possible that gamma heating slightly increased the temperature of the samples in-core, allowing faster oxidation of both the inner and outer diameters (Zr and Cr), which would reduce hydrogen diffusion to the base metal. In the case of the CS Cr-coated in-core sample, a more substantial oxide layer was identified on the inner diameter of the cladding, while the equivalent out-of-core sample does not exhibit this oxide layer. It is important to note that Cr is used as the protective coating, but in reality, it is the formation of the oxide, just as with stainless steels, that is the true protective layer. Further examination of samples to locate and quantify oxide layer thicknesses at both the inner and outer diameters would be necessary to validate this first hypothesis.

The second hypothesis is that radiation affects precipitates, such as hydrides, and inhibits or delays their formation and growth. Radiation and radiolysis processes within a reactor core also have a large impact on cladding. Two key irradiation processes can occur within an alloy containing precipitates; enhanced diffusion or destruction of precipitates (R.S. Nelson et al. 1972). In the case of hydride precipitates, the radiation from the reactor core could partly re-dissolve the hydrides existing in the substrate, delaying the precipitation of hydrogen and impeding hydride growth. In the out-of-core sample, this radiation effect would not be present, hence generating hydrides at a faster rate than the in-core samples.

The total hydrogen concentration in a sample, which includes the Zr substrate, the Cr coating, and oxide layers, was measured using LECO analysis and the results are presented in Table 3.10. It is clear that the total hydrogen, both soluble and precipitated as hydrides, is minimal for in-core samples that were uncoated and with CS Cr coating. The uncoated out-of-core sample also had minimal total hydrogen. The out-of-core CS Cr-coated samples had substantially more total hydrogen, which is observed as hydrides because of the low solubility at the cool temperatures. Radiation inhibiting the formation of hydrides would not have an effect on the total hydrogen in a sample; the radiation would have to inhibit the uptake of hydrogen. This would not seem reasonable given the uptake of hydrogen observed in LWR fuel rods. However, additional data is necessary to validate or disprove this hypothesis.

4.0 INL – Methods, Results, and Discussion

High-resolution microstructural characterization of as-fabricated, out-of-core, and in-core Cr-coated Optimized ZIRLO™ cladding samples was performed at the Critical Materials Energy System and Innovation Center (CMESIC) and the Irradiated Materials Characterization Laboratory (IMCL) at Idaho National Laboratory (INL). Characterization activities included optical microscopy (OM), scanning electron microscopy with energy dispersive X-ray spectroscopy (SEM/EDS), transmission electron microscopy (TEM), and atom probe tomography (APT). The reference (as-fabricated) cold spray (CS) Cr-coated specimen (R-Z-C1), one out-of-core sample (MO-Z-C1-2), and one in-core sample (MI-Z-C1-2) — both CS Cr-coated — were examined. The analytical approach progressed from low-resolution overview characterization to high-resolution interface and defect analysis, enabling a systematic assessment of coating integrity, phase composition, and microstructural evolution as a function of exposure condition.

4.1 Sample Preparation and Optical Microscopy

Irradiated samples were prepared for metallographic examination at the IMCL. Each specimen was cut to a nominal ring cross section, mounted in an epoxy met-mount with the surface of interest exposed, and allowed to cure overnight. Grinding and polishing were performed on an Allied High Tech Products MetPrep™ grinding and polishing machine equipped with a PH-3™ power head. The specimen surface was first ground flat using a 30 µm diamond pad, followed by progressively finer grinding and polishing steps. The final surface finish was achieved using an OPS (colloidal silica suspension) step modified with 30% H_2O_2 in a 4:1 OPS-to-H_2O_2 ratio for 5 minutes. For irradiated samples, the standard 1 µm polishing step was intentionally omitted to preserve and enhance contrast of hydride microstructures. The complete polishing procedure is summarized in Table 4.1. Following polishing, all samples were maintained in a nitrogen-purged environment prior to transfer to subsequent characterization steps to minimize surface re-oxidation.

Table 4.1.Metallographic grinding and polishing procedure used at INL-IMCL.

Step	Duration	Notes
30 µm diamond pad – grind to flat	1 minute	—
9 µm diamond pad	2 minutes	—
9 µm diamond suspension solution	5 minutes	—
3 µm diamond suspension solution	8 minutes	—
1 µm polishing step	Omitted	Omitted for irradiated samples to preserve hydride contrast
4:1 OPS–H_2O_2 (30%) vibratory polish	5 minutes	Final finish step

Optical microscopy was performed on all polished cross sections prior to electron microscopy to provide an overview of coating integrity and to identify regions of interest for higher-resolution analysis. Low-magnification images captured the full cladding cross section, while higher-magnification images were used to assess coating thickness and to screen for hydride microstructures and coating defects. Optical images of the as-fabricated (R-Z-C1), out-of-core (MO-Z-C1-2), and in-core (MI-Z-C1-2) cross sections are shown in Figure 4.1, Figure 4.2, and Figure 4.3, respectively. Optical measurements confirmed the presence of intact Cr coatings in

all samples, with measured thicknesses of 25 ± 8 µm. No coating delamination or macro-scale cracking was observed at the optical scale in the as-fabricated reference material. Notably, the out-of-core sample (MO-Z-C1-2) exhibited wavy, needle-like microstructural features in the Zr alloy substrate characteristic of zirconium hydrides (ZrH), whereas the in-core sample (MI-Z-C1-2) showed markedly fewer such features, suggesting differences in hydride density or morphology between the two exposure conditions that warranted further high-resolution investigation.

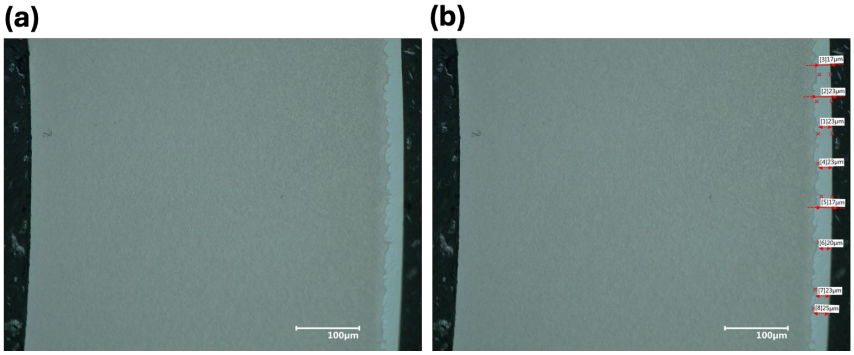

Figure 4.1. Optical microscopy images of the as-fabricated cold spray Cr-coated reference sample (R-Z-C1) showing 500X-magnification image of the Cr coating with measured thickness indicated.

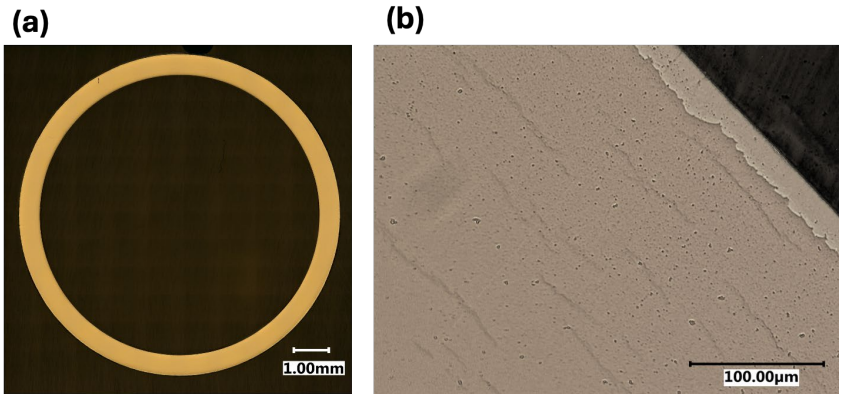

Figure 4.2. Optical microscopy images of the out-of-core cold spray Cr-coated sample (MO-Z-C1-2): (a) full cross section at 200X and (b) 1000X image showing wavy, needle-like microstructural features in the Zr alloy substrate consistent with zirconium hydrides (ZrH).

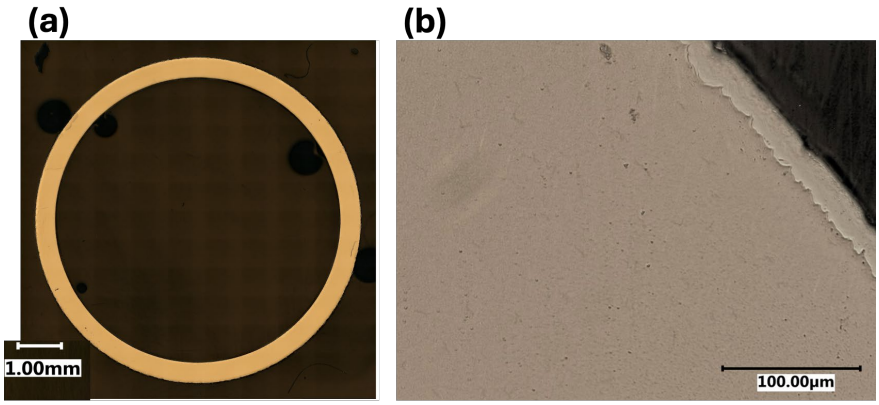

Figure 4.3. Optical microscopy images of the in-core cold spray Cr-coated sample (MI-Z-C1-2): (a) at a full cross section 200X and (b) 1000× showing the Cr coating and Zr alloy substrate. Hydride-like features are substantially less prominent relative to the out-of-core sample (MO-Z-C1-2).

4.2 As-Fabricated Cr-Coated Cladding

The as-fabricated Cr-coated Optimized ZIRLO™ reference sample R-Z-C1 (cold spray coating, nominal thickness ~25 µm) was examined at INL to establish baseline microstructural and compositional characteristics. This reference material provides the essential context against which microstructural and compositional changes induced by aqueous corrosion and neutron irradiation in the exposed samples are interpreted.

4.2.1 Cold Spray Cr-Coated Reference Material (R-Z-C1)

4.2.1.1 SEM Characterization

Surface and cross-sectional imaging of R-Z-C1 was performed using a FEI Quanta dual-beam SEM/FIB instrument at CMESIC. Images were collected at multiple length scales to characterize both the Cr coating morphology and its interface with the Zr alloy substrate. SEM micrographs confirmed the presence of a continuous, adherent Cr coating on the Zr alloy outer surface (Figure 4.4a). At higher magnification, the CS Cr coating exhibited a characteristic 'splat' microstructure with a small but detectable amount of intrasplat microporosity and isolated micro-crack-like features, consistent with the high-velocity solid-particle impact mechanics of the CS deposition process. Sites selected for TEM lamella and APT specimen preparation are indicated in Figure 4.4b.

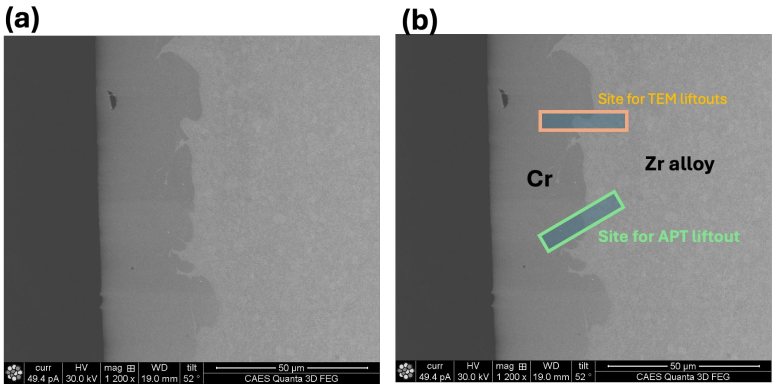

Figure 4.4. SEM micrographs of as-fabricated cold spray Cr-coated sample R-Z-C1: (a) overview image confirming a continuous, adherent Cr coating on the Zr alloy substrate, showing intrasplat microporosity and micro-crack-like features characteristic of the CS deposition process; (b) image with sites marked for TEM lamella lift-out and APT specimen preparation.

4.2.1.2 TEM Analysis

TEM lamellae were prepared from two regions of R-Z-C1 using the in-situ FIB lift-out technique on the FEI Quanta dual-beam instrument. A 1–1.5 µm thick Pt protective layer was deposited over each region of interest prior to milling. Sequential FIB milling reduced each lamella to an electron-transparent thickness of approximately 100 nm. Two lamellae were prepared: one from within the Cr coating interior and one spanning the Cr/Zr alloy interface. TEM analysis was carried out using the Spectra instrument located in CMESIC.

The Cr coating interior of R-Z-C1 exhibited equiaxed grains with a bimodal grain size distribution (Figure 4.5). Localized regions of ultrafine, nano-scale grains were observed at splat boundaries, consistent with severe plastic deformation and potential dynamic recrystallization during the CS process. HAADF STEM imaging and STEM-EDS mapping of the coating interior confirmed a predominantly Cr composition with a minor oxygen contribution at splat boundaries (Figure 4.6), suggesting trace oxidation of the Cr feedstock powder surface prior to deposition — an observation consistent with APT findings described in Section 4.2.1.3 and supporting the interpretation that intrasplat spaces contain minor Cr oxide. Bright-field TEM imaging revealed linear contrast features within the Cr coating near the Zr interface, tentatively identified as twins or shear bands arising from the CS deposition process. Additionally, a high dislocation density was observed within larger Cr grains, with clearly resolvable sub-grain boundaries, indicative of significant work hardening inherent to the CS process.

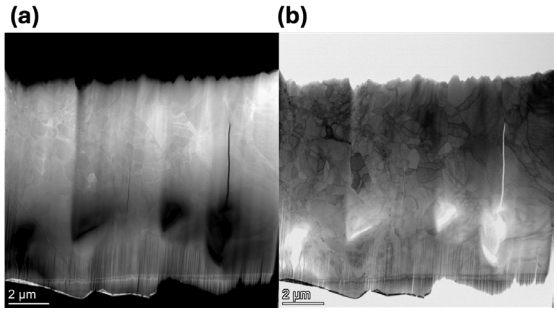

Figure 4.5. TEM analysis of the Cr coating interior in as-fabricated cold spray sample R-Z-C1: (a) HAADF-STEM image and (b) bright-field TEM image showing equiaxed grains with a bimodal size distribution — large grains interspersed with nano-grained regions at splat boundaries. Sub-grain boundaries (blue arrows) and regions of elevated dislocation density (yellow arrows) are indicated.

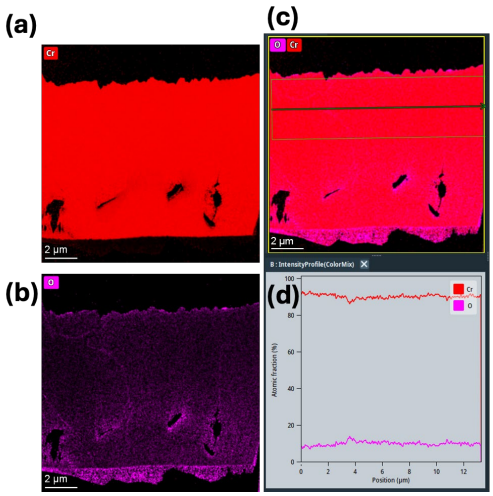

Figure 4.6. STEM-EDS analysis of the Cr coating interior in as-fabricated cold spray sample R-Z-C1: (a) Cr elemental map and (b) O elemental map showing minor oxygen enrichment at splat boundaries; (c–d) EDS line profiles taken along the length of the TEM lamella.

The TEM lamella spanning the Cr/Zr alloy interface revealed a wavy interface morphology consistent with the mechanical interlocking characteristic of CS coatings (Figure 4.7–Figure 4.10). No continuous $ZrCr_2$ intermetallic layer was identified at the interface. One-dimensional EDS line profiles taken perpendicular to the interface showed a sharp, step-like compositional transition from the Cr coating to the Zr alloy substrate with no detectable Cr diffusion into the Zr alloy, confirming the absence of significant interdiffusion in the as-fabricated condition (Figure 4.9). Sub-micron precipitates enriched in Nb and Fe were observed distributed within the Zr alloy region close to the interface (Figure 4.11), consistent with the known β-Nb and $Zr(Fe,Cr)_2$ second-phase particle composition of Optimized ZIRLO™. A Cr–O signal was detected at the interface in the EDS maps (Figure 4.9), indicating trace oxide formation at this location — an observation corroborated by APT reconstructions described in Section 4.2.1.3.

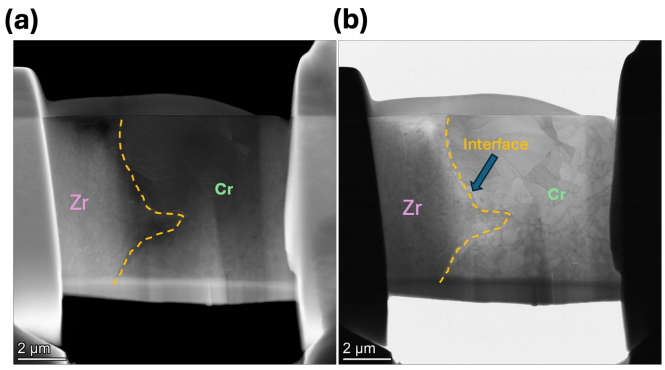

Figure 4.7. TEM analysis of the Cr coating and Zr alloy interface in as-fabricated cold spray sample R-Z-C1: (a) HAADF-STEM image and (b) bright-field TEM image with the Cr/Zr interface indicated. Nano-sized grains are visible in the Cr region proximal to the interface.

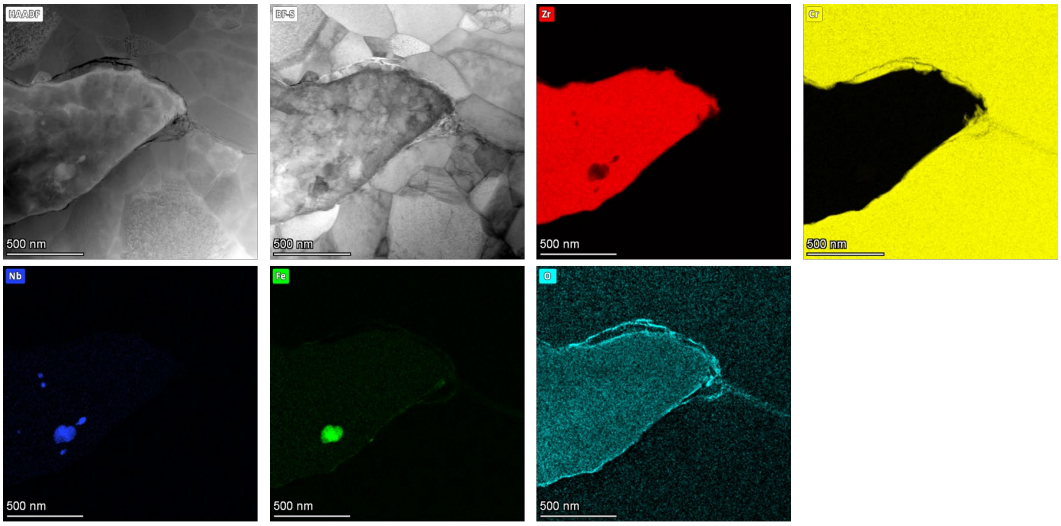

Figure 4.8. STEM-EDS elemental maps of the Cr/Zr alloy interface in as-fabricated cold spray sample R-Z-C1, showing the spatial distribution of Zr, Cr, Nb, Fe, and O across the interface region.

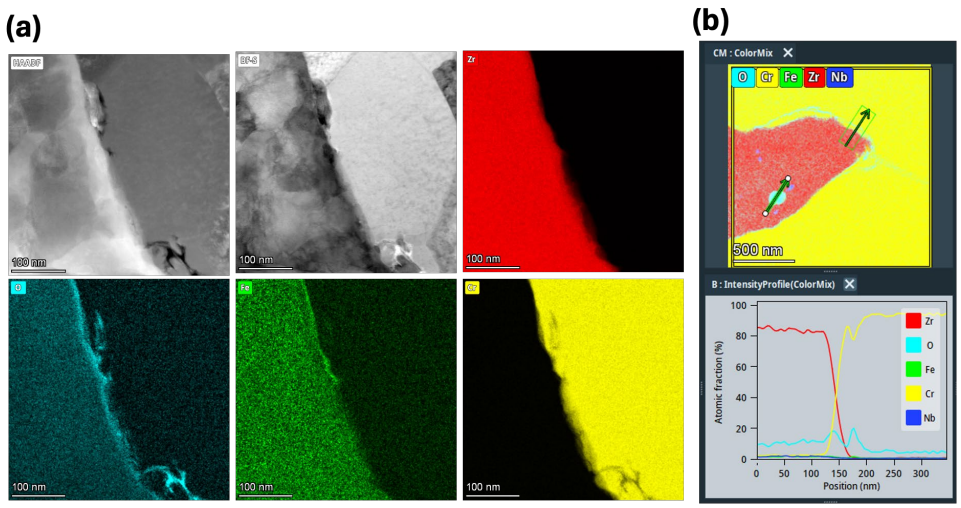

Figure 4.9. STEM-EDS analysis of the Cr/Zr alloy interface in as-fabricated cold spray sample R-Z-C1: (a) elemental maps showing the distribution of Zr, Cr, Nb, Fe, and O; (b) one-dimensional EDS line profile taken perpendicular to the interface, confirming a sharp, step-like compositional transition and the absence of an intermediate $ZrCr_2$ intermetallic layer.

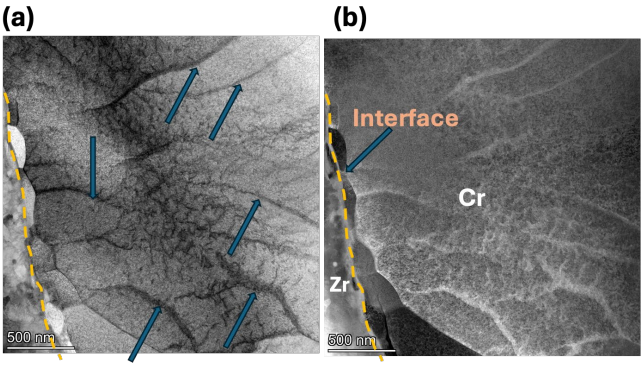

Figure 4.10. Higher-magnification STEM images at the Cr coating and Zr alloy interface of as-fabricated cold spray sample R-Z-C1: (a) bright-field and (b) HAADF images showing small grains with grain boundaries oriented perpendicular to the Cr/Zr interface, a high density of low-angle grain boundaries and sub-grain boundaries (arrows), and dislocations within the Cr coating interior.

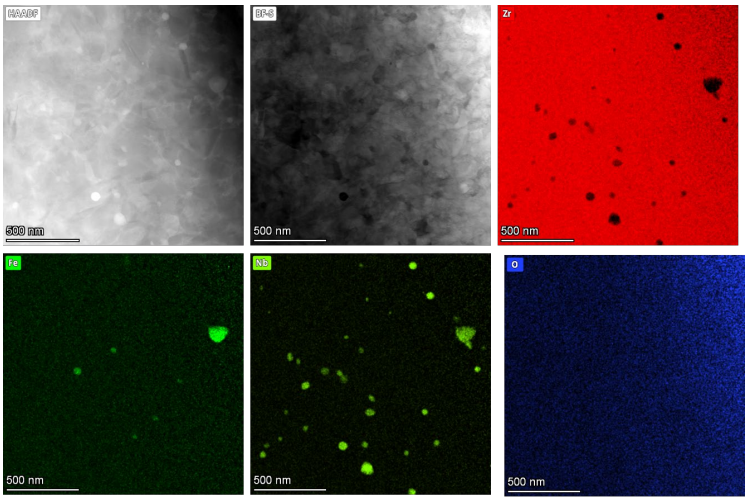

Figure 4.11. Low-magnification STEM-EDS elemental maps of the Zr alloy region in as-fabricated cold spray sample R-Z-C1, showing a high number density of sub-micron precipitates enriched in Fe and Nb, consistent with β-Nb and $Zr(Fe,Cr)_2$ second-phase particles characteristic of Optimized ZIRLO™.

4.2.1.3 APT Analysis

Atom probe tomography was performed to characterize the nanoscale chemistry of the Cr coating interior, the Cr/Zr alloy interface, and the Zr alloy substrate. Specimens were prepared by FIB lift-out from targeted regions within each layer and across the interface.

A specimen prepared from the Cr coating interior, approximately 1–2 µm from the Cr/Zr interface, revealed a composition of approximately 99.9 at.% Cr with trace-level impurities of Fe, Mn, Si, O, and P (Figure 4.12). This confirms the high purity of the CS Cr coating in the as-fabricated condition. A grain boundary was captured in this reconstruction; the one-dimensional compositional profile across the boundary showed a minor depletion in Fe but no significant enrichment of other species, suggesting limited chemical segregation at this particular boundary.

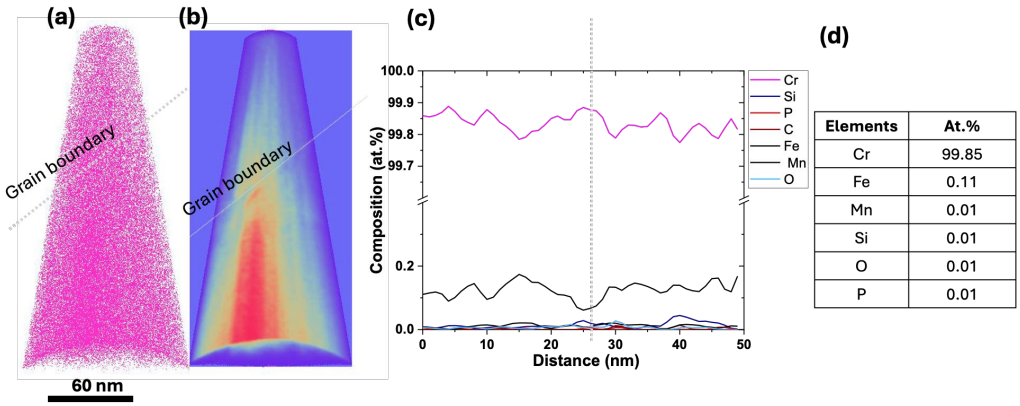

Elements	At.%
Cr	99.85
Fe	0.11
Mn	0.01
Si	0.01
O	0.01
P	0.01

Figure 4.12. APT analysis of the Cr coating interior in as-fabricated cold spray sample R-Z-C1 (specimen prepared ~1–2 µm from the Cr/Zr interface): (a) three-dimensional Cr atom map; (b) two-dimensional contour map highlighting the captured grain boundary; (c) one-dimensional compositional profile taken across the grain boundary showing minor Fe depletion; (d) measured bulk composition table of the specimen.

A second APT specimen targeted a grain boundary to investigate boundary chemistry in greater detail (Figure 4.13). This reconstruction captured a grain boundary exhibiting clear Cr oxide segregation, as evidenced by an elevated O signal at the grain boundary plane in the one-dimensional compositional profile. This boundary also showed slight Fe enrichment, in contrast to the Fe depletion observed at the first boundary. The variability in grain boundary chemistry between the two specimens is consistent with differences in grain boundary character (low-angle versus high-angle) and with local oxidation state variations introduced during the CS deposition process.

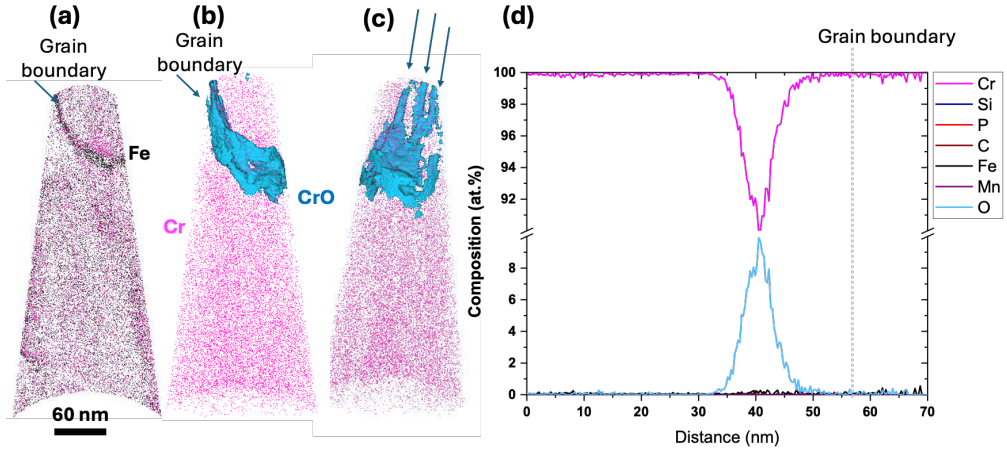

Figure 4.13. APT analysis of a grain boundary in the Cr coating of as-fabricated cold spray sample R-Z-C1 (specimen prepared ~4 µm from the Cr/Zr interface): (a) three-dimensional atom map with Fe-decorated grain boundary highlighted; (b) iso-concentration surface showing Cr oxide segregation at the boundary; (c) rotated view of the Cr oxide distribution; (d) one-dimensional compositional profile taken across the grain boundary confirming Cr oxide enrichment and slight Fe enrichment.

An APT specimen prepared from the Zr alloy region approximately 1 μm from the Cr/Zr interface revealed a uniform distribution of Zr, Sn, and Nb with no detectable Cr or Fe signal (Figure 4.14). The absence of Cr in this specimen, despite its proximity to the interface, confirms the lack of Cr diffusion into the Zr alloy substrate in the as-fabricated condition, consistent with TEM-EDS observations of a sharp compositional interface.

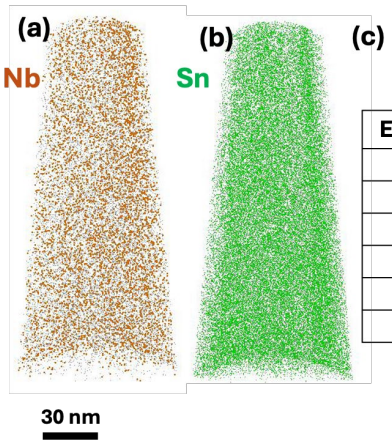

Elements	At.%
Zr	97.65
Nb	0.82
O	0.69
Sn	0.61
Fe	0.03
Si	0.01

Figure 4.14. APT analysis of the Zr alloy region in as-fabricated cold spray sample R-Z-C1 (specimen prepared ~1 μm from the Cr/Zr interface): three-dimensional atom maps showing a uniform distribution of (a) Nb and (b) Sn; (c) measured bulk composition table confirming the absence of detectable Cr or Fe, consistent with no interdiffusion in the as-fabricated state.

An additional APT specimen prepared from closer to the interface (~3–4 μm from the Cr/Zr boundary) captured Nb- and Fe-enriched second-phase precipitates within the Zr alloy (Figure 4.15). Iso-concentration surfaces highlight the precipitate morphology, and proximity histogram analysis across the precipitate/matrix interface confirms enrichment in Nb, Fe, Sn, and minor Cr relative to the surrounding Zr matrix, consistent with the composition of β-Nb and $Zr(Fe,Cr)_2$ particles known to be present in Optimized ZIRLO™. A grain boundary was also captured at the base of the reconstructed volume; the one-dimensional profile taken across it shows slight enrichment in Sn, Fe, and Nb at the boundary plane.

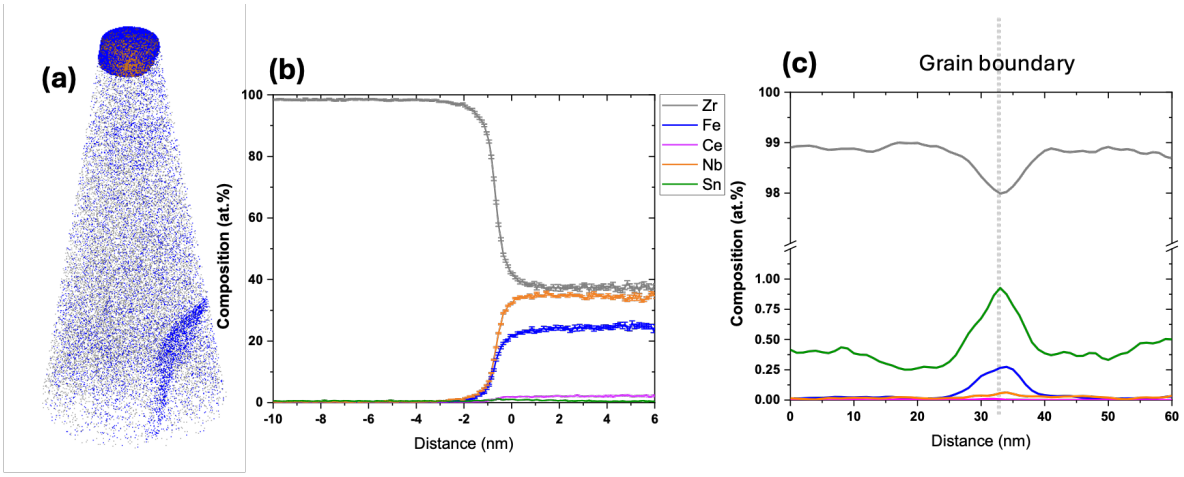

Figure 4.15. APT analysis of the Zr alloy region near the Cr/Zr interface in as-fabricated cold spray sample R-Z-C1 (specimen prepared ~3–4 µm from the interface): (a) atom map with iso-concentration surfaces highlighting Nb- and Fe-enriched precipitates; (b) proximity histogram taken across a precipitate confirming enrichment in Nb, Fe, Sn, and minor Cr relative to the Zr matrix; (c) one-dimensional compositional profile across a captured grain boundary showing slight Sn, Fe, and Nb enrichment at the boundary plane.

4.3 Radiological Material Analysis

Two irradiated CS Cr-coated Optimized ZIRLO™ samples were received at INL-IMCL for post-irradiation examination: one exposed to the MITR out-of-core water loop conditions (MO-Z-C1-2) and one irradiated in-core at the MITR to approximately 0.5 dpa (MI-Z-C1-2). Both specimens were exposed at 296–298 ± 1°C in PWR-simulated water chemistry, and carry a nominal Cr coating thickness of ~15–25 µm. Sample cutting, mounting, and metallographic preparation followed the procedure described in Section 4.1.

4.3.1 Out-of-Core Cold Spray Cr-Coated Sample (MO-Z-C1-2)

4.3.1.1 Optical Microscopy and SEM/EDS

The cross-sectional optical micrograph of MO-Z-C1-2 showed a cladding outer diameter of approximately 5 mm with an intact Cr coating of approximately 25 µm on the outer surface (Figure 4.2). Higher-magnification optical images revealed wavy, needle-like microstructural features distributed throughout the Zr alloy substrate, consistent with the morphology of zirconium hydrides. These features were widely distributed across the substrate cross section, indicating significant hydrogen uptake during the out-of-core aqueous exposure.

SEM imaging of MO-Z-C1-2 was performed using the FEI G4 instrument at IMCL. Secondary electron images at multiple length scales are shown in Figure 4.16. Low-magnification images confirmed the continuous Cr-coating on the outer surface with a few isolated porosity features. At intermediate magnification, elongated ZrH structures oriented approximately parallel to the Cr-coating surface were clearly resolved within the Zr alloy at approximately mid-wall locations. SEM imaging of the inner diameter surface revealed a thin ZrO_2 layer confirmed by EDS mapping (Figure 4.17), which showed an elevated O signal at the inner surface. ZrH structures were also identified near the inner diameter, indicating that hydrogen ingress occurred from both

the outer Cr-coated surface and the uncoated inner diameter surface, consistent with the open-tube specimen geometry used in the MITR experiment.

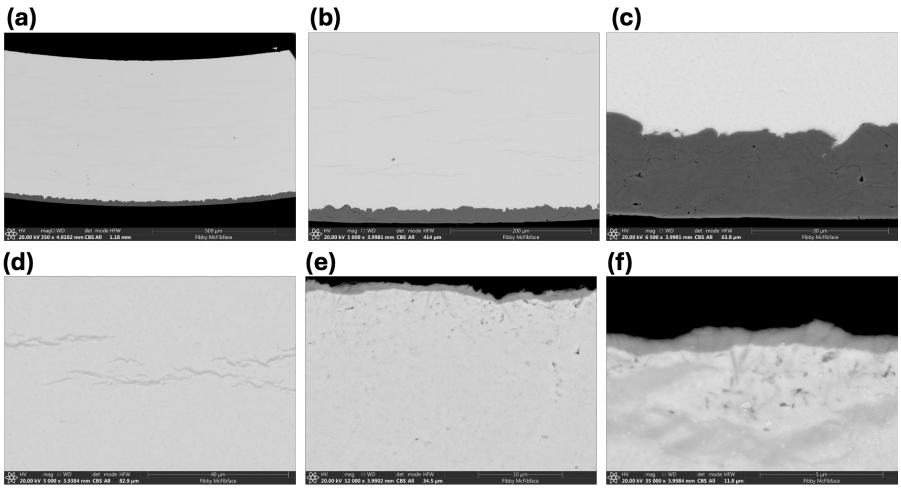

Figure 4.16. SEM analysis of out-of-core cold spray Cr-coated sample MO-Z-C1-2: (a-b) low-magnification secondary electron image of the full cross section; (c) showing Cr coating; (d) intermediate-magnification image showing elongated ZrH structures oriented parallel to the Cr coating at mid-wall locations; (e-f) inner-diameter region.

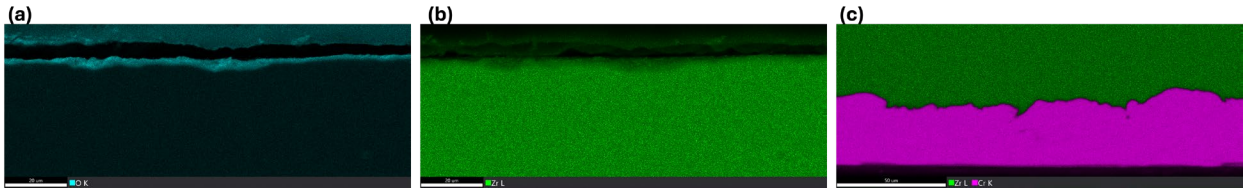

Figure 4.17. EDS elemental maps of the inner-diameter surface of out-of-core cold spray Cr-coated sample MO-Z-C1-2, showing the distribution of O, Zr, and Cr and confirming the presence of a ZrO_2 oxide layer at the inner diameter.

4.3.1.2 TEM Analysis (MO-Z-C1-3)

TEM analysis was performed on sample MO-Z-C1-3, a companion specimen from the same parent sample as MO-Z-C1-2, using a FEI Titan instrument. A TEM lamella was prepared by plasma FIB lift-out along the wavy ZrH features identified during SEM examination. Electron diffraction patterns collected from the Zr alloy region confirmed the presence of additional spots beyond those expected for the α-Zr hexagonal close-packed (HCP) matrix, attributable to the face-centered tetragonal (FCT) δ-$ZrH_{1.5-2}$ phase (Figure 4.18). Dislocation imaging was acquired using conventional two-beam bright-field TEM and weak-beam dark-field (WBDF) conditions to characterize the deformation substructure of the Zr alloy substrate. On-zone STEM imaging provided complementary dislocation contrast (Figure 4.19).

An additional TEM lamella was prepared from the Zr alloy tube interior to map second-phase precipitate distributions. STEM-EDS maps confirmed the presence of Nb-, Fe-, and Cr-enriched precipitates consistent with $Zr(Fe,Cr)_2$ and β-Nb particles (Figure 4.20).

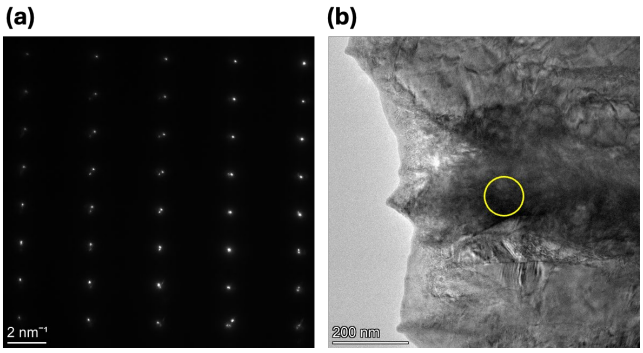

Figure 4.18. TEM analysis of the Zr alloy substrate in out-of-core sample MO-Z-C1-3: (a) bright-field TEM image with electron diffraction pattern confirming additional spots attributable to the δ-$ZrH_{1.5-2}$ phase; (b) two-beam bright-field and (c) weak-beam dark-field images revealing the dislocation substructure within the Zr alloy matrix.

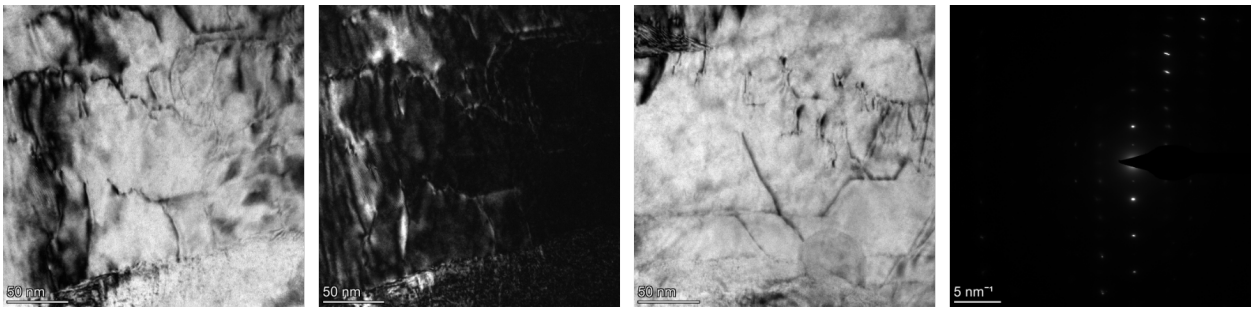

Figure 4.19. On-zone STEM image of the Zr alloy substrate in out-of-core sample MO-Z-C1-3, revealing the dislocation substructure including radiation-induced dislocation loops and line defects.

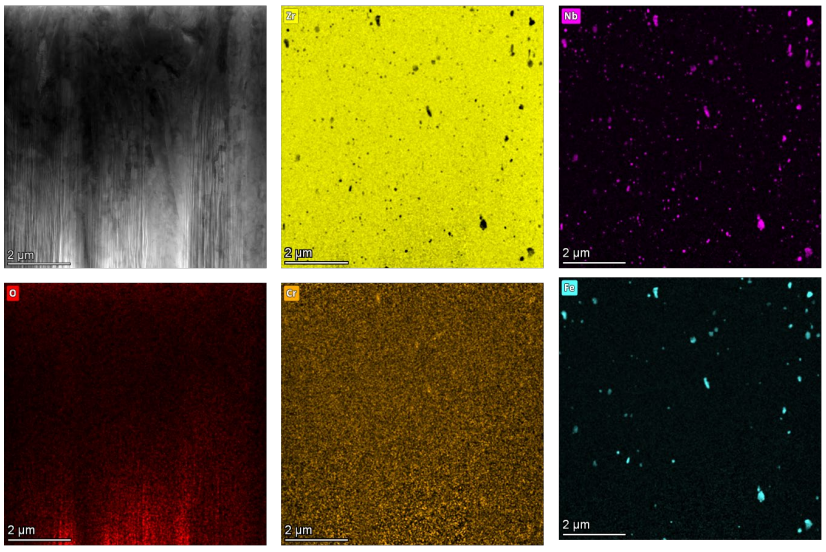

Figure 4.20. STEM-EDS elemental maps of the Zr alloy tube interior in out-of-core sample MO-Z-C1-3, confirming the presence and distribution of Nb-, Fe-, and Cr-enriched second-phase precipitates consistent with $Zr(Fe,Cr)_2$ and β-Nb particles.

4.3.1.3 APT Analysis (MO-Z-C2)

APT specimens were prepared from the Cr/Zr alloy interface region of MO-Z-C2, a companion out-of-core specimen, to elucidate compositional changes associated with aqueous exposure. A specimen prepared from the Cr coating region, approximately 2–4 µm from the Cr/Zr interface, showed a uniform Cr distribution with Fe impurities broadly comparable to the as-fabricated reference (Figure 4.21), with no significant bulk compositional change attributable to aqueous exposure at this distance from the interface.

Within the Zr alloy region, a high density of near-spherical Nb- and Fe-enriched second-phase particles was observed (Figure 4.22). A specimen prepared from the ZrH region further revealed Nb- and Fe-enriched precipitates; iso-concentration surfaces and proximity histograms confirmed the precipitate composition and highlighted Fe segregation at the precipitate/matrix interface (Figure 4.23). Quantitative comparison of precipitate composition, number density, and size distribution relative to the as-fabricated reference is ongoing.

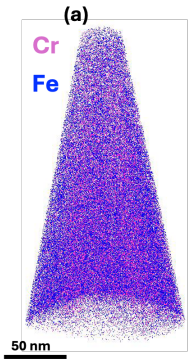

(b)

Elements	At.%
Cr	99.85
Fe	0.07
V	0.05
Mn	0.01
O	0.01
Si	0.01

Figure 4.21. APT analysis of the Cr coating region in out-of-core cold spray Cr-coated sample MO-Z-C2 (specimen prepared ~2–4 µm from the Cr/Zr interface): (a) three-dimensional Cr atom map showing a uniform distribution; (b) measured bulk composition.

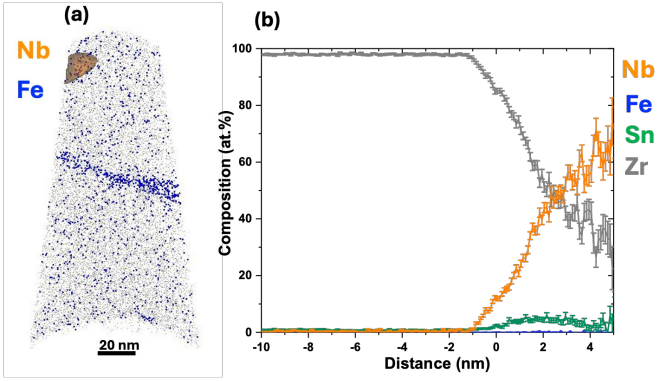

Figure 4.22. APT analysis of the Zr alloy region in out-of-core cold spray Cr-coated sample MO-Z-C2: (a) three-dimensional atom map highlighting Nb-enriched precipitates; (b) proximity histogram taken across an Nb-enriched precipitate.

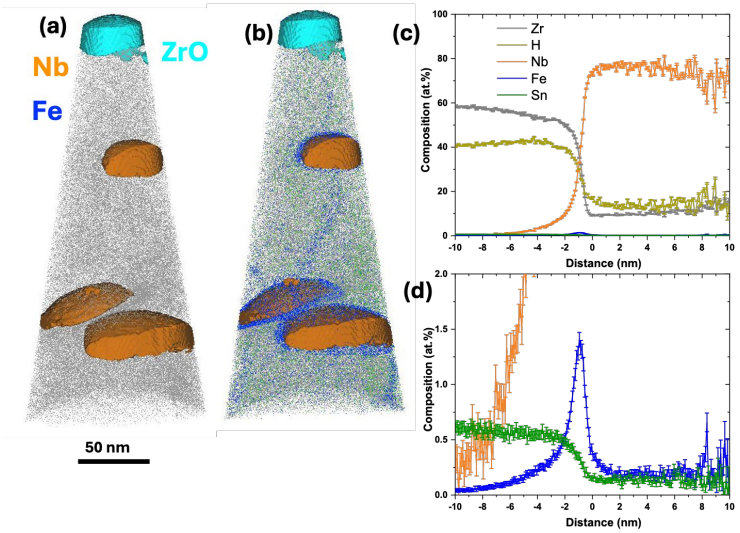

Figure 4.23. APT analysis of the ZrH region in out-of-core cold spray Cr-coated sample MO-Z-C2: (a–b) iso-concentration surfaces for ZrO, Nb, and Fe; (c–d) proximity histograms taken across Nb-enriched precipitates confirming Fe segregation at the precipitate/matrix interface.

4.3.2 In-Core Cold Spray Cr-Coated Sample (MI-Z-C1-2)

4.3.2.1 Optical Microscopy and SEM/EDS

Sample MI-Z-C1-2, irradiated in-core at the MITR to approximately 0.5 dpa at 298 ± 1°C, was examined following the same preparation and characterization sequence used for MO-Z-C1-2. Optical micrographs of the cross section (Figure 4.3) confirmed an intact Cr coating on the Zr alloy outer surface. In direct comparison to the out-of-core sample MO-Z-C1-2, the in-core sample exhibited substantially fewer wavy ZrH features at the optical scale. This is consistent with a reduced volumetric hydride fraction and may reflect suppression of hydride precipitation under irradiation conditions, potentially through irradiation-enhanced hydrogen solubility or irradiation-induced hydride dissolution.

SEM imaging of MI-Z-C1-2 at multiple length scales confirmed an intact Cr coating with isolated crack features visible at higher magnification (Figure 4.24). The elongated ZrH structures parallel to the coating surface that were prominently observed in MO-Z-C1-2 were largely absent at this imaging scale, consistent with either a lower volumetric hydride fraction, smaller hydride dimensions below the SEM resolution limit, or a preferred hydride orientation perpendicular to the polished cross section. EDS mapping confirmed the presence of a thin ZrO_2 layer at the inner diameter with an estimated thickness of 1–3 µm (Figure 4.25).

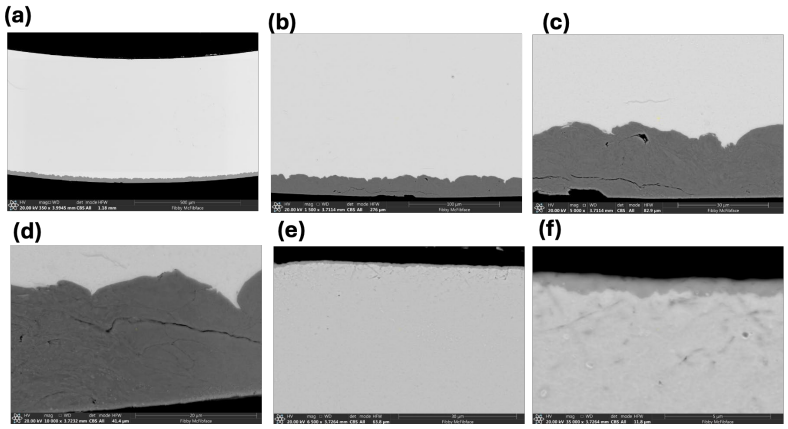

Figure 4.24. SEM analysis of in-core cold spray Cr-coated sample MI-Z-C1-2: (a) low-magnification secondary electron image of the full cross section; (b–d) higher-magnification images showing the intact Cr coating with isolated crack features; (e) the absence of prominent parallel ZrH structures observed in the out-of-core sample (f) inner-diameter region.

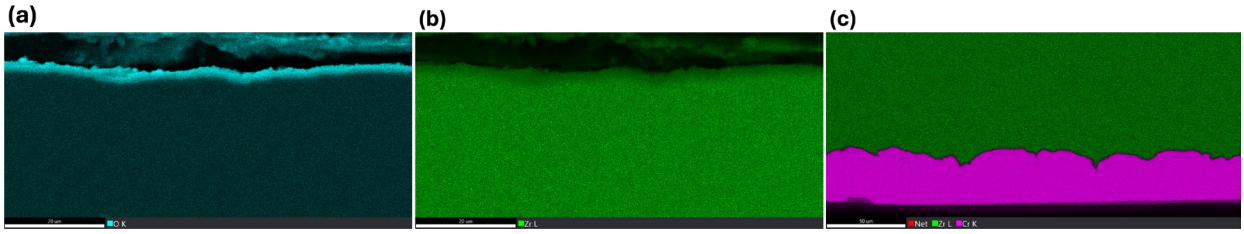

Figure 4.25. EDS elemental maps of the inner-diameter surface of in-core cold spray Cr-coated sample MI-Z-C1-2, confirming the presence of a ZrO_2 oxide layer with an estimated thickness of 1–3 μm.

4.3.2.2 TEM Analysis

A TEM lamella was extracted from the Cr/Zr alloy interface region of MI-Z-C1-2 by plasma FIB lift-out. STEM-EDS mapping resolved the Cr coating and Zr alloy substrate, with Nb- and Fe-enriched second-phase precipitates in the Zr alloy and Cr-O enrichment along crack features in the Cr coating proximal to the interface (Figure 4.26). A minor Zr signal was detected along cracks within the Cr coating near the interface; the origin of this signal requires further investigation. One-dimensional EDS profiles perpendicular to the Cr/Zr interface confirmed a sharp, step-like compositional transition with no detectable $ZrCr_2$ intermetallic layer, consistent with the as-fabricated reference and the out-of-core sample.

Electron diffraction collected from the Zr alloy region of the in-core lamella did not exhibit the additional spots associated with the δ-ZrH phase that were observed in the out-of-core sample MO-Z-C1-3, providing direct crystallographic evidence of a lower bulk ZrH phase fraction in the in-core sample under the conditions studied.

Two-beam bright-field TEM and on-zone STEM imaging were used to characterize the radiation damage substructure within the Zr alloy substrate (Figure 4.27). Radiation-induced dislocation loops and line defects were observed, consistent with approximately 0.5 dpa displacement damage. Diffraction imaging of the Cr coating revealed an elevated dislocation density relative

to the as-fabricated reference (Figure 4.28). Of particular significance, nano-scale cavities (voids or gas bubbles) were identified in the in-core Cr coating by through-focus TEM imaging (Figure 4.29): these appear as bright spots in underfocused and dark spots in overfocused images, the standard Fresnel contrast signature of voids. These cavities were not observed in as-fabricated or out-of-core samples, indicating that they are a product of neutron irradiation damage. Quantitative characterization of cavity number density and size distribution is planned as follow-on work.

A separate TEM lamella prepared from the Zr alloy tube interior confirmed the presence of Nb- and Fe-enriched second-phase precipitates by STEM-EDS mapping (Figure 4.30). Visual comparison to the as-fabricated reference suggests a potentially higher number density and smaller average precipitate size, consistent with radiation-induced segregation and precipitate dissolution phenomena reported for similar Zr alloy systems under comparable irradiation conditions. Quantitative measurements of precipitate size and number density are in progress.

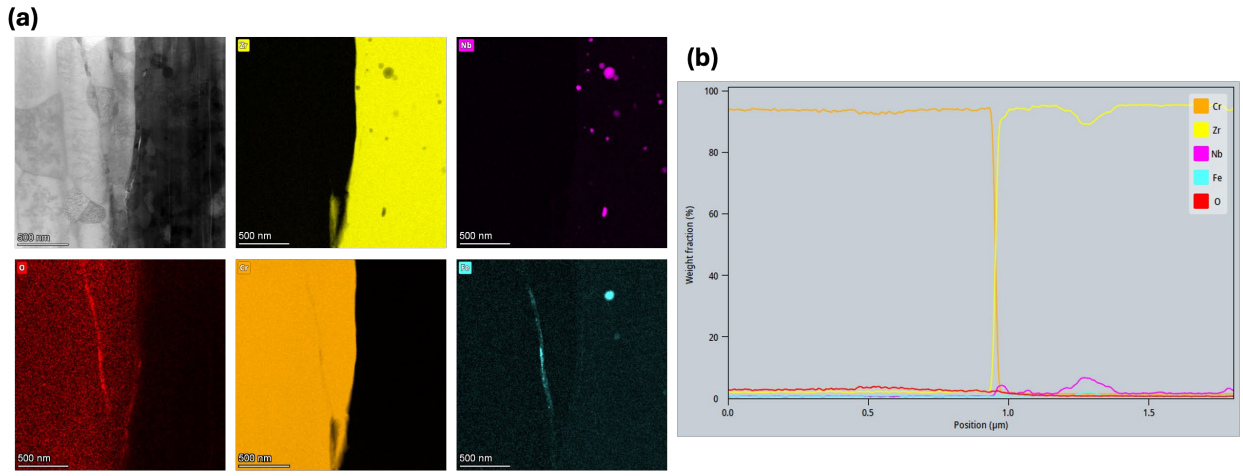

Figure 4.26. STEM-EDS analysis of the Cr/Zr alloy interface in in-core sample MI-Z-C1-2: (a) HAADF-STEM image of the interface region and corresponding EDS elemental maps showing Nb- and Fe-enriched precipitates in the Zr alloy and Cr-O enrichment along crack features in the Cr coating; (b) one-dimensional EDS line profile taken perpendicular to the interface confirming the absence of a $ZrCr_2$ intermetallic layer.

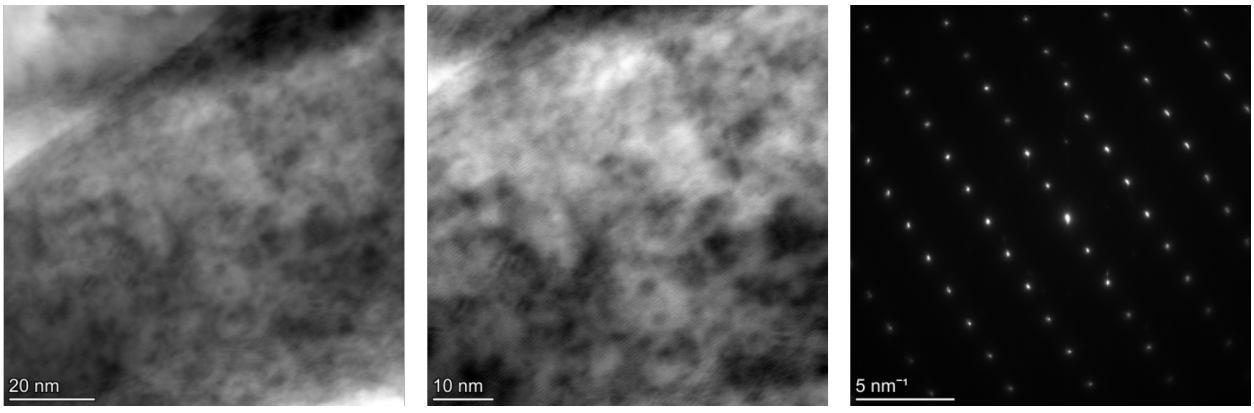

Figure 4.27. Dislocation substructure in the Zr alloy substrate of in-core sample MI-Z-C1-2: on-zone STEM image revealing radiation-induced dislocation loops and line defects consistent with approximately 0.5 dpa displacement damage.

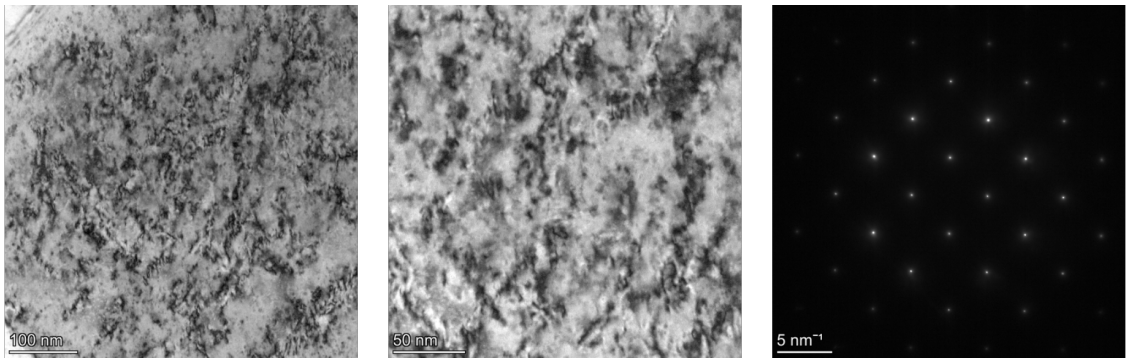

Figure 4.28. TEM analysis of the Cr coating in in-core sample MI-Z-C1-2: bright-field image with diffraction inset confirming elevated dislocation density relative to the as-fabricated reference.

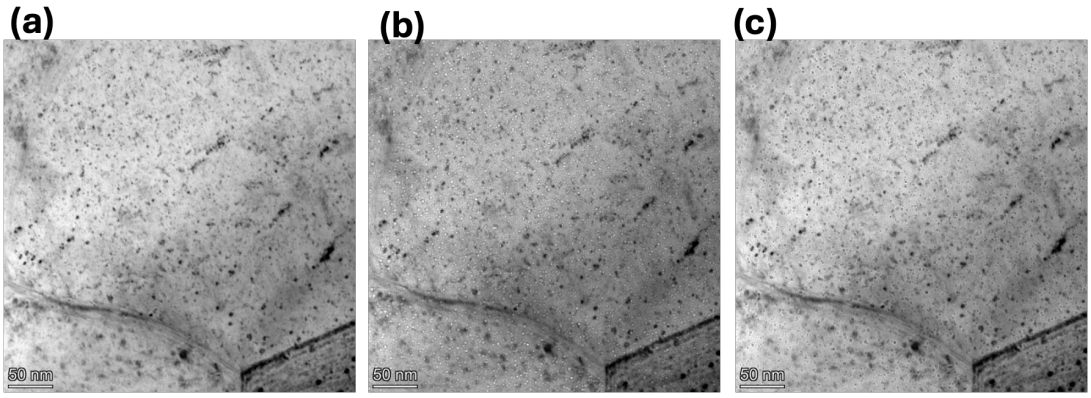

Figure 4.29. Through-focus TEM analysis of the Cr coating in in-core sample MI-Z-C1-2: (a) in-focus, (b) underfocused (−1 µm), and (c) overfocused (+1 µm) images revealing nano-scale cavities (voids) identified by Fresnel contrast. These cavities were absent in as-fabricated and out-of-core samples, confirming their origin as a neutron-irradiation-induced defect. Quantitative analysis of void number density and size distribution is ongoing.

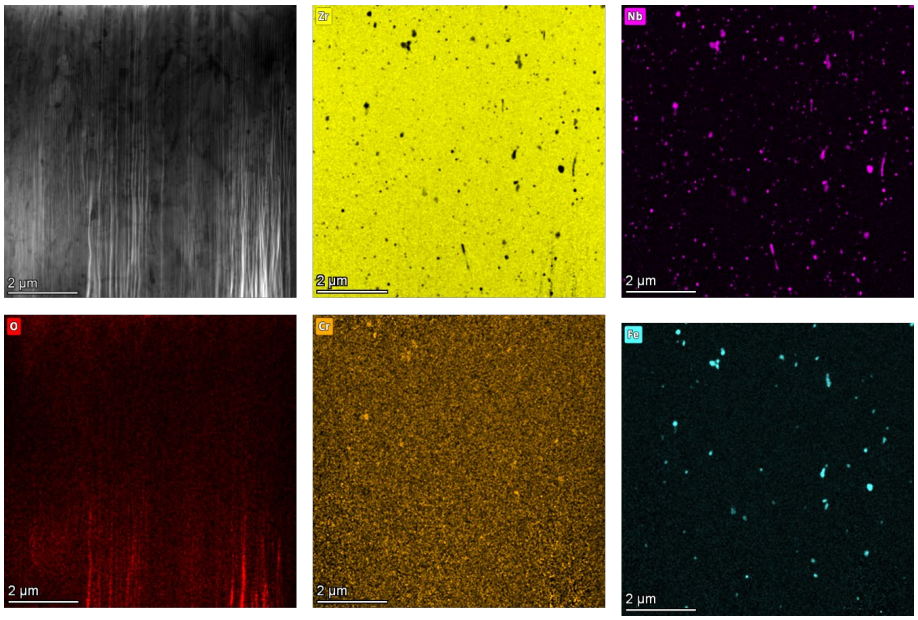

Figure 4.30. STEM-EDS elemental maps of the Zr alloy tube interior in in-core sample MI-Z-C1-2, confirming Nb- and Fe-enriched second-phase precipitates. Visual comparison to the as-fabricated reference (Figure 11) suggests a higher number density and smaller average precipitate size; quantitative analysis is in progress.

4.3.2.3 APT Analysis (MI-Z-C2-2)

APT specimens were prepared from the center region of the Zr alloy tubing of MI-Z-C2-2 using the dual-beam FIB process. Three-dimensional reconstruction was carried out using the LEAP 5000X HR instrument to elucidate microstructural and compositional changes in the irradiated material. The three-dimensional distributions of Sn, Fe, and Nb showed inhomogeneous distributions indicative of radiation-induced segregation. Clusters of approximately 1–2 nm enriched with Sn, Nb, and Fe were identified (Figure 4.31). A second specimen that captured a grain boundary exhibited a similar cluster microstructure, and the grain boundary itself showed segregation of Sn, Nb, and Fe, as demonstrated by the one-dimensional profile in Figure 4.32.

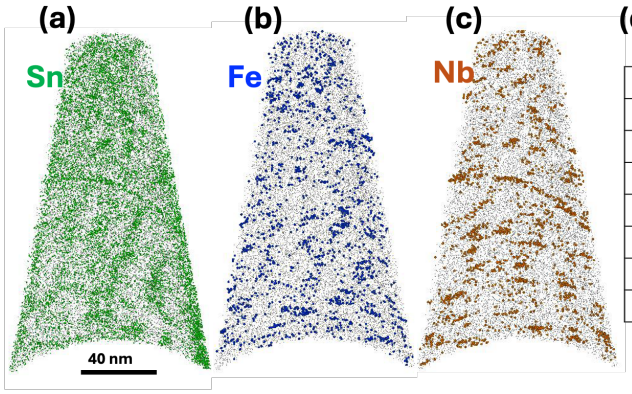

Elements	At.%
Zr	98.50
Sn	0.70
O	0.02
Nb	0.04
Fe	0.05
C	0.01
Si	0.01

Figure 4.31. APT analysis of the Zr alloy center region in in-core sample MI-Z-C2-2: three-dimensional atom map showing inhomogeneous distributions of Nb- and Fe-enriched nano-scale clusters (~1–2 nm) consistent with radiation-induced segregation.

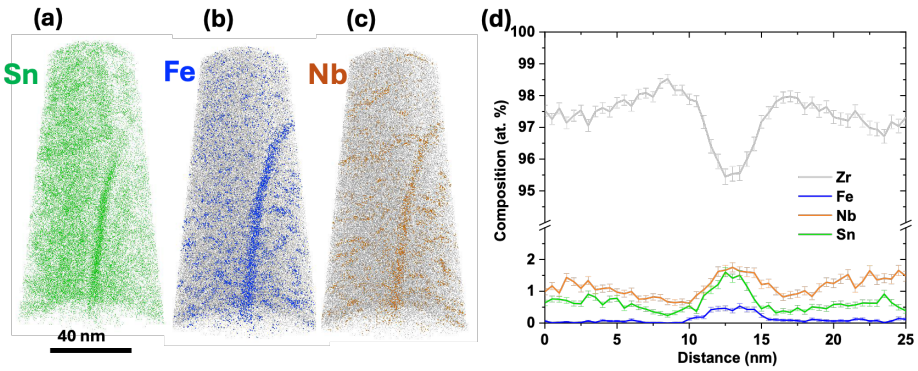

Figure 4.32. APT analysis of the Zr alloy region in in-core sample MI-Z-C2-2, with a grain boundary captured in the reconstruction: atom map and one-dimensional compositional profile across the grain boundary showing segregation of Sn, Nb, and Fe at the boundary plane.

A specimen prepared from the Cr coating region of MI-Z-C2-2 captured two grain boundaries (Figure 4.33). The three-dimensional atom maps revealed Cr oxide and Fe enrichment at both boundaries, with one-dimensional compositional profiles confirming the segregation behavior at each boundary.

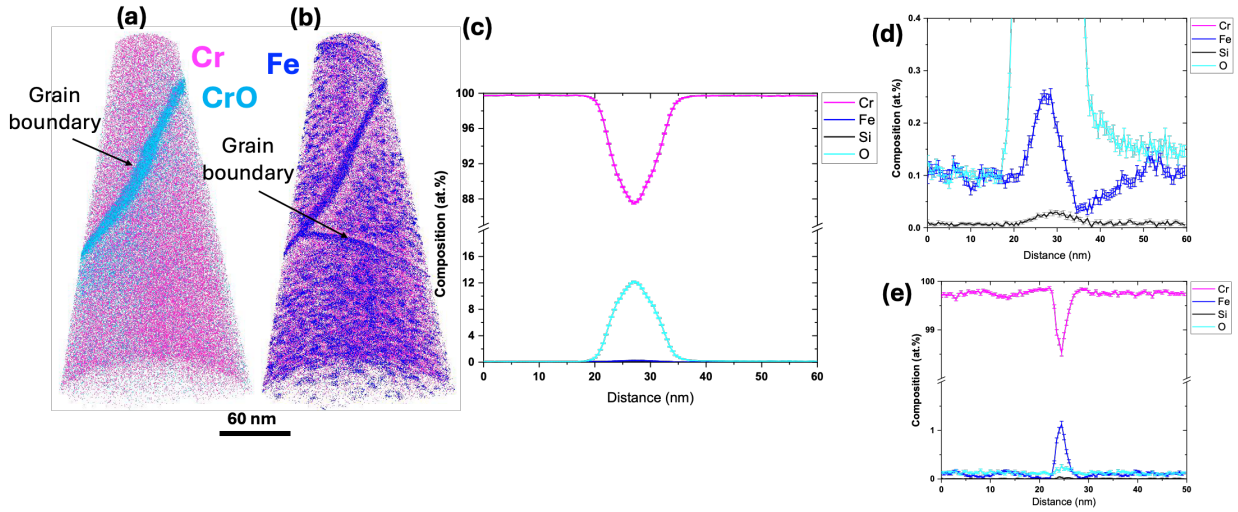

Figure 4.33. APT analysis of the Cr coating in in-core sample MI-Z-C2-2 with two grain boundaries captured in the reconstruction: (a) three-dimensional atom map showing the two grain boundaries; (b) Cr oxide iso-concentration surface; (c) Fe atom map; (d–e) one-dimensional compositional profiles taken across the first and second grain boundaries, respectively, confirming Cr oxide and Fe enrichment at both boundaries.

4.4 Summary of INL Findings

High-resolution characterization of as-fabricated, out-of-core, and in-core CS Cr-coated Optimized ZIRLO™ cladding at INL yielded the following principal findings:

- As-fabricated baseline (R-Z-C1): The CS Cr coating is phase-pure (~99.9 at.% Cr) with a wavy, mechanically interlocked interface. No $ZrCr_2$ intermetallic layer is present. Intrasplat microporosity and minor Cr oxide are inherent to the CS process. Grain boundary chemistry is variable, with some boundaries showing Cr oxide segregation and Fe enrichment. The Zr alloy substrate shows no Cr diffusion and contains β-Nb and $Zr(Fe,Cr)_2$ second-phase precipitates.
- Out-of-core aqueous exposure (MO-Z-C1-2, MO-Z-C2): Significant ZrH formation was observed in the Zr alloy substrate, confirmed by TEM diffraction (δ-$ZrH_{1.5-2}$ phase) and optical/SEM imaging. Hydrogen ingress occurred from both the outer Cr-coated surface and the uncoated inner diameter. ZrO_2 was identified at the inner diameter. No significant bulk compositional change was detected in the Cr coating at 2–4 μm from the interface relative to the as-fabricated reference.
- In-core irradiation (MI-Z-C1-2, MI-Z-C2-2): The bulk ZrH phase fraction was substantially lower than in the out-of-core sample, with no δ-ZrH diffraction spots detected in TEM. The Cr coating accumulated elevated dislocation density and, notably, nano-scale cavities (voids) attributable to neutron irradiation damage — a feature absent in as-fabricated and out-of-core samples. Radiation-induced segregation produced 1–2 nm Sn/Nb/Fe-enriched clusters in the Zr alloy and enhanced segregation at grain boundaries. The Cr/Zr interface remained free of $ZrCr_2$ intermetallic layer under both exposure conditions.

5.0 Summary and Future Work

In collaboration together, PNNL and INL studied various Cr-coated and uncoated variants of Optimized ZIRLO™ in an effort to understand hydride generation within the samples. Collectively, the results from the laboratories are highly complementary and present a consistent story. Key findings from the results were:

- The CS Cr-coated cladding developed significant hydrides in out-of-core conditions, suggesting enhanced hydrogen pickup relative to the uncoated cladding under the same conditions.
- Under in-core conditions, the formation of hydrides was suppressed in comparison to equivalent out-of-core samples.
- In-core samples in the CS Cr-coated variants exhibited damage features unique to in-core conditions, specifically nano-voids in the Cr-coating and nanoscale radiation-induced segregation clusters in the substrate. These findings have implications for long-term coating integrity.
- The CS Cr-coated materials exhibited an interdiffusion-free Cr/Zr bond with no intermetallic formation. The PVD coatings as a whole exhibited poorer quality samples, with multiple cracks and pores easily observable on the OM.
- Automated image-based quantification techniques were explored, but overestimated the bulk hydrogen content in the sample. Sample preparation is of critical importance in this analysis. Further, standards to run with this form of analysis are also important to validate and quantify techniques.

Ultimately, the investigation of the nucleation and growth mechanisms of the hydrides in the zircaloy substrate poses a challenging question. The cladding studied here poses the additional complication of being tested with an open inner diameter, which adds additional pathways for hydrogen in the matrix. To better examine and understand the mechanisms occurring in samples such as these, a methodical analysis of conditions, coating variants, and integrated post-irradiation examination techniques would need to be performed.

6.0 References

Alakiozidis, I., C. Hunt, A.D. Smith, M. Maric, Z. Shah, A. Ambard, and P. Frankel. 2025. "Microstructure and mechanical performance of cold spray Cr coatings." *Journal of Nuclear Materials* 604: 155492.

ASTM. 2017. *Standard Guide for Preparation of Metallographic Specimens.* ASTM E3-11. West Conshohocken, Pennsylvania: ASTM International.

ASTM. 2019. *Standard Guide for Calibrating Reticles and Light Microscope Magnifications.* ASTM E1951-14. West Conshohocken, Pennsylvania: ASTM International.

ASTM. 2023. *Standard Test Methods for Vickers Hardness and Knoop Hardness of Metallic Materials.* ASTM E92-17. West Conshohocken, Pennsylvania: ASTM International.

Bevington, P.R. 1969. *Data Reduction and Error Analysis for the Physical Sciences*. McGraw-Hill.

Bischoff, J., C. Delafoy, C. Vauglin, P. Barberis, C. Roubeyrie, D. Perche, D. Duthoo, F. Schuster, J.-C. Brachet, E.W. Schweitzer, and K. Nimishakavi. 2018. "AREVA NP's enhanced accident-tolerant fuel developments: Focus on Cr-coated M5 cladding." *Nuclear Engineering and Technology* 50 (2): 223–228.

Brachet, J.-C., I. Idarraga-Trujillo, M.L. Flem, M.L. Saux, V. Vandenberghe, S. Urvoy, E. Rouesne, T. Guilbert, C. Toffolon-Masclet, M. Tupin, C. Phalippou, F. Lomello, F. Schuster, A. Billard, G. Velisa, C. Ducros, and F. Sanchette. 2019. "Early studies on Cr-Coated Zircaloy-4 as enhanced accident tolerant nuclear fuel claddings for light water reactors." *Journal of Nuclear Materials* 517: 268–285.

Colas, K.B., A.T. Motta, M.R. Daymond, and J.D. Almer. 2013. "Effect of thermo-mechanical cycling on zirconium hydride reorientation studied in situ with synchrotron X-ray diffraction." *Journal of Nuclear Materials* 440 (1): 586–595.

Comstock, B., and P. Barbéris. 2015. *Zirconium in the Nuclear Industry: 17th Volume*. ASTM International.

Couet, A., A.T. Motta, and R.J. Comstock. 2014. "Hydrogen pickup measurements in zirconium alloys: Relation to oxidation kinetics." *Journal of Nuclear Materials* 451 (1): 1–13.

Daum, R.S., Y.S. Chu, and A.T. Motta. 2009. "Identification and quantification of hydride phases in Zircaloy-4 cladding using synchrotron X-ray diffraction." *Journal of Nuclear Materials* 392 (3): 453–463.

Devaraj, A., B. Matthews, B. Arey, L. Bagaasen, E. Buck, G. Sevigny, and D. Senor. 2021. "Neutron irradiation induced changes in isotopic abundance of 6Li and 3D nanoscale distribution of tritium in LiAlO2 pellets analyzed by atom probe tomography." *Materials Characterization* 176: 111095.

Di, S., Z. Yao, M.R. Daymond, X. Zu, S. Peng, and F. Gao. 2015. "Dislocation-accelerated void formation under irradiation in zirconium." *Acta Materialia* 82: 94–99.

Ells, C.E. 1968. "Hydride precipitates in zirconium alloys (A review)." *Journal of Nuclear Materials* 28 (2): 129–151.

EPRI. 1992. *Corrosion of Zircaloy-Clad Fuel Rods in High-Temperature PWRs: Measurement of Waterside Corrosion in North Anna Unit 1.* TR-100408. Electric Power Research Institute.

Fazi, A., M. Sattari, K. Stiller, H.-O. Andrén, and M. Thuvander. 2023. "Performance and evolution of cold spray Cr-coated optimized ZIRLO™ claddings under simulated loss-of-coolant accident conditions." *Journal of Nuclear Materials* 576: 154268.

Guo, D., D. Zhao, J. Ding, X. Liu, and J. Zheng. 2025. "Cr/CrOx thin films deposited by magnetron sputtering on ABS surface and their properties." *Ceramics International* 51 (28, Part B): 57715–57731.

Harkness, S.D., and C.-Y. Li. 1971. "A study of void formation in fast neutron-irradiated metals." *Metallurgical Transactions* 2 (5): 1457–1470.

High Pressure Cold Spray: Principles and Applications. 2016. Edited by Charles M. Kay and J. Karthikeyan. ASM International.

Kearns, J.J. 1967. "Terminal solubility and partitioning of hydrogen in the alpha phase of zirconium, Zircaloy-2 and Zircaloy-4." *Journal of Nuclear Materials* 22 (3): 292–303.

Kehr, K.W. 1978. "Theory of the diffusion of hydrogen in metals." In *Hydrogen in Metals I: Basic Properties*, edited by Georg Alefeld and Johann Völkl, 197–226. Berlin, Heidelberg: Springer Berlin Heidelberg.

Khatamian, D. 1997. "Hydrogen diffusion in oxides formed on surfaces of zirconium alloys." *Journal of Alloys and Compounds* 253-254: 471–474.

Kim, H.-G., I.-H. Kim, Y.-I. Jung, D.-J. Park, J.-H. Park, B.-K. Choi, and Y.-H. Lee. 2018. "Out-of-pile performance of surface-modified Zr cladding for accident tolerant fuel in LWRs." *Journal of Nuclear Materials* 510: 93–99.

Klinger, M. 2017. "More features, more tools, more CrysTBox." *Journal of Applied Crystallography* 50 (4): 1226–1234.

Krejčí, J., J. Kabátová, F. Manoch, J. Kočí, L. Cvrček, J. Málek, S. Krum, P. Šutta, P. Bublíková, P. Halodová, H.K. Namburi, and M. Ševeček. 2020. "Development and testing of multicomponent fuel cladding with enhanced accidental performance." *Nuclear Engineering and Technology* 52 (3): 597–609.

Lahoda, E.J. 2022. *Westinghouse Accident Tolerant Fuel Phase 2B with Higher Enriched and Higher Burnup Add-On Project Final Technical Report Deliverable Volume 1.* Westinghouse Electric Company LLC (United States).

Maier, B., H. Yeom, G. Johnson, T. Dabney, J. Walters, J. Romero, H. Shah, P. Xu, and K. Sridharan. 2018. "Development of Cold Spray Coatings for Accident-Tolerant Fuel Cladding in Light Water Reactors." *JOM* 70 (2): 198–202.

Maric, M., R. Thomas, J. Nunez-Iglesias, M. Atkinson, J. Bertsch, P. Frankel, C. Race, P. Barberis, F. Bourlier, M. Preuss, and P. Shanthraj. 2022. "A novel method for radial hydride analysis in zirconium alloys: HAPPy." *Journal of Nuclear Materials* 559: 153442.

Mattox, D.M. 2010. "Chapter 1 - Introduction." In *Handbook of Physical Vapor Deposition (PVD) Processing (Second Edition)*, 1–24. Boston: William Andrew Publishing.

Motta, A.T., L. Capolungo, L.-Q. Chen, M.N. Cinbiz, M.R. Daymond, D.A. Koss, E. Lacroix, G. Pastore, P.-C.A. Simon, M.R. Tonks, B.D. Wirth, and M.A. Zikry. 2019. "Hydrogen in zirconium alloys: A review." *Journal of Nuclear Materials* 518: 440–460.

Motta, A.T., A. Couet, and R.J. Comstock. 2015. "Corrosion of Zirconium Alloys Used for Nuclear Fuel Cladding." *Annual Review of Materials Research* 45: 311–343.

Nelson, R.S., J.A. Hudson, and D.J. Mazey. 1972. "The stability of precipitates in an irradiation environment." *Journal of Nuclear Materials* 44 (3): 318–330.

Norris, D.I.R. 1972. "Voids in irradiated metals (Part I)." *Radiation Effects* 14 (1-2): 1–37.

Oriani, R.A. 1970. "The diffusion and trapping of hydrogen in steel." *Acta Metallurgica* 18 (1): 147–157.

Pan, G., D.B. Mitchell, A.M. Garde, J.L. Norrell, A.R. Atwood, and M. Limbaeck. 2016. "Advantages gained by Optimized ZIRLO and AXIOM PWR cladding materials." United States.

Puls, M.P. 2012. "Diffusion of Hydrogen." In *The Effect of Hydrogen and Hydrides on the Integrity of Zirconium Alloy Components: Delayed Hydride Cracking*, edited by Manfred P. Puls, 153–174. London: Springer London.

Quillin, K., H. Yeom, T. Dabney, E. Willing, and K. Sridharan. 2022. "Microstructural and nanomechanical studies of PVD Cr coatings on SiC for LWR fuel cladding applications." *Surface and Coatings Technology* 441: 128577.

Ševeček, M., A. Gurgen, A. Seshadri, Y. Che, M. Wagih, B. Phillips, V. Champagne, and K. Shirvan. 2018. "Development of Cr cold spray–coated fuel cladding with enhanced accident tolerance." *Nuclear Engineering and Technology* 50 (2): 229–236.

Shi, X., S. Zhang, J. Li, Y. You, X. Yu, D. Sun, Y. Shao, H. Du, D. Wang, M. Zhao, M. Zhu, and F. Li. 2023. "Enhancement of hardness and corrosion resistance of Al-Si-N multilayer color coating via SiN/AlSiN/AlN compositional gradient interlayer." *Journal of Vacuum Science & Technology A* 42 (1).

Shimskey, R.W., J.R. Allred, S.E. Asmussen, H.T. Brown, S.K. Cooley, R.C. Daniel, M.K. Edwards, J.G. Geeting, A.P. Goulet, C.H. Holbrook, P.J. Macfarlan, E.K. Nickerson, L.I. Richmond, T.J. Roosendaal, A.M. Westesen, B.E. Westman, and B.D. Hanson. 2022a. *PNNL FY 2022 Sibling Pin Testing Results.* (Richland, WA).

Shimskey, R.W., J.R. Allred, S.E. Asmussen, S.K. Cooley, R.C. Daniel, L. Dinh, M.K. Edwards, J.G.H. Geeting, Z. Huber, N.A. Klymyshyn, J.M. Lonergan, P.J. MacFarlan, E.K. Nickerson, L.I. Richmond, T.J. Roosendahl, R.D. Torres, A.M. Westesen, B.E. Westman, and B.D. Hanson. 2022b. *PNNL FY 2021 Sibling Pin Testing Results.* M2SF-21PN010201057, M2SF-22PN010201062. Pacific Northwest National Laboratory (Richland, WA).

Singh, H., M. Kumar, and R. Singh. 2022. "An overview of various applications of cold spray coating process." *Materials Today: Proceedings* 56: 2826–2830.

Terrani, K.A. 2018. "Accident tolerant fuel cladding development: Promise, status, and challenges." *Journal of Nuclear Materials* 501: 13–30.

Varvenne, C., O. Mackain, L. Proville, and E. Clouet. 2016. "Hydrogen and vacancy clustering in zirconium." *Acta Materialia* 102: 56–69.

Yeom, H., B. Maier, G. Johnson, T. Dabney, M. Lenling, and K. Sridharan. 2019. "High temperature oxidation and microstructural evolution of cold spray chromium coatings on Zircaloy-4 in steam environments." *Journal of Nuclear Materials* 526: 151737.

Zhang, Y., M. Bartosik, S. Brinckmann, U. Bansal, S. Lee, and C. Kirchlechner. 2025. "Columnar grain boundaries are the weakest link in hard coatings: insights from micro-cantilever testing." *Materials Research Letters* 13 (11): 1099–1107.

Pacific Northwest National Laboratory

902 Battelle Boulevard
P.O. Box 999
Richland, WA 99354

1-888-375-PNNL (7665)

www.pnnl.gov